Design of Digital Receivers for Low Frequency Radio Astronomy

A thesis submitted for the degree
of
Doctor of Philosophy
in the
University College of Science, Technology and Agriculture
Department of Applied optics and Photonics
University of Calcutta

By

V. Mugundhan

Indian Institute of Astrophysics
Bangalore

November, 2018

This thesis is dedicated to my parents.

Publications, Talks and Awards

Refereed Journals

1. **V. Mugundhan**, R. Ramesh, I. V. Barve, C. Kathiravan, G.V.S. Gireesh, P. Kharb, A. Misra, *Low Frequency radio observations of the solar corona with arcminute angular resolution: implications for coronal turbulence and weak energy releases*, The Astrophysical Journal, Volume 831, Issue 2, pp. 154.

2. **V. Mugundhan**, K. Hariharan, R. Ramesh, *Solar type IIIb bursts as tracers for electron density fluctuations in the corona*, Solar Physics, Volume 292, Issue 11, pp. 155.

3. **V. Mugundhan**, R. Ramesh, C. Kathiravan, G.V.S. Gireesh, Aathira Hegde, *Spectropolarimetric Observations of Solar Noise Storms at Low Frequencies*, Solar Physics, Volume 293, Issue 3, pp. 41.

4. **V. Mugundhan**,R. Ramesh, C. Kathiravan, G. V. S. Gireesh, A. Kumari, K. Hariharan, I. V. Barve, *The First Low Frequency Radio Observations of the Solar Corona on a ≈ 200 km Long Interferometer Baseline*, The Astrophysical Journal Letters, Volume 855, Issue 1, pp. L8.

Talks and Proceedings

1. *Feasibility Analysis for Long Baseline Interferometry below ≈ 60 MHz at Gauribidanur* at URSI-RCRS, 2015, JNU Delhi

2. *Long Baseline interferometric observations of sub-arc minute structures in the solar corona* at URSI-RCRS, 2017, NARL Tirupathi

3. *Radio Interferometric Observations of sub-arc minute structures in the solar corona* at International Workshop of Solar, Heliospheric and Magnetospheric Radioastronomy: The legacy of Jean Louis Steinberg, 2017, Paris Observatory

Awards

1. Best Instrumentation Paper for year 2016, for the publication *Low Frequency radio observations of the solar corona with arcminute angular resolution: implications for coronal turbulence and weak energy releases*, awarded on August, 2018 at Indian Institute of Astrophysics.

2. Third Place in Student Paper Competition at URSI-RCRS 2017 at NARL Tirupathi.

Abstract

Low frequency radio observations of the solar corona provide valuable information on the heliocentric distance range $\approx 1.1R_{\odot}$ - $3R_{\odot}$, which is relatively difficult to observe from other wavelengths. These observations are crucial as it is believed that events of importance from the point of view of solar-terrestrial relations originate from the above height range. These events are transient in nature and are accompanied by a sudden non-thermal energy release (bursts) at radio frequencies. Due to their non-thermal nature, these bursts are more intense at low frequencies and thus can be observed with a better contrast.

A primary emission mechanism for these bursts are plasma emission, which is created due to acceleration of electrons in the ambient coronal plasma by shocks associated with transient emission. The nature of the shock, the fluctuations in electron density and other plasma properties can be inferred by studying the temporal, spectral, and spatial characteristics of the radio bursts. This thesis describes design and development of new instrumentation for performing high resolution observations of the solar corona at low frequencies ($\leq$ 400 MHz).

To begin with, a Low frequency Long-baseline Interferometer (LBI) experiment was conceived to study small scale angular structures ($<$ 1′) and the role of scattering induced due to density turbulence in the solar corona. The antennas, analog, and Field Programmable Gate Array (FPGA) based digital system were developed in house. Using this systems, observations were carried out at a frequency of 37 MHz with a band-width of $\approx$ 2 MHz. In LBI observations, it is not always possible to have a real-time link between the individual receiver stations. This calls for external synchronization between both the stations, which was achieved using Commercially-Off-The-Shelf (COTS) Global Positioning System Disciplined Oscillator (GPSDO). The complete LBI system design and characterization is described.

The aforementioned system was used for observations in two main campaigns. First, over an 8 km baseline, with an angular resolution of $\approx 1'$ at 37 MHz, Solar Noise Storms and type III bursts, frequently associated active-regions were observed. These observations, for the first time, showed that structures as small as 1′ in the solar corona, whence radio emission at 37 MHz typically originates. Further, these structures were found to be associated with weak energy releases ($\approx 10^{18\pm2}$ ergs [1]). This gave us confidence to repeat the same experiment over a longer baseline during the second campaign. For this, a group of the Gauribidanur Radio Interferometric Polarimeter (GRIP) and the Indian Mesospheric-Stratospheric-Tropospheric (MST) Radar were used as the "arms" of the interferometer. The effective resolution of the interferometer was $\approx 3''$. In this observation campaign, correlated emission of a type III radio burst with frequency fine structure was observed. Analysis indicated that the source region of this burst at 53 MHz was $\approx 10''$.

A FPGA based spectrometer was developed to work in the frequency range of 40 - 80 MHz, with high spectral and temporal resolutions (22 kHz and 5 ms). The objective of developing this instrument was to study fine structures in time and frequency associated with solar radio bursts. During a two month observing period with this instrument, ≈ 20 type III radio bursts with fine structures in frequency (type IIIb bursts) were observed. With the high spectral and temporal resolution provided by the instrument, the individual spectral fine structures, called "stria" were resolved in both the domains. The center frequency and bandwidth information of the striae was used to study the electron density inhomogeneities in the solar corona in the heliocentric distance range of $\approx 1.6R_\odot$ - $2.2R_\odot$, by the way of density modulation index ($\frac{\delta N_e}{N_e}$). It was found that the density inhomogeneities followed a one dimensional Kolmogorov-like turbulence spectrum. The derived Kolmogorov Power-Law index was used to estimate the amplitude of turbulent fluctuations, $C_n^2(R)$ in the aforementioned distance range. The uniqueness of this work is that this is the first instance where ground-based high resolution observations have been used to derive the nature of density fluctuations in the near-sun atmosphere.

Indirect measurements of the nature of magnetic fields in the solar

[1] 1 erg = 10^{-7} Watt Seconds (Ws)

corona can be obtained from radio polarimeter measurements. Since emission at different frequencies originate from different radial distances, a spectro-polarimeter would enable measurements of magnetic fields as a function of the heliocentric distance. With this as a motivation, a FPGA based Spectropolarimeter was implemented on a Reconfigurable Open Architecture Computing Hardware (ROACH) Board with a four channel ADC as a Spectropolarimeter Backend for the GRIP array. Based on the results from this experiment, a new Long-Baseline Polarimeter array operating in the frequency range of 15 MHz - 85 MHz was commissioned to observe the polarization signatures of coronal transients, free of the quiet-Sun background. An upgraded version of the initial Spectropolarimeter implementation was used as the backend of the new array. Using this, a Solar noise storm was observed in the aforementioned range of frequencies. A statistics of the type I, type III, the low and high frequency background continuum was obtained. It is found that type I storm bursts transition to type III at a frequency of $\approx$ 60 MHz. The spectral index of type I and type III bursts are found to be $\approx$ +3.5 and $\approx$ -2.7, respectively. The measured degree of circular polarization was $\approx$ 90 % for type I bursts and $\approx$ 25 % for type III bursts. The differences in polarization is explained by interpreting the bursts using magneto-ionic o- and e-modes. A unified scenario of the observation is visualized and described.

Solar Radio bursts are sometimes found to occur upto frequencies of 400 MHz. The radiation at such high frequencies originate from coronal regions close to the Sun. In order to observe such transient emission and their radial evolution, a wide-band spectropolarimeter was implemented using ROACH and a 2 channel 1 GHz ADC as a backend to the Gauribidanur Radio Spectropolarimeter (GRASP) antenna system. The system design and characterization is outlined. Preliminary science observations of the Sun is analyzed and the salient features of the result is discussed.

List of Figures

List of Tables

Contents

[2]Section 4.4 and 4.5 are covered in detail in the thesis *Solar Radio Observations at Low Frequencies with High Spectral and Temporal Resolutions* by K. Hariharan. Here it is recapitulated for the sake of completeness.

Chapter 1

Introduction

1.1 The Sun

1.1.1 Historical Note

The Sun has played an important role in human life for many centuries. As human knowledge evolved, so has Sun's status, from a God to a star at the center of the solar system, which has been vital in sustaining life on Earth.

The first suggestion that the Sun could be a star comes from a 5^{th} century BC philosopher Anaxagoras. He proposed that Sun as a mass of blazing metal, larger than a few thousand square miles. He also extended this theory to other stars stating that they were also similar to the Sun. These theories were notorious and he was charged with *impiety*, and was exiled from Athens [Filonik 2013]. Anaxagoras' ideas were endorsed by another greek philosopher, Aristarchus[1].

During the 5^{th} century CE, an Indian astronomer and mathematician, Aryabhata, put forth ideas that Earth rotated on its own axis, and Earth and the accompanying planets revolved around the Sun, bringing in heliocentrism for the first time. A quantitative analysis of the planets and its orbits were summarized in a compilation called Surya Siddhanta [Burgess 1978]. This ideas and estimates were later discovered independently by Ptolemy and Copernicus in Europe.

[1] https://www2.hao.ucar.edu/Education/solar-physics-historical-timeline-1223-BC-250-BC#200bc

Galileo made naked-eye observations of Sunspots and summarized his results in the phamplet *Letters on Sunspots*[2]. He showed that sunspots were surface features of the Sun and not planetary transits with comprehensive tables of motions of the former and their correlation with the appearance of the spots. He used these to suggest that the Sun also rotated about its own axis. Studies on sunspots did not continue further in the 17^{th} century due to the onset of Maunder Minimum [Eddy 1976].

Studies were renewed again after the detection of Infrared and Ultraviolet radiation from the Sun[3]. It was soon realized that the properties of the solar atmosphere could be deduced from these lines. In 1843, Samuel Schwabe noted that the number of sunspots showed a cyclic variation [Schwabe 1844]. Joseph Henry, in 1848, for the first time, determined that the sunspots were inherently colder than the surface of the sun. Carrington noted that as the solar cycle progresses, the sunspot activity, slowly moved towards the equator [Carrington 1863]. The magnetic nature of the sun and sunspots were discovered by the Harold and Horace Babcock [Babcock and Babcock 1955].

By the beginning of the 20^{th} century, observatories were set up all over the world to enable photometric and spectrometric observations of the Sun, with the most prominent observatories being Kodaikanal Solar Observatory[Kochhar 2002], and Mount Wilson Observatory[Hale 1908].

1.2 The Solar Interior

The Hertzsprung-Russel (HR) diagram (see Figure 1.1) provides the relationship between stellar luminosities and their temperature. All these values are normalized to that of the Sun, which falls in the 'G' band of the diagram, indicating that it has a surface temperature of $\approx$ 6000 K. It is a Population I, metal rich, young star, which could have been a product of a supernova explosion. The constituents of the Sun are mostly Hydrogen, which makes up almost 75% of its mass followed by Helium (25%). Other

[2] http://www.astro.umontreal.ca/~paulchar/grps/histoire/newsite/autres/3letters_e.html

[3] https://www2.hao.ucar.edu/Education/solar-physics-historical-timeline-1800-1999#1843

than these two principal constituents, there are also elements like oxygen, carbon, iron etc. The structure of the Sun from the interior to exterior is shown in Figure 1.2.

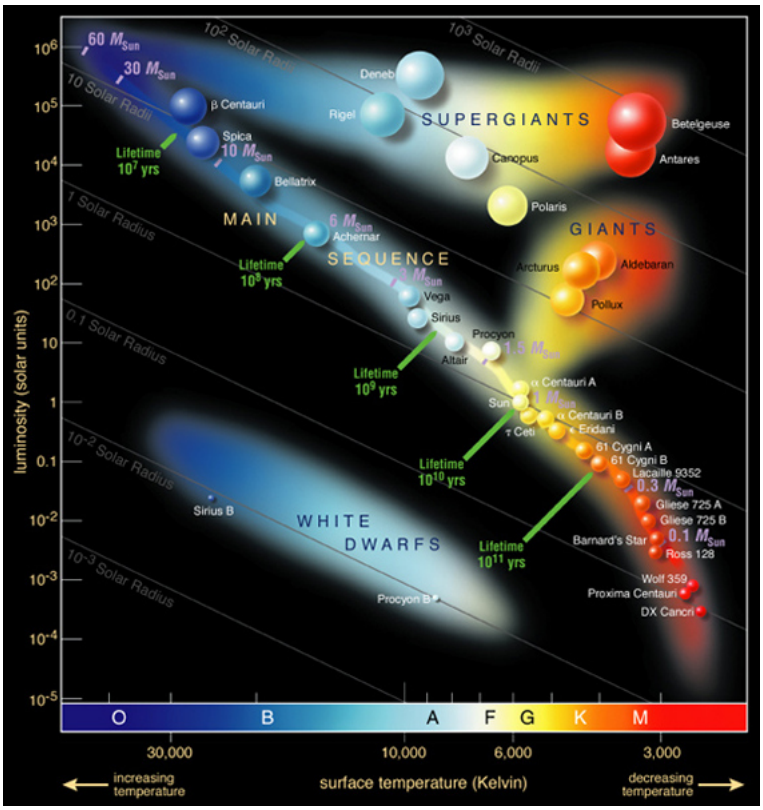

Figure 1.1: Hertzsprung-Russel (HR) diagram which is a scatter of luminosity and temperature of various stars. Note that the Sun is the luminosity reference, and it falls in the 'G' band, indicating its surface temperature to be ≈ 6000 K. (Picture Courtesy: `https://en.wikipedia.org/wiki/Hertzsprung-Russell_diagram`).

1.2.1 The Core

The energy production in the Sun is due to Nuclear Fusion. This theory was advocated by Arthur Eddington, and was formalized by Hans Bethe [Bethe 1939]. The process starts when 2 protons fuse together to form a diproton, given by the following reaction:

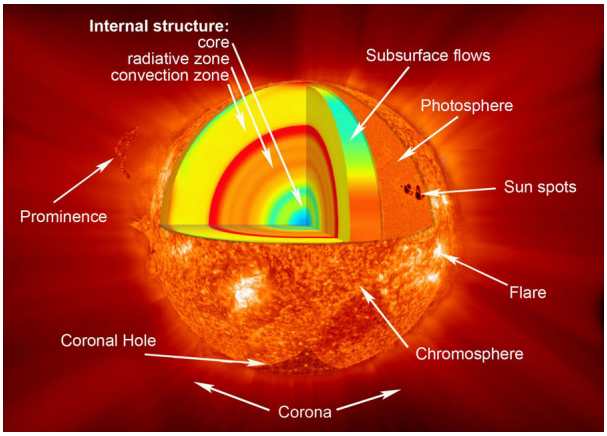

Figure 1.2: Structure of the Sun (Picture Courtesy: `https://scied.ucar.edu/sun-regions`).

$$ {}^{1}_{1}H + {}^{1}_{1}H \rightarrow {}^{2}_{2}He. $$

The above reaction is followed by a beta decay of the diproton as follows:

$$ {}^{2}_{2}He \rightarrow {}^{2}_{1}D + e^{+} + \nu_e, $$

where the diproton decays into deutrium, emitting a positron and a neutrino. The probability of occurrence of this reaction is extremely rare as the above reaction is a consequence of weak-force, which is usually dominated by electromagnetic or gravitational forces. The emitted positron annihilates by reacting with an electron releasing energy and 2 gamma ray photons.

$$ e^{-} + e^{+} \rightarrow 2\gamma + 1.02MeV. $$

The deuterium formed in the first stage fuses with another hydrogen atom, and produces an isotope of helium along with a gamma ray photon. Contrary to the first step, this process happens a lot quicker, as it is a consequence of the strong force.

$$ {}^{2}_{1}D + {}^{1}_{1}H \rightarrow {}^{3}_{2}He + \gamma + 5.49MeV. $$

Once this helium isotope is generated, the reaction can take four possible routes:

1. The p-p I branch, where 2 helium isotopes combine, forming a helium atom, producing two protons and ≈ 12 MeV of energy. Around 2% of the energy is taken away by the neutrinos. This reaction is dominant at temperatures around 10 - 14 MK, as below this limit, not much He is produced. p-p reaction chain is the most frequently occurring reaction in the Sun.

2. The p-p II branch, where a He atom, and isotope combine to produce a heavier Berelium isotope and a gamma ray photon. The Be isotope captures a positron, and becomes a Lithium atom, by releasing an electron neutrino, along with 0.861 MeV of energy if lithium is in ground state, and 0.383 MeV of energy for lithium in exited state. This probability of this reaction is ≈ 17 %.

3. The third branch, the p-p III branch, the first step, until the formation of the Be isotope is the same as p-p II, but here, the generated isotope fuses with a proton, forming a heavier Be isotope, by releasing a gamma ray photon. This isotope then beta decays forming a Be atom, which disintegrates to 2 He atoms. This reaction is dominant only at temperatures >23 MK. The neutrinos produced in this reaction are of the highest energies (upto 14.06 MeV), but the probability of this reaction is 0.02 %.

4. There is also a fourth reaction called the p-p IV, but has never been observed. In this reaction, a proton is captured by a He isotope, giving out a He atom, along with a positron and a neutrino, with ≈ 19 MeV of energy.

While the Carbon-Nitrogen-Oxygen (CNO) cycle is also possible, it has been observed to be dominant only in stars with masses ≈ 1.3 times greater than that of the Sun. All these energy release reactions happen in the core of the Sun, whose extent is about a quarter of a solar radius.

Detecting the neutrinos released during these reactions will provide insights into the reactions happening in the core of the Sun. Attempts to detect these were made by Ray Davis and John Bahcall [Bahcall 1964, Davis Jr 1964]. During the early observations, there was observed to be a deficit in the amount of neutrinos from the Sun. It was later found that this

discrepancy arose from the fact that the neutrinos changed flavors. This was observed experimentally by the Sadbury Neutrino Observatory [Boger et al. 2000] after extensive analysis and they determined the fraction to be about 34%, which is in close agreement with the theoretically predicted value [Ahmad et al. 2002]. This issue was resolved in 2002, and was awarded the Nobel prize in 2015.

1.2.2 Radiative Zone

The volume in the Sun between the core and to $\approx$ 70 % of its radius is the radiation zone. The temperature of this zone is lower than the core temperature. The plasma in this region is in hydrostatic and thermal equilibrium. The plasma regions are isolated from each other thermally, and the neighbouring regions are tightly enclosed. This satisfies the conditions for black-body radiation [Zirker 2002].

The plasma in the radiative zone is optically thick. This causes the mean free path of the photons to be very small. A shallow temperature gradient drives the movement of the photons through the optically thick plasma.

The average time for a gamma ray photon to reach the Sun's surface is about 2×10^5 years. This is because of the multiple scattering and wavelength shifts it undergoes as it crosses the radiative zone.

1.2.3 Convection Zone

Enclosing the radiative zone is a region of turbulent plasma, called the convection zone. This zone extends from a radius of 200000 km, all the way out to the surface of the Sun.

Convective zone is made of plasma, which is constantly heated by the emission from radiative zone. The temperature gradient across the convection zone is $\approx 2 \times 10^5$ K. This difference in temperature is the cause of mass motion of plasma from the lower to the outer regions of the convection zone. When the plasma convects to the surface, it cools down, and starts sinking back into the surface of the Sun. The convective flow of plasma is turbulent. The turbulent motion of the gas in the convection zone, coupled with the differential rotation of the Sun causes the generation of electric

currents, which in-turn gives rise to magnetic fields, creating the Solar Dynamo.

The granules seen in the Solar photosphere is due to convection. The interior of the Sun is studied extensively using numerical simulations. With the advent of high resolution space based imaging instruments, a new tool called Helioseismology has emerged, that can be used to infer the properties of both the radiation and convective zone.

1.2.4 Helioseismology

A useful tool to study the Sun's radiative and convective zones is Helioseismology. The primary focus of the above field is to study Sun's properties through its waves and oscillations. There are two sub-divisions, namely local and global. The former studies waves propagating at or close to the surface of the Sun, while the latter studies the resonant modes.

Solar oscillations can be observed by doppler velocity measurements and variations in the total continuum intensity of the solar disk. Dedicated observations are made from networks of small solar telescopes like Global Oscillation Network Group (GONG, Harvey et al. [1996]), and Birmingham Solar Oscillation Network (BiSON, Chaplin et al. [1996]) or using space borne instruments onboard the Solar and Heliospheric Orbiter (SOHO, Domingo et al. [1995]), which has Michelson Doppler Imager (MDI, Scherrer et al. [1995], Duvall et al. [1997]), Variability of solar IRradiance and Gravity Oscillations (VIRGO, Fröhlich et al. [1995] and Global Oscillation at Low Frequencies (GOLF, Gabriel et al. [1995]) instruments and Helioseismic and Magnetic Imager (HMI, Scherrer et al. [2012]) onboard Solar Dynamics Observatory (SDO, Pesnell [2015]) for studying solar oscillations.

1.3 The Solar Exterior

1.3.1 Photosphere

Photosphere is the spherical layer of light that is usually seen in visible wavelengths. The photosphere's temperature is ≈ 6000 K.

In the optical spectrum, a lot of absorption lines are seen in the long wavelength regime, while emission lines are observed in UV wavelengths. These lines can be used to estimate the temperature and height at which they are formed.

Images of the photosphere reveal that there are covective regions of 1000 km scales, with life time in minutes, called granules. Granules are caused by currents in the convective zone (see Figure 1.3). This causes cell-like structures to appear on the surface, directly above the convective zone. The center of a granule consists of the hot plasma, which floats in from the convection zone. The descending cooler plasma gives the edge of the granules a dark colour.

There exists a network of magnetic fields in the photosphere, whose scale lengths vary from a few km to several hundreds. They can be studied using Zeeman effect and spectropolarimetric inversion, using which photospheric Line of sight magnetic fields can be estimated.

Sunspots, regions that are cooler than the background, occur in the photosphere. They are regions of high magnetic fields, which inhibits convection, thus decreasing the effective temperature around it. They appear in opposite magnetic polarity, and the number of sunspots vary with a periodicity of 11 years. Solar Flares and Mass ejections have been found to originate close to regions around sunspots.

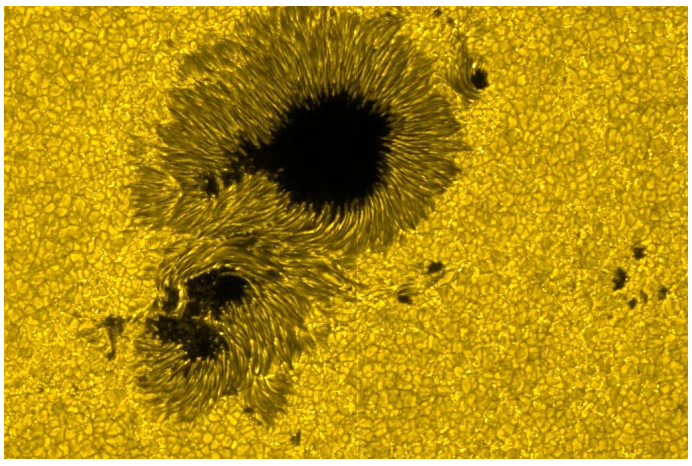

Figure 1.3: Granules seen around a sunspot in the photosphere (Picture courtesy: `https://en.wikipedia.org/Granule_(solar_physics)`).

1.3.2 Chromosphere

The chromosphere is the region between the photosphere and the transition region. It is around 3000-5000 km deep. A lot of spicules arise from the homogeneous chromosphere, above the photosphere, and extend to 10,000 kms into the Corona(see Figure 1.4). The chromosphere is a thousand times less dense than the photosphere. The temperature decreases to a minimum of 4000 K, but as we move outward towards the transition region and the corona, it goes upto 35000 K.

The chromosphere can be studied by observing its spectrum, which is dominated by emission lines. A widely used tool is to study it at Hα wavelengths of 656.3 nm, which is emitted when a hydrogen atom transitions from n=3 to n=2 levels.

The chromosphere can also be observed in radio wavelengths, but due to the increase in electron density in there, the plasma becomes optically thick to radio emission. So only the outer-most layers of the chromosphere can be observed.

During observations, a prominent feature that stands out are the spicules. These components last for 15 minutes and appear as elongated fibres. They have been observed to be associated with regions of high magnetic activity. The rise at high speeds, reach into transition region and portions of low corona before fading away.

Another notable component are filaments(see Figure 1.5) and prominences (which are side view of filaments), which rise up from the photosphere and pass through the chromosphere into the Corona, and are believed to be precursors for Coronal Mass Ejections.

1.3.3 Corona

The Sun's atmosphere is called the corona [Aschwanden 2006]. The reason for it name is due to the fact that it appears like a crown around the moon during solar eclipses (see Figure 1.6). The visible light output from the corona is very low in intensity compared to that from the photosphere. That said, the temperature of the solar corona is close to a million degrees. This is one of the open questions in solar physics.

The nature of the plasma in the corona is very tenuous. The plasma

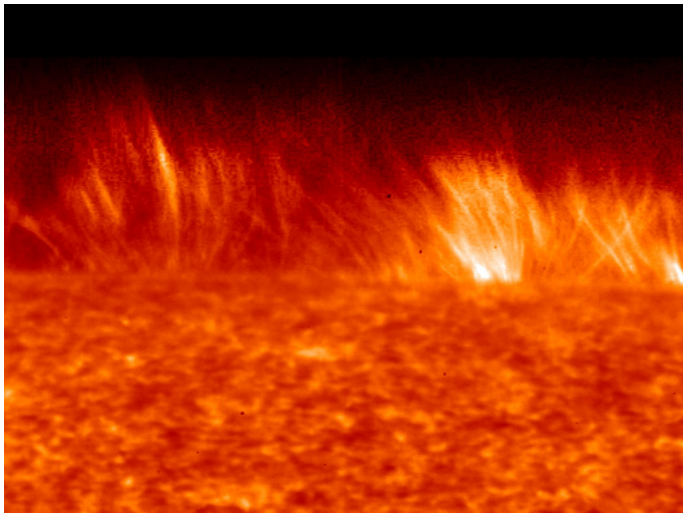

Figure 1.4: Spicules in chromosphere observed using Hinode Spacecraft (Picture courtesy: `https://www.nasa.gov/mission_pages/iris/news/interface-region.html`).

electron density decreases as we move away from the low corona. The clear boundaries of the corona is not known. It is believed to extend into the heliosphere before it transitions into the solar wind.

Regular observations of the corona started with the invention of the coronograph by Lyot [Lyot 1939], who designed a telescope with an occulter which served to block the bright photospheric light.

There are multiple structures found in the solar corona, which are enumerated below.

1. Active Regions, which are loop structures connecting magnetically opposite polar points in the photosphere. They are also called coronal loops. The temperature and density in loops may be 2-4 MK and $10^{9-10} cm^{-3}$. These regions are directly linked to the magnetic field occurring at different heights above the solar surface. They can be connected to Hα filaments, plages and prominences in the chromosphere, and spicules and flaculae in the photosphere, and flares and mass ejections in the corona. Due to the heightened activity close to them, they are believed to be the cause of CMEs and Flares.

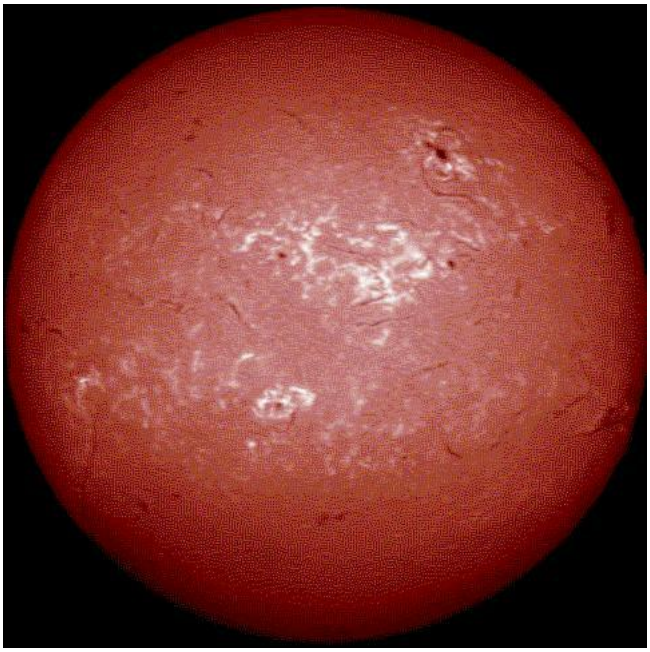

Figure 1.5: Chromospheric Filaments are seen in Hα as dark elongated features (Picture courtesy: `https://en.wikipedia.org/wiki/Chromosphere`).

2. Large-scale structures are long arcs that contain very low density plasma compared to the loops of active region. It changes over the solar cycle.

3. Filament cavities and bright points are also found in the corona. The former are zones on the corona, which appear with lower intensity in the X-ray images. They are usually found above Hα filaments over the atmosphere. They appear dark because of the lower temperature of the clouds that cause them, which are buoyant due to the Sun's magnetic field. On the contrary, bright points are active regions on the solar disks when seen in X-Ray. They are associated with smaller bipolar magnetic regions. Their temperature varies between 1 - 3 MK, and are correlated with the changes in X-ray emission.

4. Coronal Holes occur when the magnetic field of the Sun is open to interplanetary space. These regions are found in areas of low

Figure 1.6: The Corona during a solar eclipse (Picture courtesy: `https://spaceplace.nasa.gov/sun-corona/en/`).

electron densities, and are sources of high speed solar wind. They can be observed in X-Ray and radio images as patches of low intensity. They extend from Sun's equator to poles, or in some cases, from pole to pole also. Coronal holes are the cause of geomagnetic storms and increased particle activity during solar minimum.

Events with particular significance to space weather originate in the solar corona. Primary of these events is the Coronal Mass Ejection (CME, see Figure 1.7), which is a mass of plasma of few megatons, that is ejected into the interplanetary space. These events, when strong enough, bombard the earth's magnetic field, giving rise to geomagnetic storms. Of significance is the Halo-CME (see Figure 2.6), which are signature of earth directed events.

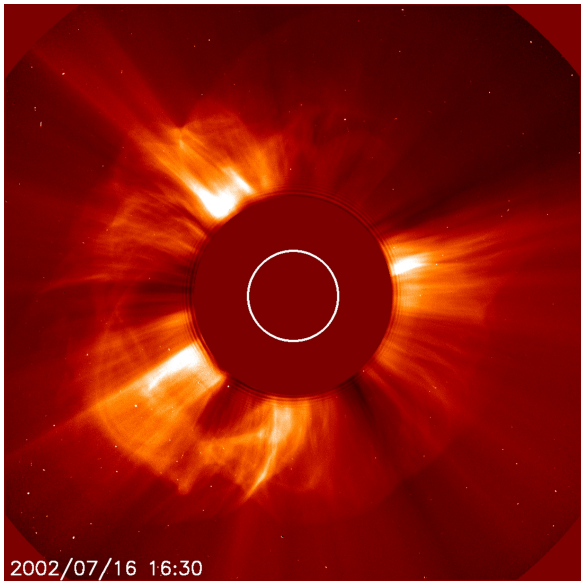

Figure 1.7: A Halo CME observed using the Large Angle Scattering COronograph (LASCO-C2) onboard the SOHO spacecraft (Picture courtesy: `https://soho.nascom.nasa.gov/gallery/images/large/20020716c2halo.jpg`).

1.3.4 Solar Wind

The corona keeps expanding outward continuously. This gives rise to a stream of ionized particles which travel outward into the interplanetary space, which is called the Solar Wind [Manoharan 2003]. The solar wind is accelerated to a large extent with a distance of 15 $R_\odot$ from the Sun. When it reaches the earth, the wind's average speed is $\approx$ 400 km/s.

The existence of the solar wind was initially postulated by Biermann et al. [1967], based on observations of the tails of Comets. This was further built up on by Parker [1965] who suggested that the solar atmosphere is in a state of continuous expansion, and gave a generalized view of the variation of temperature with distance of Sun.

The flow of the solar wind is tightly linked to the coronal magnetic fields. Regions of strong magnetic fields obstruct the flow of the wind, while regions with radial magnetic fields allow the wind to flow more freely. Due to above reason, and also the Sun's rotation about its axis,

the magnetic field tends to take the shape of an Archimedean Spiral. The strength of the interplanetary magnetic field close to Earth is $\approx 5 \times 10^{-5}$. At a distance of 12 Earth Radii, the interplanetary and terrestrial magnetic fields reach an equilibrium point, and at this point, the solar wind particles start to travel along the magnetic field lines, causing geomagnetic storms and aurora.

Figure 1.8 shows the observations of solar wind by the Ulysses spacecraft between two solar minimums [Bame et al. 1992]. Note that the flow of the fast and slow wind are almost symmetrical during solar maximum, but is pinched close to equator during the times of solar minimum. Also note the flip in the direction of the interplanetary magnetic fields between the two solar minimums.

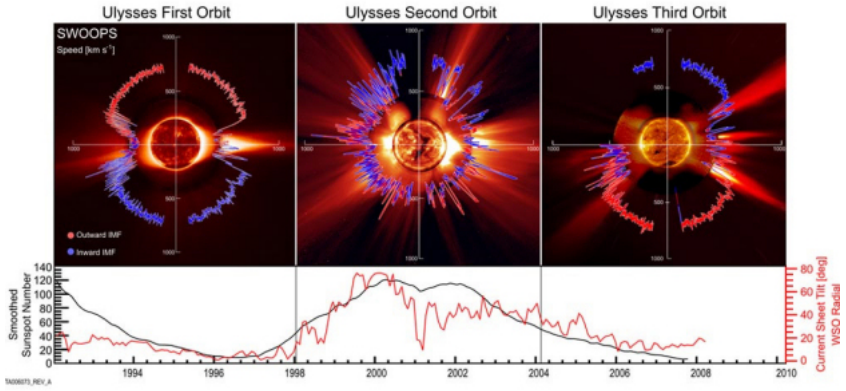

Figure 1.8: Solar wind during a full solar cycle, from minimum to maximum to minimum again. (Picture courtesy: `http://sci.esa.int/ulysses/43461-polar-plots-of-the-solar-wind-speed/`).

Solar wind can be studied using a variety of techniques. Space based instruments use particle/ion detectors, measuring their densities *in-situ*. Ground based observations can be performed using a technique called interplanetary scintillation, where the scattering of radiation from distant point sources due to electron density inhomogeneties caused by solar wind flow. By measuring the modulation of the wave-front's phase, properties of solar wind at the particular elongation of the source can be studied. Using sources at multiple elongations, a map of the solar wind speed at

various directions can be constructed.

1.4 A brief review of Solar Radio Astronomy

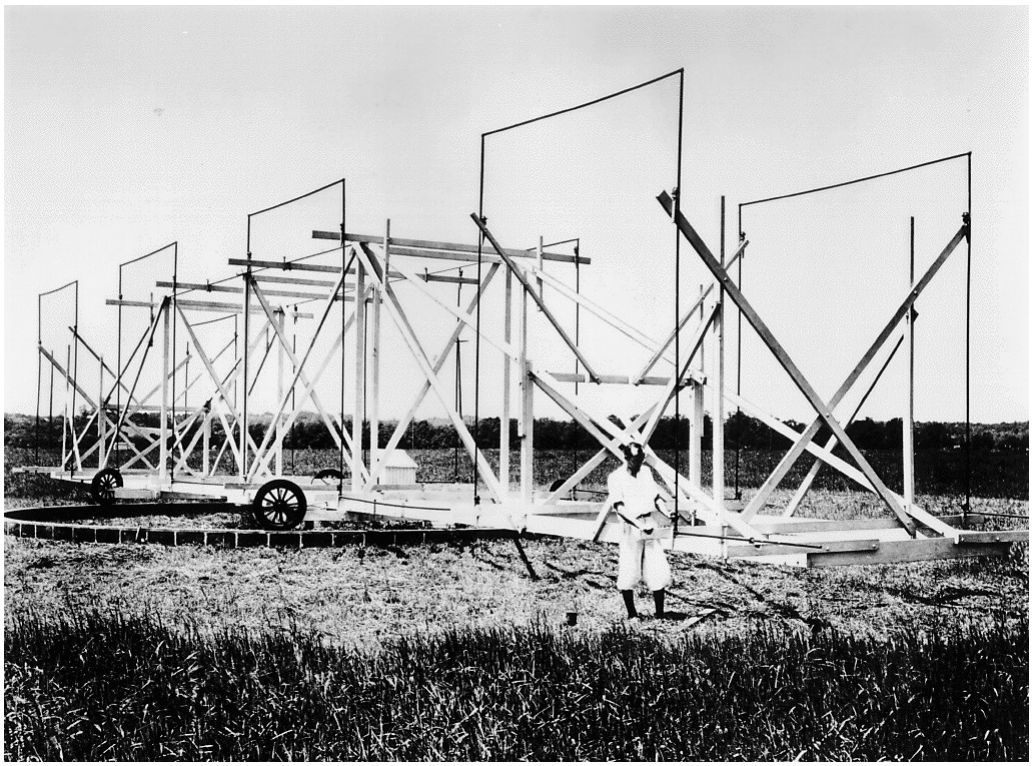

Figure 1.9: The antenna used by Karl Jansky, using which he serendipitously discovered radio emission from the Galaxy. (Picture courtesy: `https://www.nrao.edu/whatisra/`).

Karl Jansky was an engineer with Bell Labs, where he was tasked with studying the effects of static on trans atlantic communication links. Using a large directional antenna, he found a signal in his data recorder, which peaked once in every 24 hours (see Figure 1.9). On close analysis and discussions with other astronomers, he concluded that the peak of the radiation coincided with the time at which the galactic center transited the antenna.

Grote Reber, inspired by Jansky's discovery, set up his own facility at

his backyard, for observation of sky at different wavelengths and made the first radio map of the sky, shown in Figure 1.10.

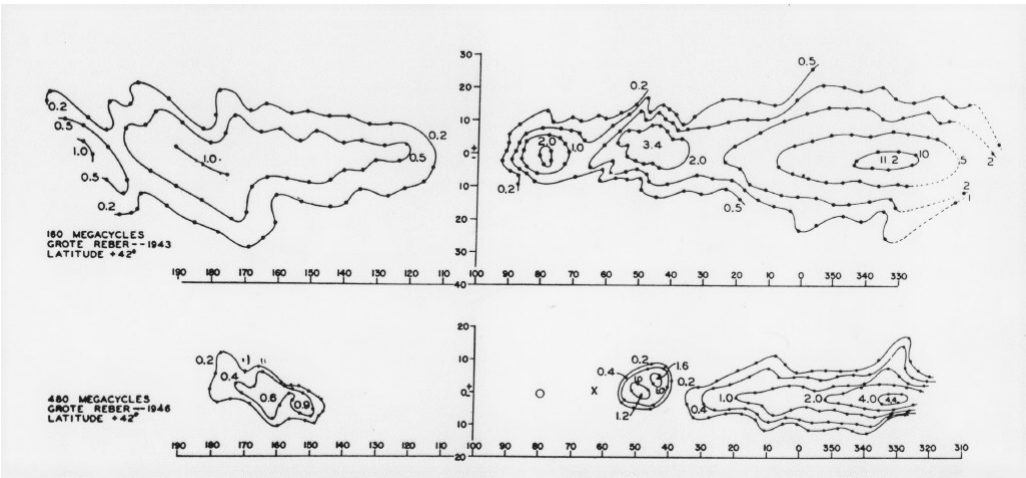

Figure 1.10: First map of the Radio Sky made by Grote Reber using observations at 160 MHz and 480 MHz (Picture courtesy: `https://www.nrao.edu/whatisra`).

During the World War 2, around 1942, the English Radars along the eastern coast of British Isles picked up an excess noise-like signal. For a long time, this signal was thought to be originating from a German Radar jammer. But subsequent analysis of the obtained signal showed that it was not of terrestrial origin, and was correlated with the appearance of a giant sunspot on the Sun. The results were summarized in an article after the end of World War 2 by Hey et al. [1948].

Around the late forties, Commonwealth Scientific and Industrial Research Organization (CSIRO), Australia, initiated a research program in radio astronomy. The main purpose of this was to study compact radio sources, and understand the mechanism behind radio emission from the Sun. Antennas working at 200 MHz were used for initial observations. These were used in the form of a *Sea-cliff Interferometer* (see Figure 1.11). The instrument worked based on the principle that superposition of the direct and the reflected ray from the source will combine at the antenna plane to form fringes. The higher the antenna was, the finer the fringes. These antennas gave resolutions $\sim 10'$. The antennas had only azimuthal

degree of freedom, due to which the sources could be observed only when they were rising. The results from the above instrument, shown in Figure 1.12 indicated that the radio signal from the Sun, which was noise-like, was highly variable. A correlation study with data from the interferometer and solar observations from Mt. Stromlo showed that the total radio noise power was correlated with the number of visible sun-spots. Observations also showed that the brightness temperatures were $\sim 0.5 - 15{\times}10^6$ [McCready et al. 1947], which was atleast 3 orders of magnitude greater than the observed 6000 K of the visible Sun. Observations using this interferometer during the time of a giant sun-spot gave clear sinusoidal interference patterns, indicating the presence of compact structures, smaller than 10′ on the Sun.

Figure 1.11: The Sea Interferometer at Dover Heights (Picture courtesy: `https://www.atnf.csiro.au/outreach/about/history/doverheights/index.html`).

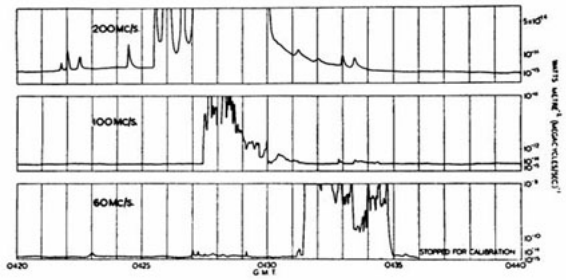

Figure 1.12: Solar Observations using the Sea Interferometer (Picture courtesy: `https://www.atnf.csiro.au/outreach/about/history/doverheights/index.html`). Note the saturation of the receiver during times of high solar activity.

From the daily data, it was found that the intensity of the solar radio noise had a sharp lower limit corresponding to $\approx 10^6 K$ [Pawsey and Yabsley 1949]. Around the same time, results using recent studies of ionization states and spectral-line widths suggested that the solar corona could be a million degrees. David Martyn used techniques of ionospheric electromagnetic wave propagation to estimate the regions whence the observed low frequency radio emission originated [Martyn 1946, 1948]. After adopting an appropriate model for the distribution of the electrons in the corona, he found that the aforementioned radiation would arise from the corona, and not from the photosphere, which was only 6000 K.

In England, Martin Ryle and Derek Vonberg came up with the idea of a two element interferometer [Ryle and Vonberg 1946, 1948]. The interferometer would consist of two small antennas spaced at a distance dictated by the required angular resolution, and the signals from the antennas would be combined by cables(see Figure 1.13). The advantage of this type of interferometer was that it was physically realizable to achieve arbitrary distance, and sources could be observed and tracked for longer times than in a sea interferometer, where the observation times were restricted to the source-rise times. The scheme of the interferometer was analogous to the optical interferometer used by Michelson for stellar interferometry. Ryle and Vonberg used this interferometer to observe the Sun, and found results those were in agreement with that of the Australian Group. They also

verified that the radiation was predominantly circularly polarized.

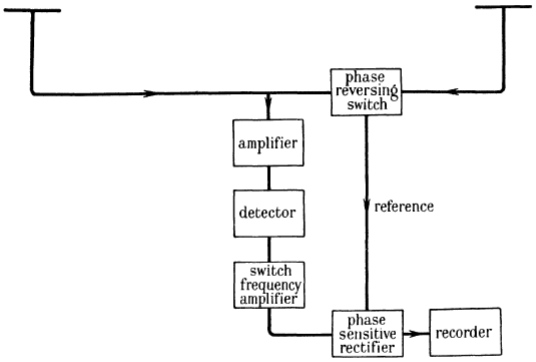

Figure 1.13: Scheme of the phase switching interferometer [Ryle and Vonberg 1948].

The early observations of solar radiation were carried out with instruments tuned to specific observation frequencies. For one to infer the spectral nature of the observed radiation, simultaneous observations of the same burst at different frequencies were required. In 1950, J. P. Wild and L. L. McCready designed an instrument that would be capable of recording the dynamic spectrum[4] of these radio bursts [Wild and McCready 1950]. The instrument operated within the continuous frequency range of 70 – 130 MHz. The receiver was a swept frequency spectrum analyzer, where the local oscillator of a superheterodyne receiver was continuously tuned to traverse the frequency axis. The amplified intermediate frequency output was connected to the Y-axis of a cathode ray oscilloscope, providing a Intensity vs. frequency curve in the display. The calibration of the instrument was carried out by injecting signals of known amplitudes and frequencies before the commencement of actual observations. Based on observations with these experiments, they found three types of bursts to

[4]The variation of the frequency spectrum with time is called the dynamic spectrum

be dominant, and they classified it as Type I, Type II and Type III bursts [Wild and McCready 1950, Wild 1950].

Type I bursts occurred in large numbers and lasted from a hour to a few days. These bursts are accompanied with background continuum emission. These bursts were noted to occur all over the frequency band. A detailed description of these bursts and their mechanism is discussed in 5 of this thesis.

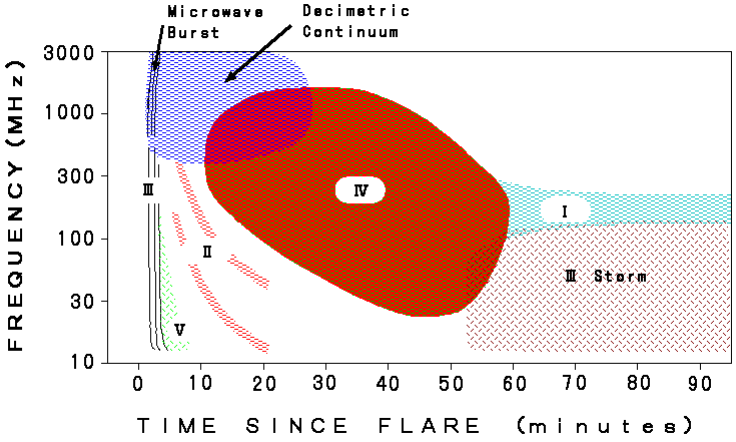

Figure 1.14: Different Solar Radio bursts and their classification in time frequency space (Image courtesy: `http://sunbase.nict.go.jp/`)

Type II bursts were rarer compared to type I bursts. These bursts were characterized by a sharp start and stop frequency cut-offs, and drift across the dynamic spectrum slowly at the rate of $0.1 - 1\,MHz/s$. These bursts last in time for $\approx 10 - 20$ minutes. These bursts were associated with disturbances slowly traversing the coronal plasma.

Type III bursts were fast drift bursts, that occurred more frequently than Type II bursts. The drifts were of the order of $\approx$ 10s of MHz. They lasted for a few seconds in time. These bursts were associated with rapidly travelling disturbances in the solar corona. Observations of a variant of this burst, Type IIIb forms the matter of discussion of 4.

Type IV bursts was independently discovered by A. Boischot [Boischot 1957]. These bursts were signatures of slowly moving disturbances in the solar corona. These bursts were characterized by a slowly drifting broad-

band continuum [Kundu 1962]. Type IV bursts also frequently occur in the microwave regime [Güdel and Benz 1988].

Type V [Weiss and Stewart 1965] bursts are similar to type III bursts, but they exhibit a continuum which is long-lived compared to the drifting signature of Type III bursts. They are usually preceded by a type III burst. The time frequency characteristics of all the aforementioned bursts is summarized in Figure 1.14.

While observations using a two element interferometer were successful in studies of the time frequency characteristics of the solar radio bursts, there was interest to image them. An initial attempt at this was the Christiansen Grating array [Christiansen and Mathewson 1958, Christiansen et al. 1961]. One of the main objective of this instrument was to study the quiet sun, and a second slowly varying component [Christiansen and Mathewson 1959] in detail and obtain information about the solar disk at radio frequencies.

The idea behind Grating array was to generate multiple beams pointing at the sky, and let the source to drift over these beams. This would provide an increased observing time along with improved angular resolution. This was realized by uniformly spacing antennas at distances of several wavelengths and combining the signals from them. The array was constructed with 32 elements operating at 1420 MHz, and had a beamwidth of 2.9 ′, with a spacing of 1.7 °. This ensured that only one beam would be on the 30 sun at any instant. The output of the array was one dimensional scan across the solar disk at 1420 MHz. Over averaging scans obtained over multiple days, the base level of the emission was found to be around 7×10^4 K. It was also observed that the radio Sun was larger than the optical Sun and evidences of limb-brightening were observed. The latter was attributed to the optical depth of the corona, which has a higher temperature than the photosphere. Two dimensional maps of the quiet sun was obtained when an additional grating arm was added in the north south direction.

The experience from the aforementioned observations were used in the construction of the Culgoora Radioheliograph [Sheridan et al. 1972], which made the first 2-D images of the Sun. A variety of bursts and their source regions were studied using this instrument over the years [Sheridan et al. 1983].

A similar instrument was established in the United States by Erickson and collaborators, and was called the Clark Lake Radio Heliograph [Erickson et al. 1982]. This instrument used Conical Log Spiral antennas as the primary element, and diode phase shifters were used to select different spirals to enable beam pointing. Maps of quiet sun, micro-type III bursts and solar noise storms were obtained using this instrument at multiple interference free spot frequencies [Kundu et al. 1983, Thejappa et al. 1990].

After a successful observing run, both the above instruments were decommissioned, leaving behind a void in solar radio imaging observations at low frequencies. Spectral observations were made on a regular basis by a network of radio spectrometers world-wide called Compound Astronomical Low cost Low frequency Instrument for Spectroscopy and Transportable Observatory (CALLISTO, Benz et al. [2005]).

1.5 Solar Radio Astronomy at Indian Institute of Astrophysics (IIA)

Solar Radio Astronomy at IIA has its roots in the Kodaikanal solar observatory. Initial observations of Sun and scinitllation from other discrete sources were conducted at frequencies of 100 and 200 MHz using Yagi antenna elements, and Dicke receiver [Dicke 1946]. A 3-m interferometer was also in operation, which was used to synchronously observe noise-storms with solar magnetically active regions [Das and Bhargava 1953].

After this initial success, a new multi-element observational system was installed at the observatory to carry-out observations at frequencies as low as 25 MHz, which was used for observing solar bursts [Sastry 1971]. In the early '70s, a decameter array was established with a phase switched receiver for studying the occultation of the radio source Tau-A by the solar corona [Sastry and Subramanian 1974].

During the late '70s, a new field station at Gauribidanur was established in collaboration with Raman Research Institute, and a decameter synthesis telescope was built to operate at 34.5 MHz [Sastry 1983]. The array had $\approx$ 1000 dipoles, arranged like a 'T'. The sensitivity of this array was ≈ 10 Jy [5].

[5] $1\text{Jy} = 10^{-26} W m^{-2} Hz^{-1}$

Using this array, the first decametric maps of the slowly varying component of the Sun were synthesized [Sastry et al. 1981a]. Fine structures of solar bursts were also studied using high spectral resolution receivers [Thejappa and Sastry 1982, Sastry et al. 1981b].

The building of the Gauribidanur RAdioheliograPH (GRAPH) began during the early 1990s [Ramesh et al. 1998, Ramesh et al. 1998]. It was initially an array of 192 log periodic antennas, built to operate in the frequency range of 40-120 MHz. Initial results using only the EW arm of the array yielded results on the electron density in the outer corona at two heliocentric distances.

The array was also used to image "Halo" CMEs (refer Section 1.3.3) and reinforced the use of radio observations to space weather [Kathiravan and Ramesh 2005]. Subsequently, to study the magnetic fields of quiet and active Sun using polarimetry, the Gauribidanur Radio Interferometric Polarimeter (GRIP, [Ramesh et al. 2008]) was commissioned. A wideband instrument to observe the spectral characteristics of radio bursts, called the Gauribidanur RAdio Solar Spectrograph (GRASS, Ebenezer et al. [2007]) was designed to operate in the range of 30 – 150 MHz. This was later upgraded to Gauribidanur Low Frequency Solar Spectrograph (GLOSS, Kishore et al. [2014]), which operates in the frequency range of 40 – 450 MHz.

Using these instruments, a wide range of significant results like estimates of coronal magnetic fields when the Sun was both quiet and active [Ramesh et al. 2010b, 2011b, Hariharan et al. 2014, Kumari et al. 2017a,b], observations of arc-second scale sources using the lunar occultation technique [Kathiravan et al. 2011, Ramesh et al. 2011a], statistics of source regions of type II radio bursts and their relation to CME locations [Ramesh et al. 2010a, 2012a], observations of quasi-periodic behaviour of radio bursts [Raja and Ramesh 2013, Hariharan et al. 2016] and observations of picoflare category energy releases [Ramesh et al. 2012b] to name a few.

To improve the sensitivity, resolution and duty cycle of the observations, an upgrade of the existing facilities were proposed, an initial exploration of which is the subject matter of this thesis.

1.6 Prologue to the Thesis

The Antenna systems currently operational at the Gauribidanur Radio Observatory are capable of operating in a wide range of frequencies (40 – 120 MHz). The receiver chain being used is a super-heterodyne receiver, with a tunable local oscillator. The IF signal is at 10.7 MHz, with a bandwidth of 1 MHz. The signal from the analog chain is digitized with a 1-bit quantization, and is sampled at 4 MHz rate by a D-Flip-Flop, before being fed into a Application Specific Integrated Circuit (ASIC) based correlator, and the correlation counts are saved at the end of every integration time [Ramesh et al. 2006].

In the aforementioned system, we see that while the antenna is capable of operating at a wide band of frequencies, the system is limited by the digital backend, which during the time of commissioning the array was state of art. But the recent development in electronics, has enabled development of mixed signal components capable of operating at wide-bandwidths. Refitting the backends of the primary instruments, namely GRAPH and GRIP, which use the legacy systems, will yield a wealth of scientific information about the solar corona and events of significance there.

From a scientific stand point, all Solar Radio events are triggered by some activity close to the surface of the Sun, and are produced by electron acceleration provided by these "triggers". So, inherently, these events are wide-band in nature. Secondly, due to the fact that the coronal plasma is stratified, the plasma frequency decreases continuously as we away from the Sun. This results in emission at different frequencies originating at different heights. Thus a broad-band receiver system to an existing imaging instrument like GRAPH, will provide us with three dimensional information of the solar corona.

A similar system for GRIP will allow us to study the polarization of the electromagnetic radiation, and probe the magnetic fields as a function of height.

For spectro-graphic and spectro-polarimetric instruments like the GLOSS and Gauribidanur Radio Solar SpectroPolarimeter (GRASP, Kishore et al. [2015]) would also benefit from digital backends, and will obtain a sensitivity boost and allow us to study weaker events with better contrast.

GRAPH, being the only existing solar dedicated radio imaging instru-

ment, is also undergoing a expansion program, which is scheduled to occur in three phases: In the first phase, the number of primary elements have been increased to ≈ 400 antennas, which provides an increased sensitivity. In the second phase, it has been proposed to upgrade the digital backend to enable wide-band imaging observations. In the third phase, it is planned to increase the longest baseline upto 10 kms to enhance the angular resolution to arc-minute scales.

This thesis explores the technical and scientific feasibility of the instrument upgrades. In chapter 3, a description of a Long baseline interferometer experiment to observe the solar corona is provided. We discuss the science objectives, the instrument development and the results obtained from it, and its importance from the point of view of GRAPH expansion.

In chapter 4, the design and development of wide-band digital spectrometers for GLOSS is covered. The results obtained with the backend, and how observations of fine structures in the corona with such high resolution backends, can provide information on turbulence in the low corona is discussed.

Chapter 5 discusses the end-to-end system design of a wide-band spectropolarimetric array, and noise storm observations with it, along with the enhancements obtained due to the usage of a wide-band digital backend. We conclude in Chapter 6, by summarizing the results from individual chapters and future vision.

References

Ahmad, Q. R., Allen, R., Andersen, T., Anglin, J., Barton, J., Beier, E., Bercovitch, M., Bigu, J., Biller, S., Black, R., et al. (2002). Direct evidence for neutrino flavor transformation from neutral-current interactions in the sudbury neutrino observatory. *Physical review letters*, 89(1):011301.

Aschwanden, M. (2006). *Physics of the solar corona: an introduction with problems and solutions*. Springer Science & Business Media.

Babcock, H. W. and Babcock, H. D. (1955). The sun's magnetic field, 1952-1954. *The Astrophysical Journal*, 121:349.

Bahcall, J. N. (1964). Solar neutrinos. i. theoretical. *Physical Review Letters*, 12(11):300.

Bame, S., McComas, D., Barraclough, B., Phillips, J., Sofaly, K., Chavez, J., Goldstein, B., and Sakurai, R. (1992). The ulysses solar wind plasma experiment. *Astronomy and Astrophysics Supplement Series*, 92:237–265.

Benz, A. O., Monstein, C., and Meyer, H. (2005). Callisto–a new concept for solar radio spectrometers. *Solar Physics*, 226(1):143–151.

Bethe, H. A. (1939). Energy production in stars. *Physical Review*, 55(5):434.

Biermann, L., Brosowski, B., and Schmidt, H. (1967). The interaction of the solar wind with a comet. *Solar Physics*, 1(2):254–284.

Boger, J., Hahn, R., Rowley, J., Carter, A., Hollebone, B., Kessler, D., Blevis, I., Dalnoki-Veress, F., DeKok, A., Farine, J., et al. (2000). The sudbury neutrino observatory. *Nuclear Instruments and Methods in Physics Research Section A: Accelerators, Spectrometers, Detectors and Associated Equipment*, 449(1-2):172–207.

Boischot, A. (1957). Caractères d'un type d'émission hertzienne associé à certaines éruptions chromosphériques. *Academie des Sciences Paris Comptes Rendus*, 244:1326–1329.

Burgess, E. (1978). Translation of the surya-siddhanta, a text-book of hindu astronomy: with notes and an appendix. *Minneapolis: Wizards Book Shelf, c1978.*

Carrington, R. C. (1863). *Observations of the Spots on the Sun from November 9. 1853, to March 24, 1861, Made at Redhill*. Williams and Norgate.

Chaplin, W., Elsworth, Y., Isaak, G., Lines, R., McLeod, C., Miller, B., New, R., and van der Raay, H. (1996). Observing the sun with the birmingham solar-oscillations network (bison). *The Observatory*, 116:32–33.

Christiansen, W. and Mathewson, D. (1958). Scanning the sun with a highly directional array. *Proceedings of the IRE*, 46(1):127–131.

Christiansen, W. and Mathewson, D. (1959). The origin of the slowly varying component. In *Symposium-International Astronomical Union*, volume 9, pages 108–117. Cambridge University Press.

Christiansen, W. N., Labrum, N., McAlister, K., and Mathewson, D. (1961). The crossed-grating interferometer: a new high-resolution radio telescope. *Proceedings of the IEE-Part B: Electronic and Communication Engineering*, 108(37):48–58.

Das, A. K. and Bhargava, B. N. (1953). Radio noise-bursts from solar m-regions. *Nature*, 172(4384):855.

Davis Jr, R. (1964). Solar neutrinos. ii. experimental. *Physical Review Letters*, 12(11):303.

Dicke, R. H. (1946). The measurement of thermal radiation at microwave frequencies. In *Classics in Radio Astronomy*, pages 106–113. Springer.

Domingo, V., Fleck, B., and Poland, A. (1995). Soho: the solar and heliospheric observatory. *Space Science Reviews*, 72(1-2):81–84.

Duvall, T. L., Kosovichev, A., Scherrer, P., Bogart, R., Bush, R., De Forest, C., Hoeksema, J., Schou, J., Saba, J., Tarbell, T., et al. (1997). Time-distance helioseismology with the mdi instrument: initial results. In *The First Results from SOHO*, pages 63–73. Springer.

Ebenezer, E., Subramanian, K. R., Ramesh, R., Sundararajan, M. S., and Kathiravan, C. (2007). Gauribidanur radio array solar spectrograph (GRASS). *Bulletin of the Astronomical Society of India*, 35:111–119.

Eddy, J. A. (1976). The maunder minimum. *Science*, 192(4245):1189–1202.

Erickson, W., Mahoney, M., and Erb, K. (1982). The clark lake teepee-tee telescope. *The Astrophysical Journal Supplement Series*, 50:403–419.

Filonik, J. (2013). Athenian impiety trials: a reappraisal. *Dike-Rivista di Storia del Diritto*

Greco ed Ellenistico, 16:11–96.

Fröhlich, C., Romero, J., Roth, H., Wehrli, C., Andersen, B. N., Appourchaux, T., Domingo, V., Telljohann, U., Berthomieu, G., Delache, P., et al. (1995). Virgo: Experiment for helioseismology and solar irradiance monitoring. *Solar Physics*, 162(1-2):101–128.

Gabriel, A., Grec, G., Charra, J., Robillot, J.-M., Cortés, T. R., Turck-Chièze, S., Bocchia, R., Boumier, P., Cantin, M., Cespédes, E., et al. (1995). Global oscillations at low frequency from the soho mission (golf). In *The SOHO Mission*, pages 61–99. Springer.

Güdel, M. and Benz, A. (1988). A catalogue of decimetric solar flare radio emission. *Astronomy and Astrophysics Supplement Series*, 75:243–259.

Hale, G. E. (1908). The tower telescope of the mount wilson solar observatory. *The Astrophysical Journal*, 27:204.

Hariharan, K., Ramesh, R., Kathiravan, C., Abhilash, H., and Rajalingam, M. (2016). High dynamic range observations of solar coronal transients at low radio frequencies with a spectro-correlator. *The Astrophysical Journal Supplement Series*, 222(2):21.

Hariharan, K., Ramesh, R., Kishore, P., Kathiravan, C., and Gopalswamy, N. (2014). An estimate of the coronal magnetic field near a solar coronal mass ejection from low-frequency radio observations. *The Astrophysical Journal*, 795(1):14.

Harvey, J., Hill, F., Hubbard, R., Kennedy, J., Leibacher, J., Pintar, J., Gilman, P., Noyes, R., Toomre, J., Ulrich, R., et al. (1996). The global oscillation network group (gong) project. *Science*, 272(5266):1284–1286.

Hey, J. S., Parsons, S. J., and Phillips, J. W. (1948). Some Characteristics of Solar Radio Emissions. *Mon. Not. Roy. Astron. Soc.*, 108:354.

Kathiravan, C. and Ramesh, R. (2005). Identification of the Source Region of a "Halo" Coronal Mass Ejection Using Meter-Wavelength Radio Data. *Astrophys. J. Lett.*, 627:L77–L80.

Kathiravan, C., Ramesh, R., Barve, I. V., and Rajalingam, M. (2011). Radio observations of the solar corona during an eclipse. *The Astrophysical Journal*, 730(2):91.

Kishore, P., Kathiravan, C., Ramesh, R., Rajalingam, M., and Barve, I. V. (2014). Gauribidanur Low-Frequency Solar Spectrograph. *Solar Phys.*, 289:3995–4005.

Kishore, P., Ramesh, R., Kathiravan, C., and Rajalingam, M. (2015). A Low-Frequency Radio Spectropolarimeter for Observations of the Solar Corona. *Solar Phys.*, 290:2409–2422.

Kochhar, R. (2002). Madras and kodaikanal observatories: a brief history. *Resonance*, 7(8):16–28.

Kumari, A., Ramesh, R., Kathiravan, C., and Gopalswamy, N. (2017a). New evidence for a coronal mass ejection-driven high frequency type ii burst near the sun. *The Astrophysical Journal*, 843(1):10.

Kumari, A., Ramesh, R., Kathiravan, C., and Wang, T. (2017b). Strength of the solar coronal magnetic field–a comparison of independent estimates using contemporaneous radio and white-light observations. *Solar Physics*, 292(11):161.

Kundu, M. R. (1962). The Nature of Type IV Solar Radio Bursts. *Journal of the Physical Society of Japan Supplement*, 17:215.

Kundu, M. R., Erickson, W. C., Gergely, T. E., Mahoney, M. J., and Turner, P. J. (1983). First

results from the Clark Lake Multifrequency Radioheliograph. *Solar Phys.*, 83:385–389.

Lyot, B. (1939). The study of the solar corona and prominences without eclipses (george darwin lecture, 1939). *Monthly Notices of the Royal Astronomical Society*, 99:580.

Manoharan, P. (2003). The solar wind. In *Lectures on Solar Physics*, pages 299–326. Springer.

Martyn, D. (1946). Temperature radiation from the quiet sun in the radio spectrum. In *Classics in Radio Astronomy*, pages 210–214. Springer.

Martyn, D. F. (1948). Solar radiation in the radio spectrum-i. radiation from the quiet sun. *Proc. R. Soc. Lond. A*, 193(1032):44–59.

McCready, L., Pawsey, J. L., and Payne-Scott, R. (1947). Solar radiation at radio frequencies and its relation to sunspots. *Proc. R. Soc. Lond. A*, 190(1022):357–375.

Parker, E. (1965). Dynamical theory of the solar wind. *Space Science Reviews*, 4(5-6):666–708.

Pawsey, J. and Yabsley, D. (1949). Solar radio-frequency radiation of thermal origin. *Australian Journal of Chemistry*, 2(2):198–213.

Pesnell, W. D. (2015). *Solar dynamics observatory (SDO)*. Springer.

Raja, K. S. and Ramesh, R. (2013). Low-frequency observations of transient quasi-periodic radio emission from the solar atmosphere. *The Astrophysical Journal*, 775(1):38.

Ramesh, R., Kathiravan, C., Barve, I. V., and Rajalingam, M. (2011a). High angular resolution radio observations of a coronal mass ejection source region at low frequencies during a solar eclipse. *The Astrophysical Journal*, 744(2):165.

Ramesh, R., Kathiravan, C., Kartha, S. S., and Gopalswamy, N. (2010a). Radioheliograph observations of metric type ii bursts and the kinematics of coronal mass ejections. *The Astrophysical Journal*, 712(1):188.

Ramesh, R., Kathiravan, C., and Narayanan, A. S. (2011b). Low-frequency observations of polarized emission from long-lived non-thermal radio sources in the solar corona. *The Astrophysical Journal*, 734(1):39.

Ramesh, R., Kathiravan, C., and Sastry, C. V. (2010b). Estimation of magnetic field in the solar coronal streamers through low frequency radio observations. *The Astrophysical Journal*, 711(2):1029.

Ramesh, R., Kathiravan, C., SundaraRajan, M. S., Barve, I. V., and Sastry, C. V. (2008). A low-frequency (30 – 110 mhz) antenna system for observations of polarized radio emission from the solar corona. *Solar Physics*, 253(1):319–327.

Ramesh, R., LAkSHMI, M. A., Kathiravan, C., Gopalswamy, N., and Umapathy, S. (2012a). The location of solar metric type ii radio bursts with respect to the associated coronal mass ejections. *The Astrophysical Journal*, 752(2):107.

Ramesh, R., Raja, K. S., Kathiravan, C., and Narayanan, A. S. (2012b). Low-frequency radio observations of picoflare category energy releases in the solar atmosphere. *The Astrophysical Journal*, 762(2):89.

Ramesh, R., Rajan, M. S., and Sastry, C. V. (2006). The 1024 channel digital correlator receiver of the gauribidanur radioheliograph. *Experimental Astronomy*, 21(1):31.

Ramesh, R., Subramanian, K., Sundararajan, M., and Sastry, C. V. (1998). The gauribidanur radioheliograph. *Solar Physics*, 181(2):439–453.

Ramesh, R., Subramanian, K. R., and Sastry, C. V. (1998). Some initial results from the Gauribidanur radio heliograph. *Bulletin of the Astronomical Society of India*, 26:233.

Ryle, M. and Vonberg, D. (1946). Solar radiation on 175 mc./s. In *Classics in Radio Astronomy*, pages 184–187. Springer.

Ryle, M. and Vonberg, D. (1948). An investigation of radio-frequency radiation from the sun. *Proc. R. Soc. Lond. A*, 193(1032):98–120.

Sastry, C. V. (1971). The time splitting of decameter solar radio bursts.

Sastry, C. V. (1983). REPORTS FROM ASTRONOMICAL CENTRES: Indian Institute of Astrophysics and Raman Research Institute. *Bulletin of the Astronomical Society of India*, 11:167–171.

Sastry, C. V., Dwarakanath, K. S., Shevgaonkar, R. K., and Krishan, V. (1981a). Observations and interpretation of the slowly varying component of solar radio emission at decameter wavelengths. *Solar Phys.*, 73:363–377.

Sastry, C. V., Krishan, V., and Subramanian, K. R. (1981b). Pulsating radio emission at decametre wavelengths from the sun. *Journal of Astrophysics and Astronomy*, 2:59–65.

Sastry, C. V. and Subramanian, K. (1974). Observations on the occultation of the radio source tauras a by the solar corona during june 1971.

Scherrer, P., Bogart, R., Bush, R., Hoeksema, J.-a., Kosovichev, A., Schou, J., Rosenberg, W., Springer, L., Tarbell, T., Wolfson, C., et al. (1995). The solar oscillations investigation—michelson doppler imager. In *The SOHO Mission*, pages 129–188. Springer.

Scherrer, P. H., Schou, J., Bush, R., Kosovichev, A., Bogart, R., Hoeksema, J., Liu, Y., Duvall, T., Zhao, J., Schrijver, C., et al. (2012). The helioseismic and magnetic imager (hmi) investigation for the solar dynamics observatory (sdo). *Solar Physics*, 275(1-2):207–227.

Schwabe, H. (1844). Sonnenbeobachtungen im Jahre 1843. Von Herrn Hofrath Schwabe in Dessau. *Astronomische Nachrichten*, 21:233.

Sheridan, K., Labrum, N., and Payten, W. (1972). Multiple-frequency operation of the culgoora radioheliograph. *Nature Physical Science*, 238(86):115.

Sheridan, K., Labrum, N., Payten, W., Nelson, G., and Hill, E. (1983). Preliminary observations of solar radio sources with the culgoora radioheliograph operating at four frequencies. *Solar Physics*, 83(1):167–177.

Thejappa, G., Gopalswamy, N., and Kundu, M. R. (1990). Microbursts at meter-decameter wavelengths. *Solar Phys.*, 127:165–183.

Thejappa, G. and Sastry, C. V. (1982). Time structure of solar decametre Type III radio bursts. *Journal of Astrophysics and Astronomy*, 3:151–159.

Weiss, L. A. A. and Stewart, R. T. (1965). Solar radio bursts of spectral type V. *Australian Journal of Physics*, 18:143.

Wild, J. (1950). Observations of the spectrum of high-intensity solar radiation at metre wavelength. ii. outbursts. *Australian Journal of Chemistry*, 3(3):399–408.

Wild, J. and McCready, L. (1950). Observatioas of the spectrum of high-intensity solar radiation at metre wavelengths. i. the apparatus and spectral types of solar burst observed. *Australian Journal of Chemistry*, 3(3):387–398.

Zirker, J. B. (2002). *Journey from the Center of the Sun*.

Chapter 2

Instrumentation systems and their Characterization

2.1 Introduction

The signal received from the antennas comprising a radio telescope is Gaussian noise-like in nature. Before obtaining useful information, the signal undergoes "conditioning" like filtering, amplification and digitization. Figure 2.1 shows a typical radio astronomy signal chain [Kraus 1966].

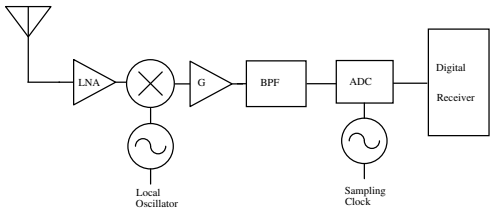

Figure 2.1: A typical Radio Astronomy Receiver system

The components can be broadly classified as Analog, mixed signal, and digital components. The signal received from the antenna is continuous in time or Analog in nature. Preliminary processing of this signal is done in the analog time domain, by amplifying; the amplified signal is isolated in frequency by making use of filters for limiting the band of the signal to a useful, usable range. This signal, based on the nature of the further

processing stages is brought to a lower frequency by a process called mixing, to facilitate processing of this signal by slower electronic components down the signal path. But recent advances in electronic technology has made it possible to bypass this mixing stage altogether [Kirichenko et al. 2009]. Based on the amplitude of the signal after processing, one more stage of amplification may be necessary before digitization.

The need for digitization is to convert the continuous time signal into a discrete time signal for further storage and processing. The first step in this process is conversion of the former to latter using a mixed-signal device called an Analog to Digital Converter (ADC). The ADC is classified as a mixed signal device as the input to it is analog in nature, while the output from it is a set of numbers, which is digital. On these numbers, further processing like correlation and spectrum analysis are carried out.

In this chapter, the theory behind these components, methods to characterize their operation in the linear and the non-linear regime, and their influence on the observed signals is discussed. While these details can be obtained from various text books [Kraus 1966, Thompson et al. 2001, Pozar 2009, Proakis and Manolakis 1996] and lecture notes [1,2], this chapter unifies all these from the view point of signal processing pertaining to radio astronomy.

2.2 Analog Systems

For characterizing analog systems, an important metric are the Scattering parameters (S-parameters) [Pozar 2009]. These parameters for a two port network (like amplifiers, filters) can be defined as:

1. S_{11}, or return loss or reflection from Port 1
2. S_{21}, or Forward Transmission/Gain (for active networks), Insertion Loss of signal when Port 1 is input, and Port 2 is output (for passive networks)
3. S_{12}, or Reverse Isolation (for Active, non symmetric networks), Insertion Loss of signal when Port 2 is input and Port 1 is output

[1] https://www.strw.leidenuniv.nl/radioastronomy/doku.php?id=ra_2015
[2] https://web.njit.edu/~gary/728/

4. S_{22}, or return loss or reflection from Port 2.

For RF networks, scattering parameters are used, rather than conventional voltage or current parameters, as at higher frequencies it is more easier to quantify signals in terms of power than voltages as the wavelength of EM waves and the size of the components become comparable.

These parameters can be obtained by connecting the two ports of the device to be characterized to a Network Analyser. The Analyser can be either scalar or vector, the difference being that the former provides only the magnitudes of the S-parameters, while the latter provides both magnitude and phases. All the S-parameter plots appearing in the subsequent sections were obtained from a Vector Network Analyser (VNA). The connection of a Device Under Test (DUT) to a VNA is shown in Figure 2.2.

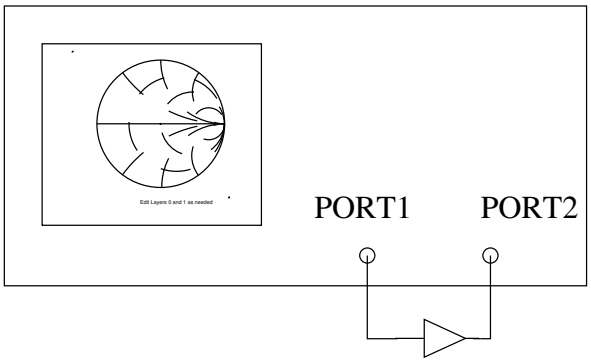

Figure 2.2: Measurement of system S-parameters using a Vector Network Analyzer

2.2.1 Amplifier

Amplifier, as the name suggests, is used for boosting the signal level. At Radio Frequencies, typically, power amplifiers are used. The amplifier uses the electrical power from a DC supply to increase the power level of the input signal. The factor by which the power of the input signal increases at the output is called Gain (G) of the amplifier. It is defined as:

$$G = \frac{P_{out}}{P_{in}}, \tag{2.1}$$

Where P_{in} and P_{out} are the input and the output powers.

Gain in terms of S-parameters is S_{21}. S_{11}, S_{22} and S_{12} provide information about the input impedance matching, the output impedance matching and isolation between the input and output ports, respectively. The measured S-parameters of a Minicircuits MAN-1LN amplifier is shown in Figure 2.3.

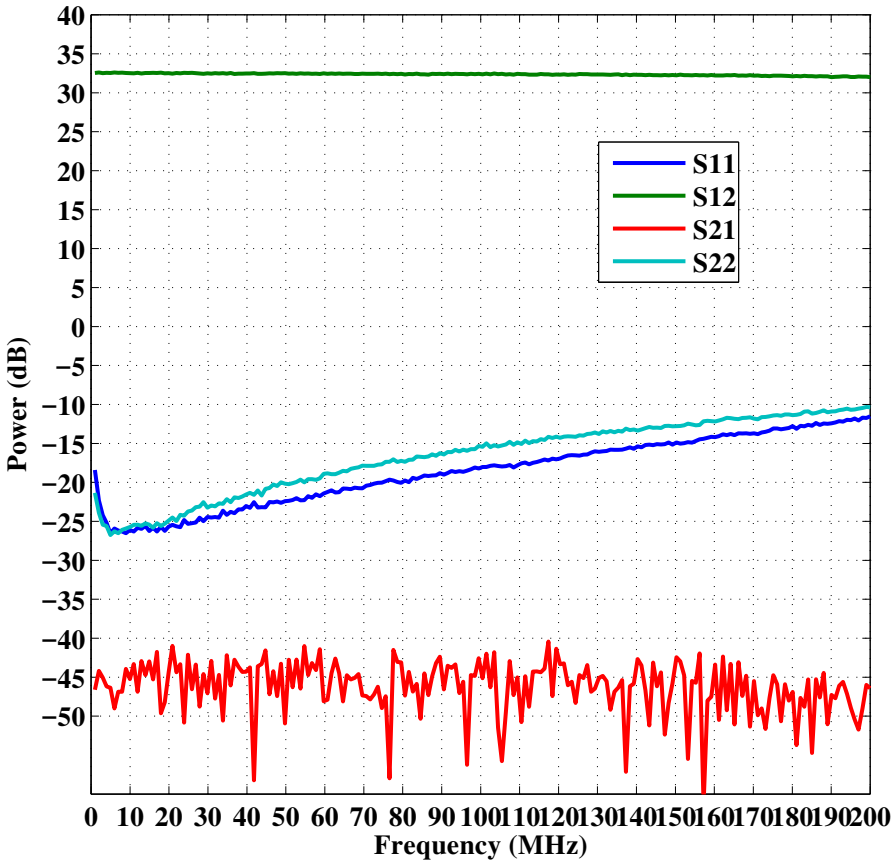

Figure 2.3: S-Parameters of MAN-1LN Amplifier from Minicircuits.

There is a range of input powers for which the amplifier operates in the linear regime. When the input power exceeds this limit, the behaviour of the amplifier becomes non-linear. In the non-linear regime, the gain starts decreasing, and the effects can be:

1. Harmonic Generation
2. Saturation, leading to reduction of amplifier gain
3. Intermodulation distortion, which arise due to products of two strong closely spaced input signals
4. Cross-modulation, leading to transfer of modulation from one signal in the band to another
5. Spectral-regrowth, which is caused to to intermodulation between many closely spaced signals in the spectrum

Of the above, all effects other than cross-modulation are important for radio receivers. Typically, these non-linearities are introduced in the receiver chain due to high levels of radio frequency interference at our frequency range, and due to high levels of radio signal from the Sun itself during times of activity. Thus, it is important to ensure sufficient signal level at the input of the receiver chain such that it is sufficient enough for obtaining good signal to noise ratio (SNR), and also does not drive the system into non-linearity.

Generally, the output response of a non-linear system to an input voltage signal, v_i is given as[3]

$$v_o = a_0 + a_1 v_i + a_2 {v_2}^2 + a_3 {v_3}^3 + \ldots \tag{2.2}$$

where v_o is the output, and the coefficients represent the dc component, linear output, squared output and other higher order outputs, respectively. The constant term represents rectification, while the linear term models attenuation or gain, typical of a filter or amplifier network, while the squared output term is used for mixing and other frequency dependent functions.

In the above case, if we consider the input signal to be a single frequency sinusoid, such that $v_i = v_0 \cos \omega_o t$, then according to Equation 2.12:

$$v_o = a_0 + a_1 v_0 \cos \omega_o t + a_2 v_0 \cos^2 \omega_o t + \ldots \tag{2.3}$$

[3]The following analysis has been performed using voltages, but the same are readily applicable to power amplifiers as well as they are proportional quantities.

Expanding the higher order terms of the cosine function leads to the gain component:

$$G_v = a_1 + \frac{3}{4} a_3 {v_0}^2. \tag{2.4}$$

The gain obtained is a sum of the linear gain and a third order term, which typically is of opposite in sign to that of a_1, which leads to the reduction of the output of the amplifier for large values of v_0. This effect is called as *Gain compression*. For an ideal amplifier, which would have no gain compression, the input-output relationship will be linear with a constant slope. For a practical amplifier, we would reach a voltage(power) limit, where the gain would start to droop. The input power at which the output power has decreased by 1dB from the idea linear characteristic is called the *1dB compression point (P1dB)*. P1dB can be stated in terms of both input and output powers, which datasheets provide the larger of the two values, which is the output power P1dB.

This can be converted directly to P1dB at input as $P1dBO - G + 1$.

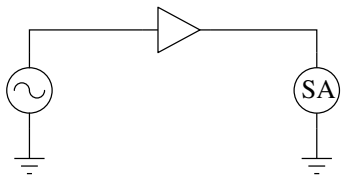

Figure 2.4: Test setup for measuring gain and P1dB

Usually, when a single tone is injected into the amplifier, the output may consist of harmonics of the input frequency (ω_o) at $n\omega_o$, where $n = 1, 2, 3, \ldots$. These harmonics usually fall outside the band of interest and can be filtered out subsequently. But when dealing with a wide band of signals, there may be strong tones (RFI in our case) at very closely spaced frequencies. The effect of such a scenario can be studied by setting $v_i = v_o(\cos \omega_1 t + \cos \omega_2 t)$. Substituting this into Equation 2.12 leads to:

$$\mathrm{v}_o = a_0 + a_1 v_o(\cos \omega_1 t + \cos \omega_2 t) + \frac{1}{2}(a_2 {v_o}^2((1 + \cos 2\omega_1 t) + (1 + \cos 2\omega_2 t))) + a_2 {v_o}^2(\cos \omega_1 - \omega_2 t + \cos \omega_1 + \omega_2 t) +$$

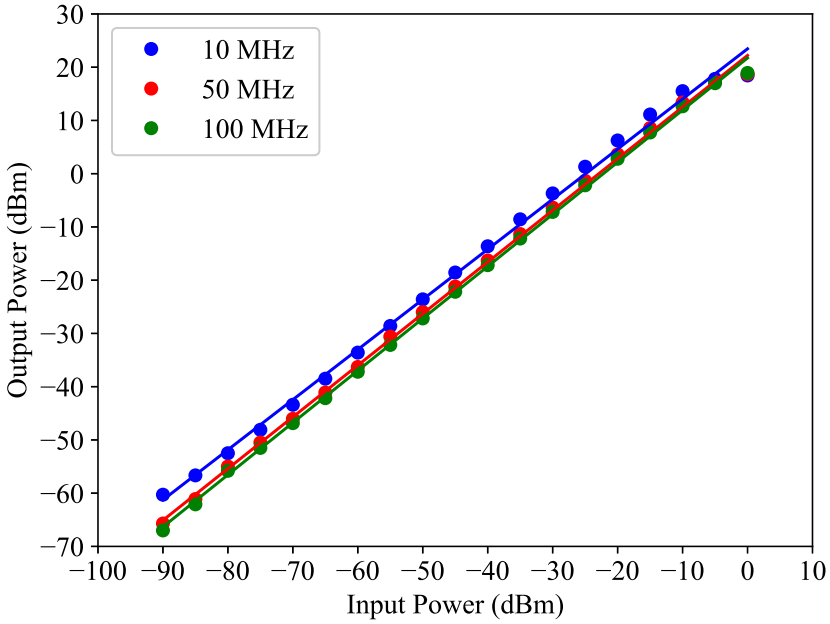

Figure 2.5: Power at 1dB gain compression point

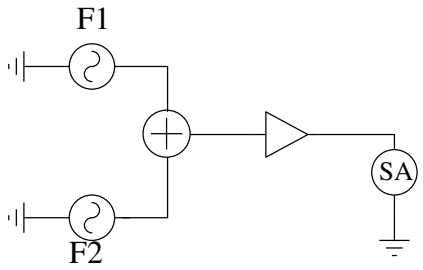

Figure 2.6: Scheme to measure the intermodulation distortion in amplifiers.

$a_3{v_o}^3(\frac{3}{4}\cos\omega_1 t + \frac{1}{4}\cos\omega_1 t) + a_3{v_o}^3(\frac{3}{4}\cos\omega_2 t + \frac{1}{4}\cos\omega_2 t) +$
$a_3{v_o}^3(\frac{3}{2}\cos\omega_2 t + \frac{3}{4}\cos(2\omega_1 - \omega_2)t + \frac{3}{4}\cos(2\omega_1 + \omega_2)t) + a_3{v_o}^3(\frac{3}{2}\cos\omega_1 t +$
$\frac{3}{4}\cos(2\omega_2 - \omega_1)t + \frac{3}{4}\cos(2\omega_2 + \omega_1)t) + ...(2.5)$

We see that the equation contains terms that have harmonics of $m\omega_1 + n\omega_2$ form, with $m, n = 0, \pm1, \pm2....$ The second order terms are characteristic of the output of a mixer, but are not desired from an amplifier. But these terms will fall sufficiently away from the pass band and can be filtered

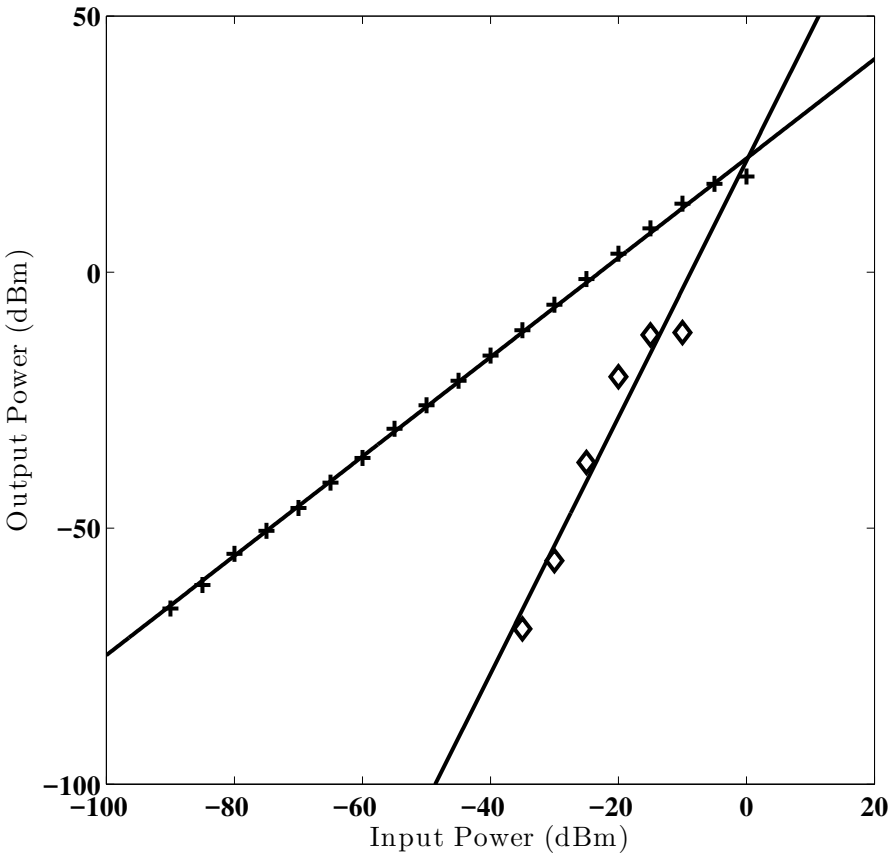

Figure 2.7: Third order intermodulation product of the amplifier.

easily. Of interest are the third order terms, $2\omega_1 - \omega_2$ and $2\omega_2 - \omega_1$. These two terms will be located sufficiently close to the signal, and thus cannot be filtered out directly. This effect is called *third order intermodulation distortion*. From the equation 2.2.1, it is seen that the $2\omega_{2/1} - \omega_{1/2}$ term are ≈ 3 times stronger than the $3\omega_{1/2}$ term.

As the input voltage (power) increases, the amplitude of the associated third order products increase as the cube of the input power. For small input powers, the third order effect is small, but increases rapidly for higher powers. This can be visualized by plotting the linear and third order output powers, respectively, to that of the input power. At high

powers, both the above products will exhibit compression, so the idealized responses can be obtained by extrapolating the respective curves linearly from the compression points. The point where the two curves intersect is the *third order intercept point (IP_3)*. This term, similar to P1dB can be expressed in terms of input or output.

The non-linear terms defined above are important in deciding the dynamic range of the receiver chain. Since in solar radio astronomy, we are typically limited by the noise from the source, there are times during high levels of solar activity, when the dynamic range of the signal can be as large as $\approx 30-40$ dB [Nelson et al. 1985]. Thus it is important to select amplifiers with sufficient linearity and dynamic to accommodate for these signals and also strong RFI at low frequencies.

Dynamic Range can be defined as the operating range within which a system has desirable characteristics. For an amplifier, at the lower end, it is limited by the sensitivity, and the P1dB at the higher end. This is the range within which an amplifier can operate in the linear range. This can be further extended to define a *Spur Free dynamic Range (SFDR)*, which is the frequency at which the magnitudes of the intermodulation products starts degrading the system response.

The linear dynamic range (LDR) and SFDR can be defined as follows:

$$LDR = OP1dB - S_{min} \tag{2.6}$$

and

$$SFDR = \frac{2}{3}(OIP3 - S_{min}) - SNR \tag{2.7}$$

2.2.2 Filter

Filters are used to select and process a specific frequency range. The signals received by the antenna are broad-band signals. To avoid complications in processing, the signal has to be restricted to selected chunks in frequency. The center frequency and width of these bands are decided by various factors such as the range in which the signals are strong, proximity to RFI, and bandwidth of the expected signal. For solar radio astronomy, the transient events that occur are very intense at low frequencies, typically

at frequencies $\leq 100\,\text{MHz}$. The whole of the former band is not usable as in most places the ionospheric cut-off is $\approx 15\,\text{MHz}$, and in the frequency range between $85-100\,\text{MHz}$ contains the FM band.

Based on these constraints, for the receiving systems presented in this thesis, band-pass filters, to obtain signal between $15-85\,\text{MHz}$, and band reject/notch filters to filter off signals in the FM Band was used.

Filters also can be characterized by S-parameters, but since filters are symmetric networks, the S_{11} and S_{22}, and the S_{21} and S_{12} are identical. Here, S_{11} and S_{21} indicate the filter attenuation in either direction. Since filter is a passive component, its noise figure is the same as its insertion loss. The response of filters used in various experiments are provided at the respective chapters.

2.2.3 Mixers

Mixers are non-linear devices used for translating the frequency of the received signal. The mixer has 2 inputs: a RF input, where the signal whose frequency is to be translated is connected and a Local Oscillator (LO) input. The mixer performs a multiplication operation and outputs the product signal at two frequencies. The output at an intermediate frequency (IF), is obtained. The working of a mixer can be mathematically represented as follows.

Let the RF signal be $A\sin\omega_{rf}t$, and the LO signal be $B\sin\omega_{lo}t$. Then the output is the product of the above two signals, which can be written as

$$C = 0.5 \times AB(\cos(\omega_{rf} - \omega_{lo}) - \cos(\omega_{rf} + \omega_{lo})) \tag{2.8}$$

We see that the output has components at two frequencies: $(\omega_{rf} \pm \omega_{lo})$. Depending on the signal needed at the output, either one can be filtered. When using mixers, it also becomes important to reject another frequency component called image frequency. Any frequency, other than the RF frequency, which would give the same IF when mixed with the LO signal is called the image frequency. This frequency is typically rejected when the signal is filtered before being fed to the mixer.

Mixers are also characterized by the same parameters required for the amplifier viz. dynamic range, P1dB and IP3. An additional term used is

called the conversion loss. It is the level by which the IF signal is below the RF signal. In order to overcome this, usually the LO level is maintained about 15-20 dB above the RF levels.

While the older systems at the Gauribidanur observatory used mixers in their super-heterodyne receivers, we do not use them in this thesis, as here one of our main goals was to sample the RF band directly.Thus, mixers were reviewed mostly for the sake of completeness.

2.2.4 Power Splitter/Combiners and Beam-formers

A single antenna usually lacks the sensitivity and resolution to study weak emission and fine structures on the object of interest. Thus to improve aforementioned quantities, it becomes necessary to combine multiple antennas. Power combiners and beam-formers are used for this.

Power combiners are passive devices used for, as the name suggests, combining RF signals from N paths and output the combined signal. A beamformer is a special case of a power combiner, where the signals are combined after introducing a delay or phase to enable phase coherent addition of signals [Mugundhan 2014].

For the two antenna case (see Figure 3.1 in Chapter 3), when the source is at the zenith, the net phase or delay between the signals is 0. Thus, at this position the signal can be combined directly without any delay or phase shift. But for a signal that is off-zenith, the signals for obtaining coherent addition, the signals from the individual elements have to be phased or delayed. This is done by delaying the signal from the antenna where the sky signal reaches first. For a signal frequency signal, delay and phase shifts are equal. But for a wide band signal, phase compensation alone introduces a "squint" in the beam. Squint is the phenomenon where the beams at different frequencies have their maxima at different directions. To avoid this, wideband signals are typically provided a delay compensation, rather than phase as delay is not frequency dependent.

For obtaining delay over a range of zenith angles, multiple stages of delay switching may be required. This is implemented is a network called a delay shifter. The typical architecture of the delay shifter is made of switches and delay lines. The control signals are chosen based on the delay required to selectively switch ON and OFF delay and no delay stages.

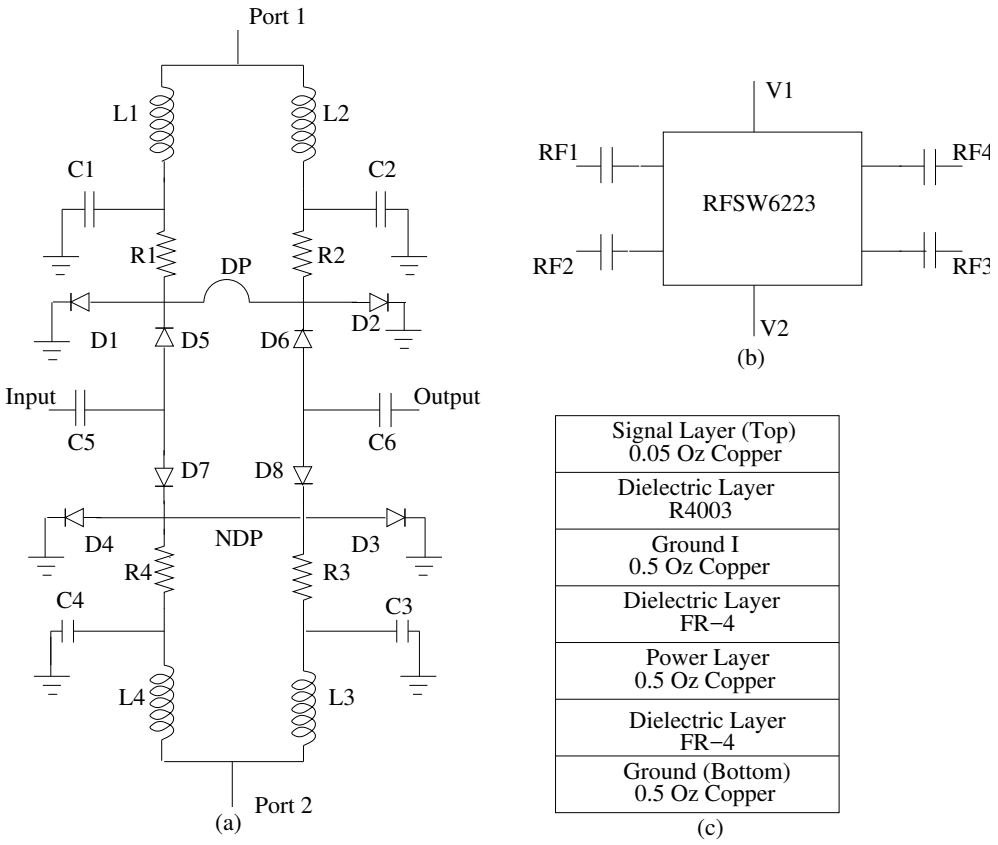

Figure 2.8: A diode based delay switcher is shown in (a). An equivalent network, implemented using a Miniature Microwave Integrated Circuit (MMIC) is shown in (b), along with the PCB stack-up required to obtain minimal return and insertion loss is shown in (c).

We see that the MMIC circuit's insertion and return loss are uniform through out the band. The restricted usage of discrete components in RF networks also decreases the possibility of it being affected by parasitics at high frequencies. Secondly, the development of this board showed that it is important to maintain controlled impedance overcome losses due to mismatch.

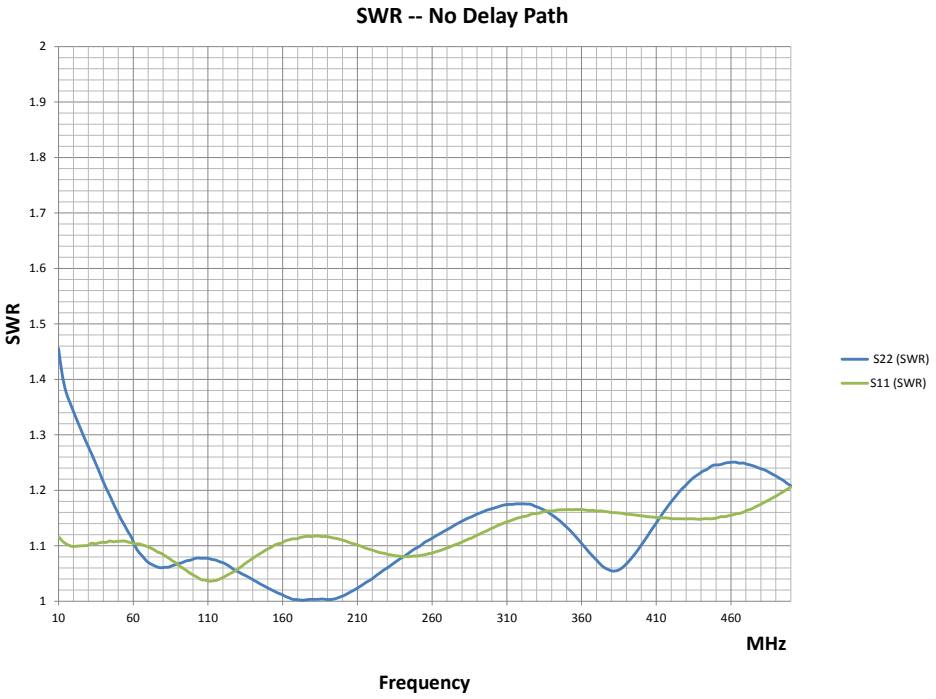

Figure 2.9: The SWR of a MMIC based, 4 stage delay shifter when the no-delay path is activated.

2.2.5 Friis Noise equation and System Noise Estimation

The noise added by the receiver chain to the input signal can be calculated by using the Friis noise equation (refer 2.9). It provides the total noise of the system as it is related to the gains and the noise figures of various stages.

$$F_{total} = F_1 + \frac{F_2 - 1}{G_1} + \frac{F_3 - 1}{G_1 G_2} + \frac{F_4 - 1}{G_1 G_2 G_3} + \ldots \tag{2.9}$$

A typical radio telescope system like the Gauribidanur Low Frequency Solar Spectrograph (GLOSS) would contain LNAs, Filters, beamformers, coaxial cables. Refer to the Figure 1 of Chapter 4. The total noise figure of this system can be estimated by arranging the gains and noise figures of the components in the signal chain in a spreadsheet and estimate the total

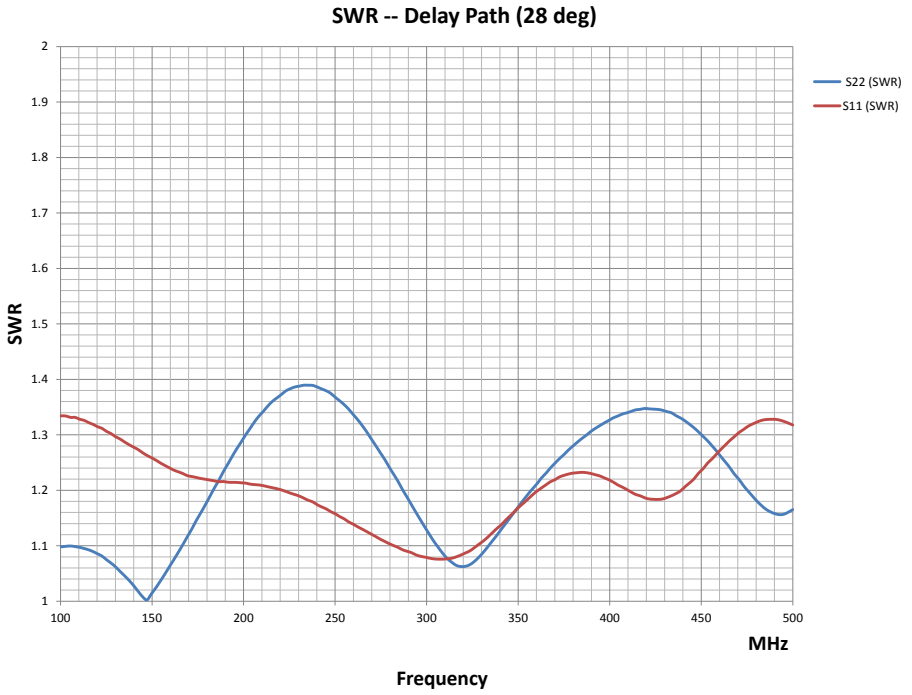

Figure 2.10: The SWR of a MMIC based, 4 stage delay shifter when the maximum delay path is activated.

output as given in the Friis equation.

2.3 Digital Systems

It becomes advantageous to convert the analog data to digital to store for processing it at a later point of time. The rapid pace at which electronics has advanced has miniaturized the components needed for this purpose such that even complicated digital systems can be easily realized with extremely robust and economical, with a small form-factor.

This section deals with various components of the digital systems used for the work presented in this thesis and provides a preliminary introduction to them.

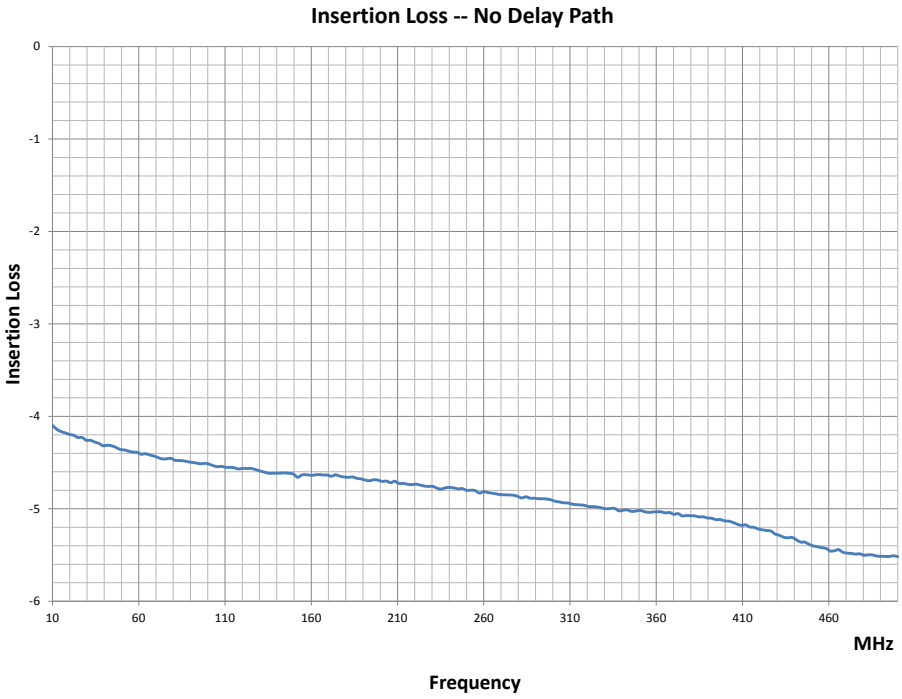

Figure 2.11: The Insertion loss of a MMIC based, 4 stage delay shifter when the maximum delay path is activated.

2.3.1 Analog to Digital Converter

The first element in any digital signal processing chain is the analog to digital converter. The device takes an analog signal as input and converts it to a numerical or digital version.

This is achieved by two steps: Sampling and Quantization. The quantized estimates of the signal will be encoded in a further step to a number, which can be used for processing [Gray 2003].

Sampling is the process in which information from the continuous analog signal is acquired at discrete time intervals, with the help of an external gating signal, called the sampling clock. Nyquist sampling theorem states that a signal has to be sampled atleast at twice its maximum frequency for faithful reproduction of all frequency components present in it.

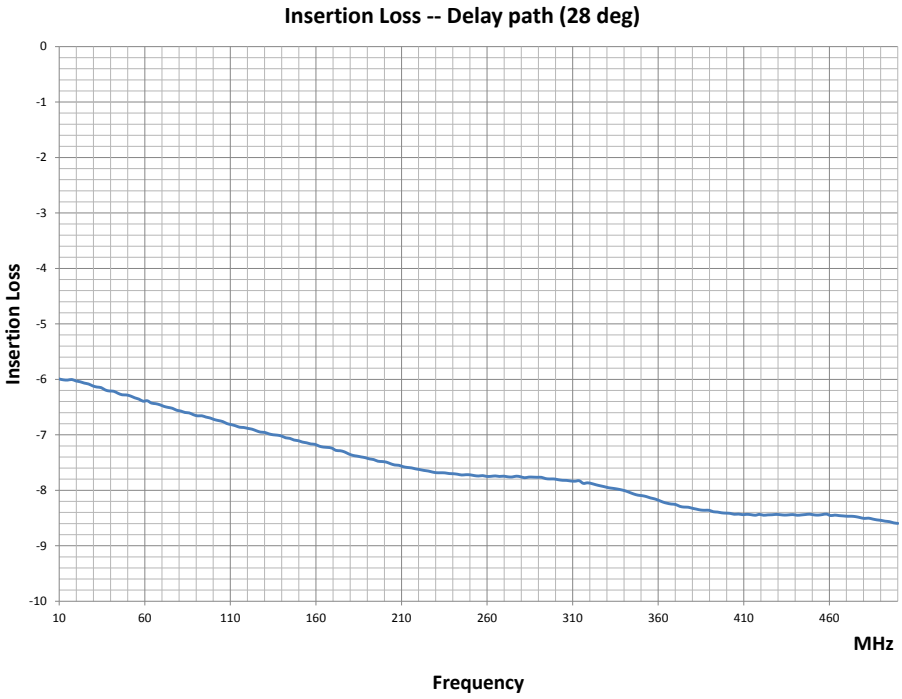

Figure 2.12: The Insertion loss of a MMIC based, 4 stage delay shifter when the maximum delay path is activated.

This gives rise to three scenarios: Over-sampling, Under-sampling and critical sampling. Critical sampling is when the signal is sampled exactly at the Nyquist frequency. Under-sampling and over-sampling mean the signal is sampled at a frequency below and above the Nyquist frequency.

One of the goals of work presented in this thesis was to explore the possibility of direct RF sampling for the digital backends to do away with the heterodyne receiver setup, currently used in the analog front ends of GRAPH and GRIP instruments. The maximum frequency at which these instruments operate are at $\approx$ 120 MHz, with an effective bandwidth of 100 MHz. So for our trial observations, ADCs capable to sampling at such high frequencies (typ $\approx$ 200 MHz) were selected.

There are different families of ADCs. These can be differentiated by their architecture [Kester 2005] . Pipelined architecture is usually used for

RF sampling ADCs to manage the high data throughput.

Sometimes, in multicore ADCs, [4] one can achieve twice or more bandwidth (based on the number of cores present) using the principle of interleaving. Interleaving is the process in which different cores are operated at clocks of different phases such that each core samples different instances in a single cycle. For example, in a 4 core ADC, with respect to the reference clock, the cores are phase shifted by 0°, 90°, 180°and 270°. This is equivalent to sampling the same signal at 4× Nyquist rate.

When ADCs breakdown a continuous signal to values at specific time instants, the conversion process introduces imperfections into the converted data stream. It is thus important to study and quantify various parameters of the ADC that help in characterization of these imperfections. There are two types of parameters: Static and Dynamic parameters, which are elaborated in the next two sections [Linnenbrink et al. 2001].

2.3.2 Static Parameters

These parameters define the response of the ADC to a DC or a slowly varying signal. These parameters are inherent to the ADC itself. These are:

1. Offset Error: The difference between the ideal and the actual transfer function of the ADC is the cause of this error. This is measured by feeding a known voltage and noting the deviation between the expected and the ideal code. This quantity is dependent on temperature. The ADCs used in this thesis provided tunability of the offset error using Serial Peripheral Interface (SPI), which was used to correct for this offset error.

2. Gain Error: This is the difference between the actual and the ideal voltage that provides the full scale voltage. This error is easily influenced by the offset error. So, this test typically has to be done only after correcting for the offset error. The variation of gain error with frequency is called the gain drift.

[4] A ADC chip with many converter cores

3. Integral and Differential Non-linearity: Ideally, the difference between 2 codes in an ADC is 1 LSB. The error between the actual and ideal difference is Differential Non-linearity. This, for the ADCs used in this thesis are ≤ 0.05 LSB. Integral non-linearity (INL) of a code is the cumulative sum of all codes up-to the code for which the INL is required.

   All these errors cumulatively contribute to the Total Unadjusted Error which is the rms sum of all the aforementioned errors.

2.3.3 Dynamic Parameters

An ADC, that is typically used in RF applications will encounter high frequency signals more often. So, more than static errors, it becomes important to understand the response of the ADC to such signals. The dynamic parameters of the ADC are:

1. Signal to Noise and Distortion Ratio (SINAD)
2. Total harmonic distortion (THD)
3. Spur Free Dynamic Range (SFDR)

All these error affect another figure of merit of an ADC, called Effective Number Of Bits (ENOB). ENOB is a more realistic estimate of the resolution of an ADC, and how it is affected by dynamic parameters. ENOB questions the performance of the ADC as follows: What would be the *quantization* of the ADC that gives a particular set of dynamic parameters, had the ADC been ideal?

ENOB and SINAD are related as follows:

$$ENOB = \frac{SINAD - 1.76}{6.02} \tag{2.10}$$

2.3.3.1 Methods

A simple technique to measure the ENOB is the sine wave fitting test. Sine waves at different frequencies and amplitudes are fed to the ADC and is

sampled "coherently", which means that there is always an integral number of cycles in the sampled data set. While coherent sampling may not be a strict requirement for ENOB measurement, it is important for SINAD, SFDR and THD measurements, which are inferred from the spectral characteristics. This is because a non integer number of cycles will introduce an uncertainty in the number of frequency components present in the signal and will introduce side lobes. While these lobes can be reduced using windowing functions, it is more convenient to choose the input signal frequency such that this condition is maintained.

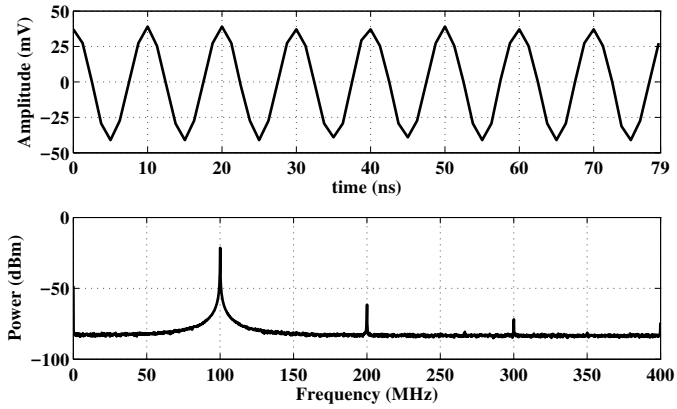

Figure 2.13: Spectrum of an incoherently sampled sine-wave

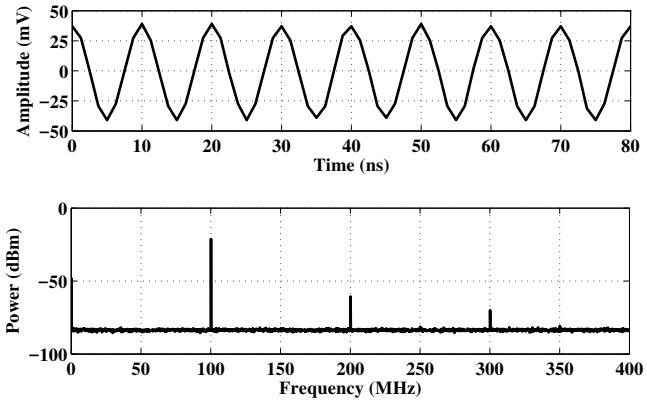

Figure 2.14: Same as previous figure, but for coherent sampling.

The sine wave data thus acquired is passed through a routine that fits a sine wave of the form:

$$Y = A\cos(\omega t) + B\sin(\omega t) + C \tag{2.11}$$

The rms error of the least square fit is obtained and is used to find the ENOB as:

$$ENOB = N - \log_2 \frac{E_{rms}}{V_q/12}. \tag{2.12}$$

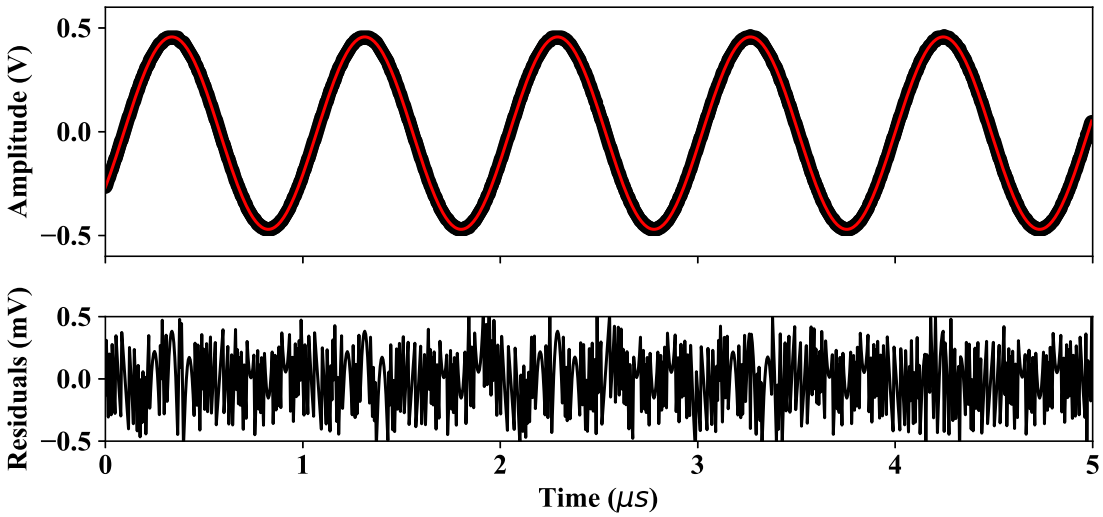

Figure 2.15: Sine Wave curve fit to acquired ADC data, and its residuals.

Figure 2.16 shows the sine wave fit and the obtained residuals for a signal of amplitude ≈ 500 mV and a frequency of 1 MHz. We see from the bottom panel of Figure 2.2 that at low amplitudes, ENOB goes as low as 3 bits. This is because, at those levels, only few levels of the ADC code is occupied. Similarly, on the high frequency side, we see that after ≈ 1 V, the ENOB drops rapidly. This is because the ADC enters non-linear regime, once the input voltage exceeds its full scale voltage, thus resulting in a decrease in the ENOB. The input signals levels to the ADC is decided based on these results. Typically in solar observations interested

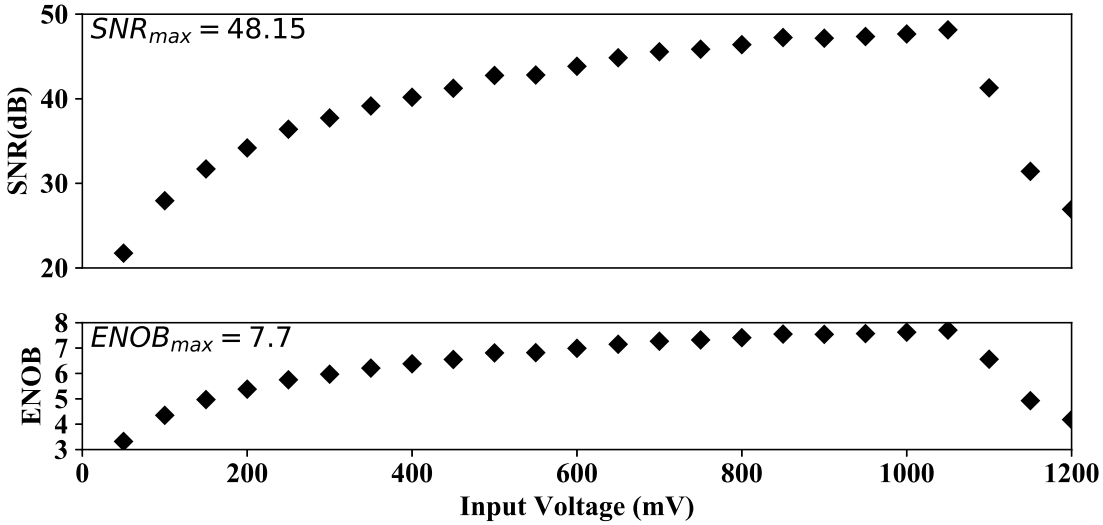

Figure 2.16: The variation of ENOB and SNR of the ADC with input signal amplitude.

in studying bursts, it is useful to have ≈ 3 bits for the background, and 5 bits for times of high transient activity, such that dynamic range is not lost.

SFDR of the signal is the difference between the signal and its worst spurious signal, regardless of where it lies on the frequency spectrum. This signal can also be the harmonic of the original signal. This characteristic is important in radio astronomy as this would represent the smallest signal that can be detected in the presence of strong interferers. This measurement is carried out by measuring the power spectrum of the signal at various frequencies and finding the difference between the signal peak and the spurious peak. The signals that were captured for the ENOB test was used for this measurement also. This signal was fast Fourier transformed and the resultant spectrum was plotted.

The figure is normalized such that the peak of the carrier signal is a 0 dB. The SFDR in this case is found to be ≈ 53.5 dBc [5].

Total harmonic distortion (THD) is measured by feeding a signal and finding the ratio of the signal peak to that of all harmonics that are present

[5]Decibels relative to the peak carrier signal

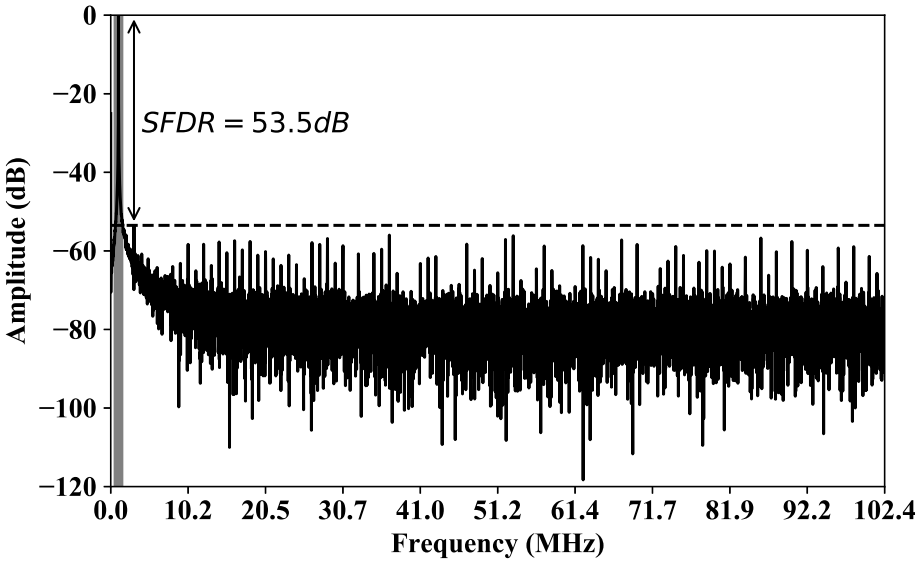

Figure 2.17: Measurment of the Spur Free Dynamic Range.

within the band. For this also, the Fourier technique is used. Usually, the first 5 harmonics are only taken into account for this measurement as only they are dominant.

2.3.4 Field Programmable Gate Arrays

In this thesis, all the digital backends that were developed used Field Programmable Gate Arrays (FPGA, see Figure 2.19). These are a category of digital devices, which provides us with the flexibility to reconfigure the hardware in particular ways that suit us.

At their lowest level, FPGAs are nothing but a collection of switches. These switches are grouped into blocks of configurable logic, resources for clocking like Phase and Delay Locked Loops (PLL and DLLs), Digital Signal Processing (DSP) resources, and Transceivers for enabling high speed communications. Architecture of a generic FPGA device is shown in the Figure below.

There is a specific design flow to design with any FPGA, which is enumerated below:

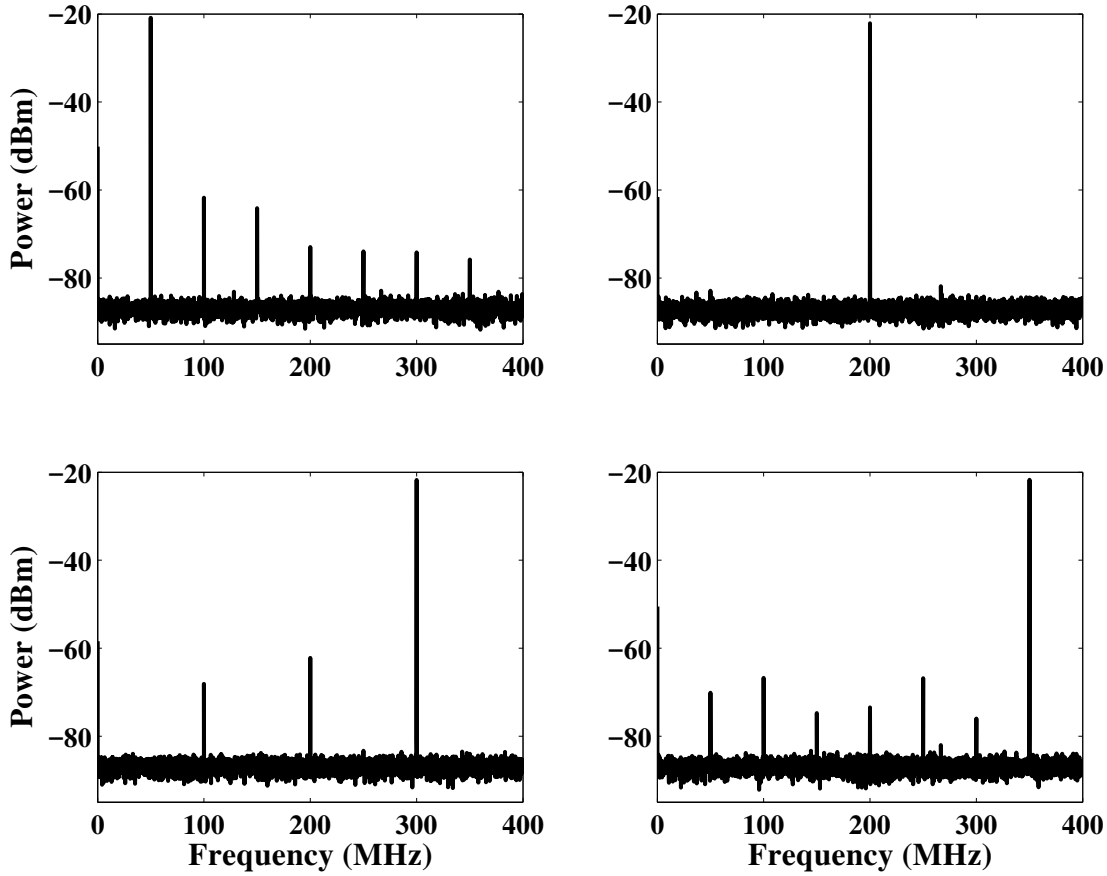

Figure 2.18: Variation of SFDR at different frequencies.

1. Design Entry: In this step, the design of the system we are interested in is created in the form of Hardware Description Language (HDL) programs (using Verilog or VHDL[6]). It also is entered sometimes using C/C++, or graphical interface blocks, like in MATLAB-Simulink or LabView.

2. Design Synthesis: In this step, the code or high level design from the previous step is converted into a netlist, describing the connections

[6]VHDL is the abbreviation of Very high speed integrated circuit Hardware Description Language

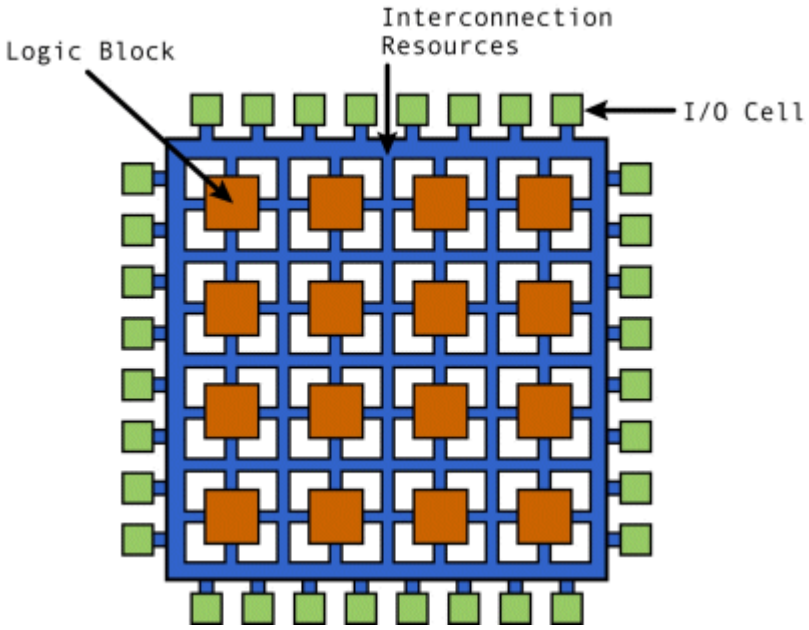

Figure 2.19: Architecture of a generic FPGA device.

between the various elements in the design.

3. Place and Route: This process can be broken up into three steps. In the first step, the synthesized netlist is packed into various logic resources present in the FPGA. Modules that are connected directly are packed to resources that are present close by. In the Placement step, the packaged design is placed at the respective location on the FPGA, and in the final Routing step, the connections between the placed resources are completed using some design constraints specified by the user.

4. Programming the FPGA: The routed design is then converted to a bit-stream that can be programmed into the FPGA. The configuration of the FPGA using bit files is done using Joint Test Access Group (JTAG) ports present on the FPGA or using a Serial or Parallel Interface.

In this project two FPGAs from the Xilinx Virtex 5 family were used (refer to Table 2.1). These FPGAs are Static Random Access Memory (SRAM) based. So they cannot retain the configuration when powered-off. For

Table 2.1: The resources present in the two FPGAs used in this thesis.

Resource	XCV5LX110T	XCV5SX95T
Logic Elements	110592	94208
DSP Slices	64	640
Block RAM	4608 Kb	8784 Kb
Transceivers	16	16
Platform	XUPV5	CASPER ROACH-1

re-configuring the FPGA during power-on, an external non-volatile memory was used. This non-volatile memory is configured with the FPGA bitstream, and on power-on, is transferred to the FPGA using SPI.

2.4 Communication systems

The systems developed in this thesis performed the processing of the digitized data onboard the FPGA. For acquiring the processed data, communication interfaces are required. The choice of the communication network used depends on the data rate, ease of development and readily available interfaces to data aquisition servers.

The three systems used in this thesis for high speed data acquisition are Gigabit Ethernet (Gbe)[7] and Peripheral Component Interface express (PCIe)[8] and 10 Gigabit Etherent (10Gbe) [Cunningham 2001].

Gbe is a networking protocol which is used for transferring data at gigabit rates. The communication is packet based. The data that is to be transferred is encapsulated as ethernet packets. Each packet contains a header field which is defined as:

1. Source and Destination Media Access Controller (MAC) Addresses
2. Type/Length field, elaborating the version of internet protocol and the size of the packet to be sent
3. The time for which the data has to be retained in the network or Time To Live (TTL), and the datagram protocol. This was chosen to be

[7]https://study-ccna.com/ieee-ethernet-standards/
[8]https://pcisig.com/specifications/pciexpress/

User Datagram Protocol (UDP) in our case to achieve high streaming speeds.

4. If UDP is chosen, the ports between the communication takes place is to be included in the header. If the user chooses to have some header for identification or troubleshooting, then it can be included after this as part of the data bytes.

Normal ethernet packets are 1500 Bytes in length including the headers. There is a special class of packets called Jumbo Frames which have a capacity of upto 9000 Bytes.

10Gbe packets have a similar header structure, but our data acquisition systems used Jumbo Frames for 10Gbe communications.

The physical layer is the medium through which the communication takes place. This usually is a pair of copper twisted pair cables (RJ45) for Gbe. The 8 bit data that is to be transmitted is encoded to 10 bits, and is transmitted as Low Voltage Differential Signals (LVDS). The encoding takes place in such a way that over a long time, equal number of ones and zeros are maintained in the stream. This is for the receiver to decode and recover the clock from the actual data stream itself, rather than transmitting the clock also in a separate differential pair. This stream of data is then decoded in the receiver end and is passed on to the higher layers. Ethernet data can also be transmitted using optical media, where the data is converted into a stream of optical pulses and transmitted. At the receiver end, these pulses are detected and converted back to data for the user. The above process applies for 10 Gbe also, but the data is encoded as 64-66 bit, and two twisted pairs are used for transmission and two for reception. The physical layer cable used for our systems was a CX4 cable.

PCIe is an bus interface specification, which defines how various devices connect to the processor on the mother-board of a computer. It was a replacement to the older, parallel, Peripheral Component Interconnect (PCI). While the PCI can transfer a maximum of 33 MB/s, PCIe can transmit upto 250 MB/s of raw data per lane. Similar to ethernet, the communication between the transmitter and the receiver is handled as packets. The packetization and de-packetization is handled by the transaction layer. In the physical layer, the communication happens through lanes. Based

on lanes, there are 4 categories of PCIe: x1, x4, x8 and x16. The maximum theoretical speed possible is 4 GB/s for Generation 1 PCIe. For the latest 5th Generation, it is 63 GB/s.

PCIe communication in this thesis was implemented using an core called Xillybus[9]. This core wraps all the low level functions of PCIe and interfaces at the top level to a First In First Out (FIFO) buffer on the FPGA side. On the host side, this FIFO is seen as a device file. A shared memory FIFO is implemented on the host side to handle high speed data communications, without any data loss. The block diagram of Xillybus connections are shown in the figure.

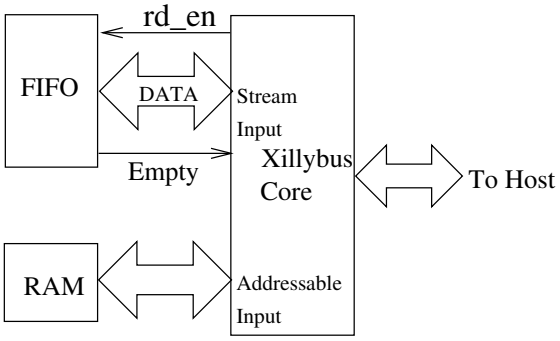

Figure 2.20: Block diagram of Xillybus interface connecting a FIFO in an FPGA to a host

These high speed interfaces are characterized to test for data slips after integration into the FPGA. A data generator, typically a counter, is used to generate data at high speed, and is fed to a FIFO. The high speed data is encapsulated into a packet with serial number. On the data acquisition system, these packets are recorded, and checked for any slips in data. This is used to test the reliability of a high speed communication system.

2.5 Conclusion

In this chapter, various analog and digital hardware components used in this thesis were described. Characterization of these components and

[9]www.xillybus.com

understanding their reliability is important to know the limits of the designed system, as they are mostly deployed in the field. The algorithms used for the firmware and the data processing is described in the respective chapters.

References

Cunningham, D. G. (2001). The status of the 10-gigabit ethernet standard. In *Optical Communication, 2001. ECOC'01. 27th European Conference on*, volume 3, pages 364–367. IEEE.

Gray, N. (2003). Abcs of adcs. *National Semiconductor Corporation, Aug*, 4.

Kester, W. (2005). Which adc architecture is right for your application. In *EDA Tech Forum*, volume 2, pages 22–25.

Kirichenko, D. E., Filippov, T. V., and Gupta, D. (2009). Microwave receivers with direct digitization. In *Microwave Symposium Digest, 2009. MTT'09. IEEE MTT-S International*, pages 1449–1452. IEEE.

Kraus, J. D. (1966). *Radio astronomy*.

Linnenbrink, T. E., Tilden, S. J., and Miller, M. T. (2001). Adc testing with ieee std 1241-2000. In *Instrumentation and Measurement Technology Conference, 2001. IMTC 2001. Proceedings of the 18th IEEE*, volume 3, pages 1986–1991. IEEE.

Mugundhan, V. (2014). *Beam-former for single beam, total power mode observations with Gauribidanur Radioheliograph*. PhD thesis, Indian Institute of Astrophysics.

Nelson, G. J., Sheridan, K. V., and Suzuki, S. (1985). *Measurements of solar flux density and polarization*, pages 113–154.

Pozar, D. M. (2009). *Microwave engineering*. John Wiley & Sons.

Proakis, J. G. and Manolakis, D. G. (1996). Digital signal processing 3 rd edition.

Thompson, A. R., Moran, J. M., and Swenson, G. W. (2001). *Interferometry and Synthesis in Radio Astronomy; 2nd ed.* Wiley-VCH, Weinheim.

Chapter 3

Long Baseline Interferometry of the Solar Corona

This Chapter is based on:

1. *Mugundhan V., Ramesh R., et al., 2016, The Astrophysical Journal, 831, 154*

2. *Mugundhan V., Ramesh R., et al., 2018, The Astrophysical Journal Letters, 855, L8*

3.1 Introduction

The size of the smallest structure observable at radio wavelengths in the solar corona is one of the open questions in solar radio astronomy. White-light observations of the solar corona during eclipses and with coronagraphs reveal structures of characteristic dimensions ≈10″ in the heliocentric distance (r) range of $\approx 1.1-2.0R_{\odot}$ from where the low-frequency (100 – 30 MHz) radio radiation typically originates. The size of the smallest observable angular structure in the solar corona is believed to be limited by the scattering due to density turbulence there. Ray-tracing calculations and observations in the past have indicated that scattering results in the angular broadening and under-estimated brightness temperatures (T_b) of compact sources in the aforementioned distance range [Erickson 1964, Aubier et al. 1971, Bastian 1994, Sastry 1994, Ramesh 2000, Ramesh and

Ebenezer 2001, Ramesh et al. 2006]. In view of this, there have been suggestions that interferometers with angular resolution better than 3′ may not be needed for solar imaging[Bastian 2004].

It is to be noted that previous observations were carried out with instruments of limited angular resolution (>2′; Wild [1967], Labrum [1972], Kundu et al. [1983], Kerdraon and Delouis [1997], Ramesh et al. [1998]). Conventional synthesis imaging instruments observing the sun are also dynamic range limited, because the flux of the sun during times of activity is atleast 2-4 orders of magnitude higher than that of the quiet corona. This makes observations of fine structures associated with weak energy releases relatively difficult.

Nonetheless, noise storm sources of size $\sim 35''$ at 327 MHz have been detected previously by [Lang and Willson 1987] using the Very Large Array (VLA), [Mercier et al. 2006] and [Mercier et al. 2015] using the Giant Meterwave Radio Telescope (GMRT). Eclipse observations conducted at Gauribidanur has confirmed the existence of sources smaller than the diffraction limit of such a set-up ($\approx 15''$; Kathiravan et al. [2011], Ramesh et al. [2012]). Recent theoretical studies on coronal scattering with spherical wave solutions confirm the above and predicts the existence of sources $< 10''$ [Subramanian and Cairns 2011].

This calls for radio observations in the above frequency range with high angular resolution, since there are unique advantages like:

1. Simultaneous observations of both the corona overlying the solar disk as well as off the solar limb with the same instrument (see for example Kathiravan et al. [2002])

2. Observations with good contrast even at short data integration times ($\approx$100 ms)

3. Sensitivity to density enhancements since radio brightness is $\propto n_e^2$, where n_e is the coronal electron density

4. Radio bursts associated with the solar transients are intrinsically more intense at low frequencies, since the associated emission processes (plasma or gyrosynchrotron mechanisms) are nonthermal in nature

5. Simpler measurements of the coronal magnetic field through circular polarization observations (see for example Sasikumar Raja et al. [2014])

Taking into consideration the minimal radio frequency interference (RFI) in Gauribidanur [Monstein et al. 2007, Kishore et al. 2015, Hariharan et al. 2016], the "stable" ionosphere during midday [Kassim et al. 2007], the proximity of the declination of the Sun to the latitude of Gauribidanur (≈14° N) for a major part of the year, because of which the zenith angle-dependent ionospheric errors are expected to be smaller [Jacobson et al. 1991, Mercier and Chambe 2009], predicted small coronal radio source sizes [Subramanian and Cairns 2011], and the advancements in the field of digital signal processing, a pilot study in the Gauribidanur observatory [Ramesh et al. 2011] with a simple radio interferometer that provides an angular resolution of $\approx 1'$ could was carried out. At a later point, the baseline was extended to ≈ 200 km to search for sources as small as ≈ 10″.

This study is important as future radio arrays such as the LOw Frequency ARray (LOFAR; Van Haarlem et al. [2013]), Murchison Widefield Array (MWA; Tingay et al. [2013]), Long Wavelength Array (LWA; Ellingson et al. [2009]) and the Square Kilometer Array (SKA; Dewdney et al. [2009]) are expected to have long-baselines for facilitating high resolution imaging. From this viewpoint, this experiment can be considered to be a "pilot" study for long-baseline solar radio observations.

This chapter introduces essential radio interferometry, describes the first round of 8 km Long Baseline Interferometer (LBI) experiment, the instrumentation and its characterization, and results from the above campaign. Then, the Gauribidanur-Gadanki 200 km LBI experiment is described along with the results obtained during this campaign. The chapter concludes after a short discussion of the implications of the results obtained and future scope for such LBI solar observations.

3.2 Radio Interferometry

The resolution of an astronomical telescope depends on two parameters: the size of the aperture and the wavelength of operation. During the early days of radio astronomy, observations were carried out mostly using large

dishes (e.g. Green Bank Telescope, Jodrell Bank, Effelsburg Telescope, Arecibo etc.). In the quest for higher resolution per aperture, the operational frequency was also gradually increased to higher frequencies ($\approx$ 100s of MHz to a few GHz), departing from the low frequency (<100 MHz) where the initial radio astronomical discoveries were made. But there came a point, where the increasing the size of the telescope was not practically possible. Australian and English scientists at CSIRO and Cambridge first attempted to synthesize a telescope using two discrete antenna elements separated by a distance, which provided the same resolution as a dish of size equal to the separation between, but at a decreased sensitivity. Sensitivity could be improved upon later by integrating over a larger bandwidth or time. Martin Ryle realized that this arrangement of antennas would indeed synthesize a complete, "filled" aperture as the earth rotates. Radio telescope arrays like the Very Large Array (VLA), Giant Meter-wave Radio Telescope (GMRT) and Gauribidanur RAdio HeliograPH (GRAPH) etc. built up on this technique of aperture "synthesis". But the most simplest element of any aperture synthesis radio telescope is the *two element interferometer*, described in the next section.

3.2.1 Two Element Interferometer

As the name suggests, two element interferometer is made up of a pair of receiving elements. At high frequencies, these elements are usually single dishes, while they can be as simple as a dipole at low frequencies. Since the thesis concentrates on low frequencies, we will consider the only the latter, but the principle remains the same irrespective of the frequency of observation.

The two antenna elements are spaced apart by a distance, d, called *baseline*. The baseline decides the spatial resolution of the two element interferometer. The relation between the wavelength of operation λ, the baseline and the resolution θ is:

$$\theta \approx \frac{\lambda}{d}. \tag{3.1}$$

The above equation's denominator will be $2d$, when fields are at the edge of the aperture [Kraus 1966].

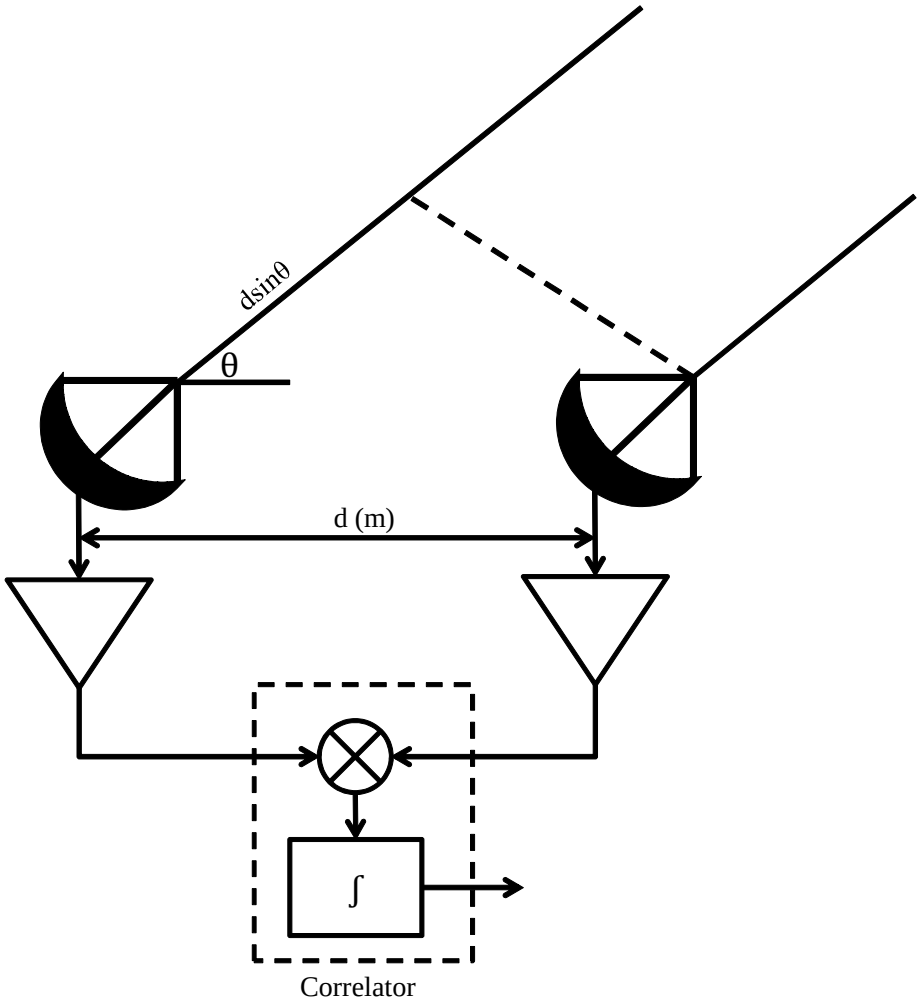

Figure 3.1: A simple two element interferometer.

Figure 3.1 shows the arrangement of a two element interferometer. The inteferometer baseline is d, and plane waves are incident on the antenna. The angle that the baseline makes with the source is θ. When the source is at zenith, there is no phase difference between the signals received by the individual antennas. Thus, the response of the interferometer (r) is maximum when the source is at the zenith. When the source is off-zenith, due to the fact that the radiation from the source has to travel a longer path

to reach the antenna on the farside, a *geometric phase* ϕ_g gets added to the signal received by the former. By using basic trigonometric principles, ϕ_g can be shown to be:

$$\phi_g = \frac{2\pi}{\lambda} d \sin\theta \tag{3.2}$$

So, the electric fields received by the antennas will be

$$E_1 = E_0 \sin(\omega t) \tag{3.3}$$

and

$$E_2 = E_0 \sin(\omega t + \phi_g). \tag{3.4}$$

The fields will be converted to a voltage signal, but since both are proportional quantities, we can retain the electric field formalism itself for our analysis. The *correlator* block is where the phase coherence of the signals received from these two antennas will be estimated. The correlator performs an operation of multiplication, followed by integration. Correlation operation can be defined mathematically as:

$$r(t) = \int_{t_1}^{t_2} x(t)^* y(t+\tau) dt, \tag{3.5}$$

where r is the amplitude of correlation, and τ is the lag. If we set $\tau = 0$, like in case of a *zero-lag* correlator, then the correlation between the electric fields can be written as:

$$r_{E1E2} = \int_{t_1}^{t_2} E_0^2 (\sin(\omega t))(\sin(\omega t + \phi_g)) dt \tag{3.6}$$

where the time interval over the limits of the integration is called the *integration time*. Since the nature of the sky signal is gaussian, larger integration time results in a better signal to noise ratio. The above equation, when evaluated, becomes,

$$r_{E1E2} = \cos\phi_g. \tag{3.7}$$

3.2.2 Bandwidth and Integration time Effects

In the previous section, we derived the two element interferometer response assuming the incident radiation is monochromatic in nature. How-

ever, when actual observations are carried out, the signal is always detected with some finite bandwidth. Also, the sensitivity, or the minimum detectable flux, of an interferometer is given by[Kraus 1966]:

$$\delta S_{min} = \frac{2k_B T_{sys}}{A_e \sqrt{\beta \tau}}, \tag{3.8}$$

where A_e is the effective collecting area of the interferometer, which is the geometric mean of the effective areas of the individual antennas [Christiansen and Högbom 1987]; β and τ are the bandwidth and integration time, respectively. It is seen from the above equation that it is also necessary to observe over a broad bandwidth to improve the sensitivity. But observing over a large bandwidth has its own disadvantages as well. *Bandwidth decorrelation* is one such disadvantage. It arises due to the fact that over a large observing bandwidth, for observations away from the meridian, radiation at different frequencies, which have different geometric phases, add incoherently. When the signal bandwidth is added as limits of integration, $f_c - \beta/2$ to $f_c + \beta/2$, where f_c is the centre frequency of observation,to Equation 3.6, the result is Equation 3.7 multiplied by a *sinc* function of the following form:

$$d_r = \frac{\sin \pi \beta \tau_g}{\pi \beta \tau_g}, \tag{3.9}$$

where d_r is the bandwidth decorrelation. d_r is dependent on the baseline length due to the presence of τ_g in the equation. d_r is 1 for sources at the zenith. A source that is at zenith is at 0° with respect to the phase center of the interferometer. For longer baselines, d_r becomes narrower, in effect, reducing the observation time.

The interferometer response is modulated by the above decorrelation sinc functions during observations. Figure 3.3 shows this phenomena.

This effect can be avoided by splitting the observation bandwidth into discrete frequency channels during correlation. The optimal bandwidth can be obtained by holding the baseline constant and varying the bandwidth. This would result in a curve like the one shown in Figure 3.4.

This effect is offset in interferometers using dish antennas by tracking the source continuously, such that the source is always at the phase center of the interferometer. For dipole arrays, this effect can be compensated in

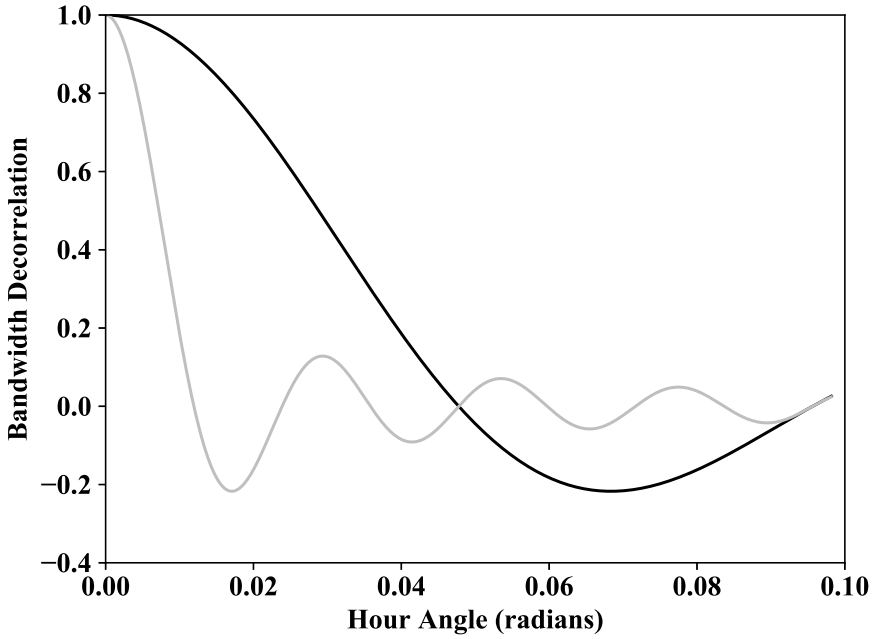

Figure 3.2: Bandwidth decorrelation as a function of hour angle. The solid black and grey lines are for 2 km and 8 km baselines, respectively. Note that the null arrives faster for the 8 km baseline curve.

a similar way, by tracking the source by the means of beamforming (see Section 2.2.4 in Chapter 2).

Time averaging also causes some decorrelation. Since the response of the interferometer varies at the fringe frequency, the integration time must be always below the fringe period, which is the time taken for a full fringe cycle. When the integration time is equal to the fringe period, the average value of the fringe function in Equation 3.7 becomes zero. This can be overcome by carrying out a fringe stopping operation by actively compensating for the geometric delay during the time of observation. This requirement becomes even more stringent in the case of VLBI observations, where other than the geometric delay, delay due to ionosphere, atmosphere, doppler delays due to precession, nutation, and wobble of the earth comes into play. So, for this, extensive modelling of the delay is carried out by using data from precision astrometry, measurements of Total Electron Content

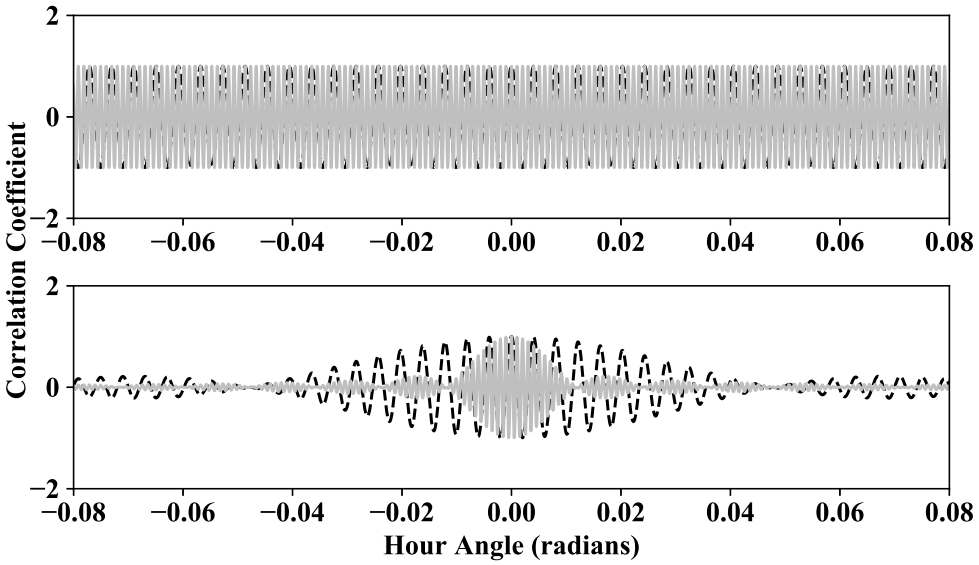

Figure 3.3: Effect of bandwidth decorrelation on fringes as a function of hour angle. The top panel shows the fringes for a 2 km and an 8 km baseline, when the radiation incident on the interferometer is monochromatic. The bottom panel shows the effect of integrating over a bandwidth of 1 MHz. In both the panels, the dashed black line represents the response of a 2 km baseline, while the solid grey line is the response of an 8 km baseline.

from dual frequency Global Positioning System (GPS) *etc.*.

3.2.3 Long Baseline Interferometry

Due to the long wavelengths involved, achieving high resolution in radio astronomy requires large apertures. For instance, in our case, for achieving an angular resolution of 1′ at 37 MHz, an equivalent aperture of 8 km is required. But it is not always physically feasible to achieve aperture of such scales. Thus, techniques were conceived, where in contrast to the conventional *connected element interferometers*, the elements were independent of each other. *Independent* here implies that there no common LO or sampling clock distributed between them and thus, they were not directly synchronized. Indirectly synchronizing these independent systems required very high level of precision, which was enabled by the use of atomic clocks.

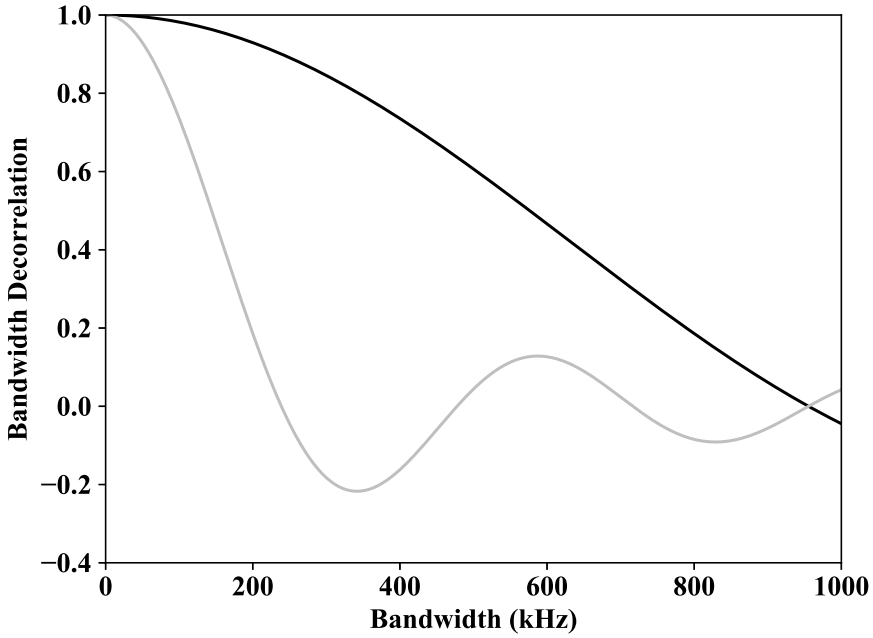

Figure 3.4: Effect of decorrelation with integration bandwidth. Note that for an 8 km bandwidth, an integration of 50 kHz results in a $d_r \approx 0.9$. Thus, for our subsequent observations on an 8 km baseline, the above bandwidth was used to avoid decorrelation.

Each system had its own atomic clock, which were initially synchronized to a common reference. These atomic clocks provided the reference for individual stations, where the LO and the samplers derived their respective signals from the former. This second order synchronized data was recorded and stored in disks for later analysis. The analysis is usually performed in a correlator facility, where data-disks from all the antennas involved in the observation is transported. The data is then offset for delay compensation, and then finally correlated to obtain the visibilities, which are used to obtain high resolution images [Booth 1991, Napier 1994]. Figure 3.5 shows a typical schematic of a Long Baseline Interferometer system.

In the earliest of these systems, the data rates were limited to a few kbps. With the advancements in electronics, the difference between connected and disconnected element interferometry is diminishing, as the European

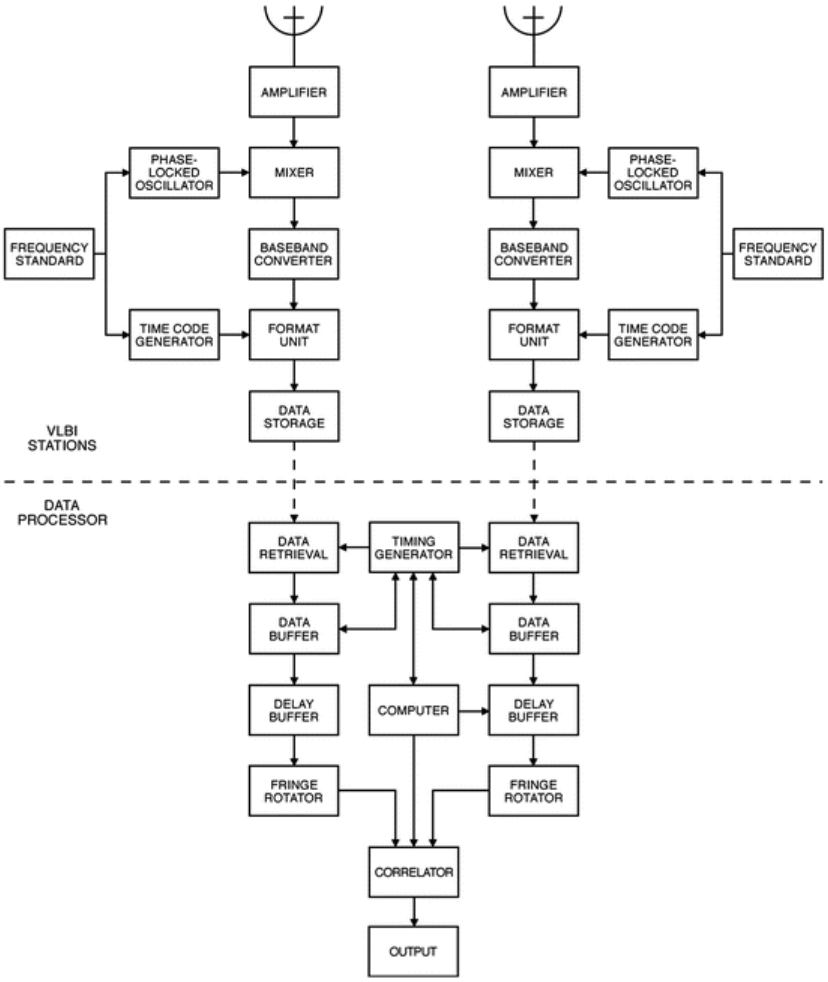

Figure 3.5: A typical Long Baseline Interferometer System. Figure adopted from Thompson et al. [2017], Chapter 9.

VLBI Network (EVN) has demonstrated the first near real-time VLBI, where data was transmitted to the central correlator facility using fiber optics. Clock distribution from a central station through fiber optics has also been explored and successfully demonstrated [Clivati et al. 2017].

3.3 8 km LBI Experiment

The main objective of carrying out this experiment at Gauribidanur was to verify the existence of structures $\sim 1'$ in the solar corona, whence the radiation low frequencies originate. The result of this experiment would also be a precursor to the third phase of the GRAPH expansion, where it is sought to image these spatial fine structures, with baselines ~ 10 km, which would provide effective resolution of $\approx 1'$ at low frequencies.

Considering the above distance, and the exploratory nature of the study, it was decided to design a complete LBI type receiving system, with independent receivers, where the analog signal from the antenna will be band-limited, digitized, and recorded in servers located remotely. The signals will be transported to a central location where correlation and processing will happen. The observations carried out during the course of this experiment was limited to the local meridian transit to minimize errors due to the variations in the ionosphere.

Figure 3.6 shows the block diagram of our observational setup. Subsequent Sections (3.3.1 – 3.3.6) describe the analog and the digital components of the data recorder, characterization tests and experiments, and the actual 8 km baseline observations, the data analysis methodology, and the obtained results.

3.3.1 Antennas and Analog Front-end

The experiment used Log Periodic Dipole Antenna (LPDA) as the primary receiving element. A LPDA was chosen over a simple dipole as it has a wide frequency response, which would give us the flexibility of frequency hopping to avoid RFI. It belongs to the class of antennas, whose dimensions are defined in terms of angles, rather than lengths. The Rumsey's Principle states that such antennas have electrical characteristics that are uniform over a wide frequency range.

The construction of the Log Periodic dipole antenna is shown in Figure 3.7. It consists of dipole arms of varying lengths attached to a metallic "boom". The arm lengths and spacing are in log-periodic intervals. The adjacent arms are connected in a criss-cross fashion to maintain 180° phase difference between them to allow in phase addition of signals. The length

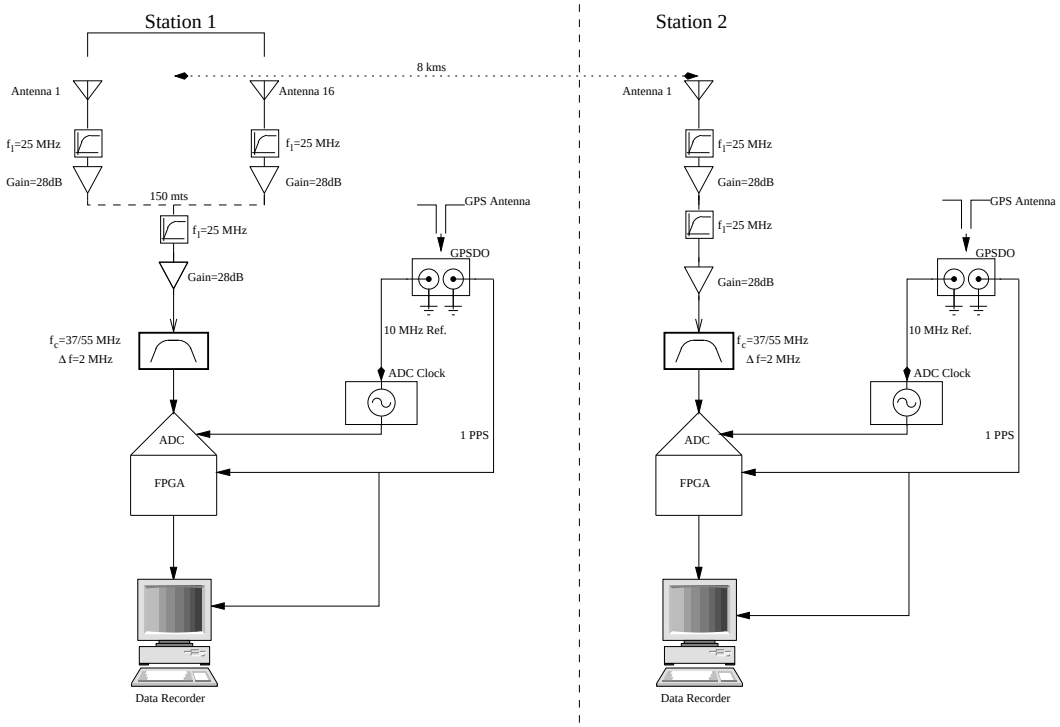

Figure 3.6: The experimental setup used for the 8 km LBI observations

of the shortest and the longest arm decide the highest and the lowest operating frequency, respectively.

The main factors used in the design of the LPDA are:

1. the design constant, τ,
2. the spacing factor, σ, and,
3. the half apex angle, α

The above factors can be obtained from the plot shown in Figure 3.8.

The required gain of the LPDA required is a quantity that has to be chosen by the designer, based on effective aperture, and beamwidth requirements. We needed a beamwidth of $\approx 60°$ in the RA, and $\approx 90°$ in the Dec axis. From this, we chose a gain of ≈ 6.25 dBi. Using the optimal gain curve would result in a large antenna size. Due to the nature of experiment, it was envisioned that the antenna had to be transported to remote

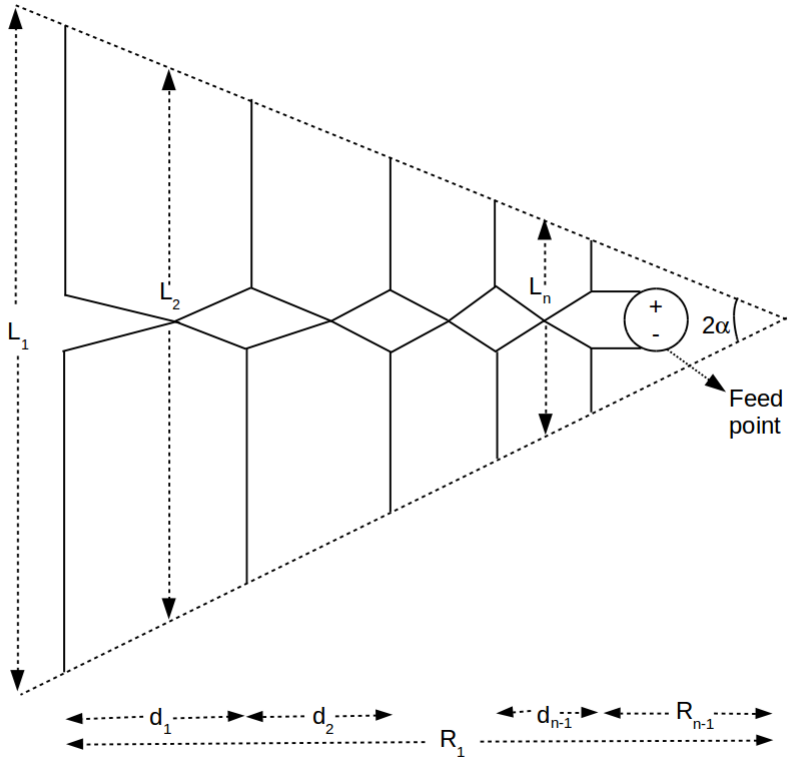

Figure 3.7: A Log Periodic Dipole Antenna

locations. This led us try different combinations of the design parameters and we finally fixed $\tau \approx 0.86$, $\sigma \approx 0.06$, and $\alpha \approx 29°$.

The highest and the lowest frequency of operation (f_h and f_l) required was 60 MHz and 30 MHz, respectively. f_h and f_l are related to the design constant, τ as:

$$f_l = \frac{\tau}{f_{l+1}}, \tag{3.10}$$

and

$$f_h = \frac{\tau^{h-1}}{f_l} \tag{3.11}$$

The relation can be generalized as:

$$\log f_{n+1} = \log f_n + \log \frac{1}{\tau}, \tag{3.12}$$

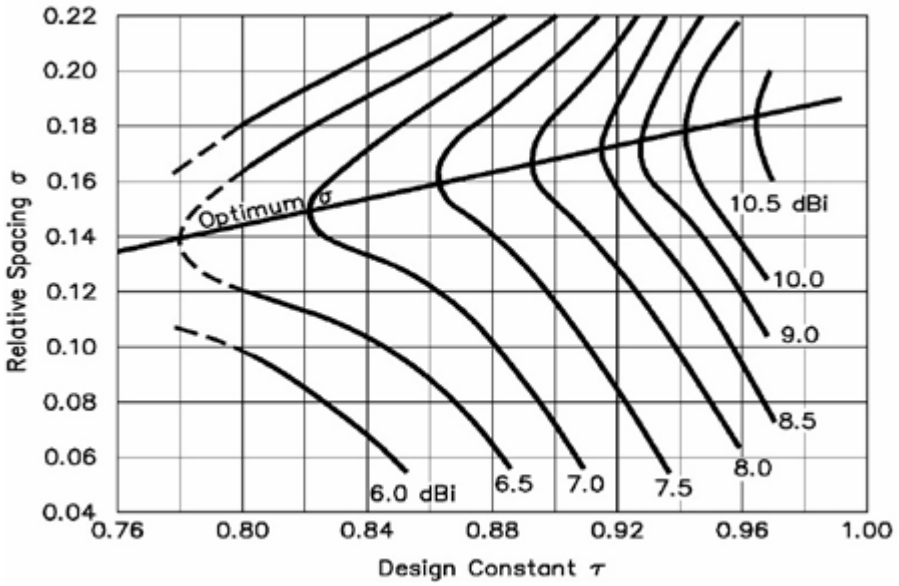

Figure 3.8: A plot of variation of Gain of the LPDA with relative spacing, σ between the arms, and the design constant, τ. This figure was adopted from Carrel [1966].

where f_n and f_{n+1} is the frequency of operation of the n^{th} and the $(n+1)^{th}$ arm respectively. The ratio of the highest and the lowest frequency is defined as the antenna bandwidth, β.

In the Figure 3.7, spacing between the n^{th} and the $(n-1)^{th}$ arm is d_{n-1}, the length of the n^{th} element is L_n, and R_n is the distance of the n^{th} element from the antenna apex. Using the above information, the design constant, τ can be written as,

$$\tau = \frac{L_n}{L_{n-1}} = \frac{d_{n-1}}{d_{n-2}} = \frac{R_n}{R_{n-1}}, \tag{3.13}$$

and the relative spacing factor, $sigma$ is:

$$\sigma = \frac{d_{n-1}}{2L_{n-1}}. \tag{3.14}$$

From the above equations, the relation between α, τ and σ is:

$$\sigma = \frac{1-\tau}{4\tan\alpha}. \tag{3.15}$$

S.no.	Spacing [m]	Apex distance [m]	Arm length [m]	Frequency [MHz]
1	0.00	0.00	0.97	77.32
2	0.25	0.25	1.11	67.57
3	0.26	0.51	1.25	60.00
4	0.32	0.83	1.43	52.45
5	0.4	1.23	1.65	45.45
6	0.43	1.66	1.89	39.68
7	0.52	2.18	2.18	34.40
8	0.58	2.76	2.5	30

Table 3.1: Design estimates obtained after using Equation 3.10 – 3.16.

The total number of elements, N of the antenna can be calculated as:

$$N = \frac{\log \beta}{\frac{1}{\tau}}. \tag{3.16}$$

It is to be noted that all the aforementioned design equations are for free-space. This would require some corrections to be made in the actual design.

Using these equations, we designed an antenna whose parameters are listed in the Table 5.2.

Once the antenna was designed, the next step was to verify the various parameters of the antenna like Voltage Standing Wave Ratio (VSWR), Antenna Gain, Half Power Beam Width (HPBW) in both the principal planes, *etc.*. The definition of VSWR, its importance and methods of measuring it is provided in Chapter 2. For the designed antenna, the VSWR plot is shown in Figure 3.9. The plot shows that the VSWR$\leq$2, at frequencies between 25 MHz and 70 MHz.

Next, the beam pattern of the antenna was measured to obtain the gain, and the HPBWs of the principal planes. For this, an antenna whose characteristics are already known is used as the radiatior, and the designed antenna was used as the receiver. A CW source was used as the input of the transmitter antenna, and the patterns were measured at three frequencies: 30 MHz, 45 MHz, and 60 MHz. On the receiving end, the output of the antenna was connected to a spectrum analyzer, where the power at all the

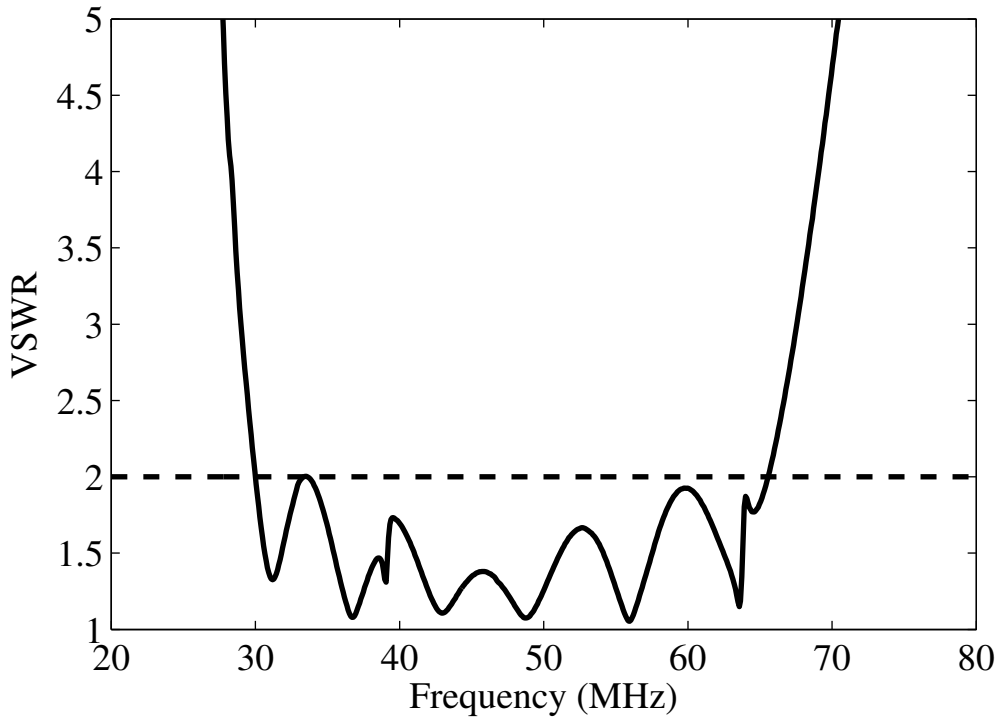

Figure 3.9: The VSWR of the designed antenna. The frequencies where VSWR≈2 indicates the lowest and the highest frequency of operation.

radiated frequencies were measured. The set-up used for the measurement of the antenna beam pattern is shown in Figure 3.10.

The receiver antenna can be moved along the azimuth and elevation axis to scan across the source to obtain an angular profile. The antennas must be placed at a distance greater than the far-field of the highest frequency. The radiation pattern obtained is shown in Figure 3.11.

From the Figures 3.11a and 3.11b, we can estimate the HPBW in the E and the H planes as 55° and 107°, and the gain to be ≈ 7 dBi. The collecting area of the single antenna is $\approx 0.4\lambda^2$. The Front-Back ratio is ≈ 34 dB.

The sky signal measured by the antenna is ≈ -110 dBm. This signal is broad-band, and white-noise like in nature. The weak signal has to be conditioned by the way of amplifying and filtering before it is in the appropriate power level to be detected for recording. These operations are performed in the analog front-end. Also, the analog system must add

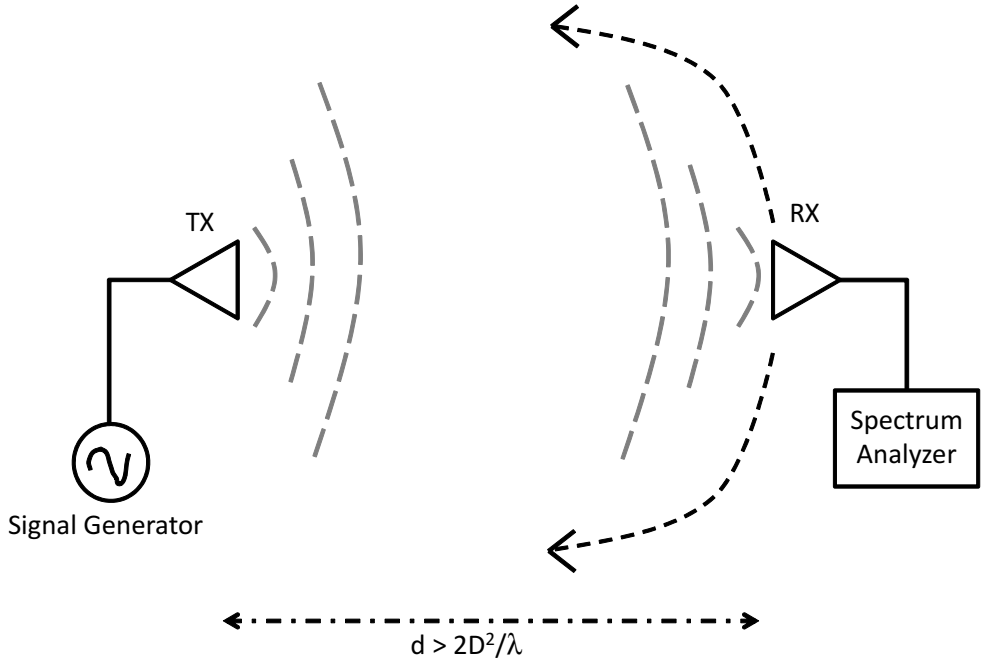

Figure 3.10: Beam pattern measurement setup.

minimal noise to the detected signal to ensure a good SNR.

The LNA used for most of the experiment was a MAN-1LN. This amplifier was characterized for its gain, dynamic range, 1dB compression point, and third order intercept points using the techniques described in Chapter 2. The measured characteristics of this amplifier is summarized in Table 3.2.

The sky signal that is amplified by ≈ 30 dB is filtered using a tunable band-pass filter. The filter characteristics with its center tuned to 37 MHz is shown in the Figure 3.12. From the plot, it is seen that the insertion loss of the filter in the pass-band is ≈ 1 dB. The return loss is ≈ -20 dB, both at the input and the output ports of the filter. The filtered output is the input to the digital data recorder (described in the next section).

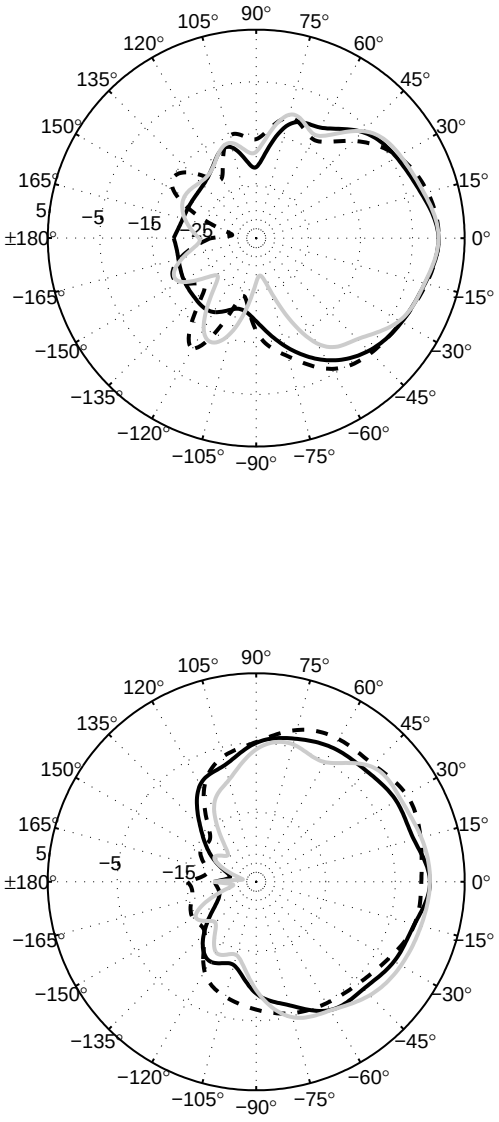

Figure 3.11: (a) The E-plane and (b) the H-plane radiation patterns.

Table 3.2: Amplifier Characteristics.

Parameter	Value
Gain	30 dB
Noise Figure	3 dB
Frequency	0.5 – 500 MHz
1dB compression (output)	≈+5 dBm
3^{rd} order intercept point	+15 dBm

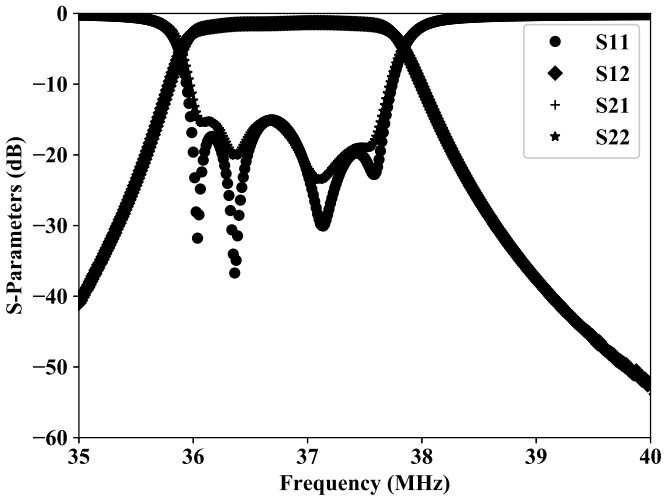

Figure 3.12: Filter characteristics. A tunable Lorch 5TF-24/48-5S 5 stage band-pass filter was used. The center frequency was tuned to be at 37 MHz.

3.3.2 Data Recorder and Synchronization

The purpose of the data recorder in LBI experiments is to digitize the analog data, time stamp them, and store them in a data acquisition server for later correlation. Since these data recorders will be used independently at individual stations, they must be synchronized to a stable reference. Thus, this section deals with the design of the data recorder and the synchronization system together. Note that in legacy VLBI experiments, where the RF was downconverted to IF, the LO also had to be synchronized. But since in the work presented here, the RF was digitized directly, we will not discuss

LO synchronization.

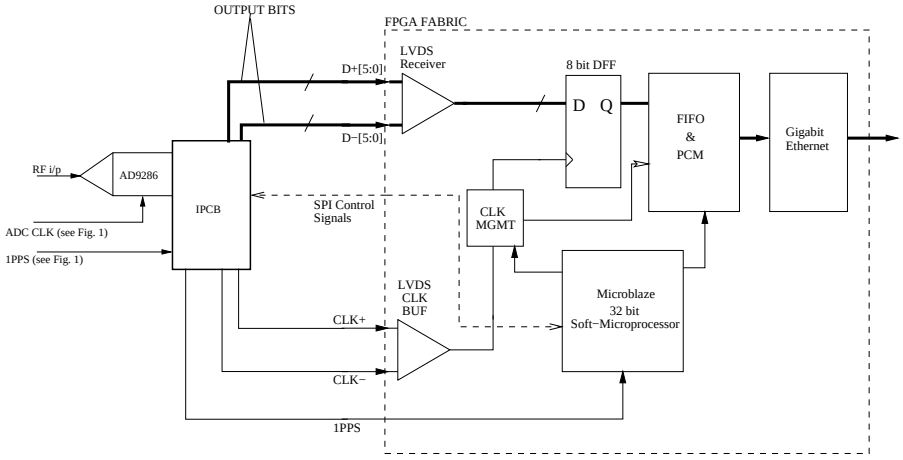

Figure 3.13: Description of the digital firmware used in the experiment

The Figure 3.13 shows the block diagram of the data recorder firmware. The firmware was implemented on an XUPV5[1] development board. This board contained a Virtex-5[2] family FPGA, along with which various data transfer interfaces such as Universal Asynchronous Receive/Transmit (UART), Gigabit Ethernet (Gbe), 10 Gigabit Ethernet (10 Gbe), Peripheral Component Interconnect Express (PCIe), etc., which provide high speed connectivity. It has an Expansion header, which allows inferfacing with external components, through Low Voltage Differential Signaling (LVDS), and Low Voltage Complementary Metal Oxide Semiconductor (LVCMOS) signals.

It was decided to build the data recorder, such that it will be capable of sampling bands upto 32 MHz. This would help in wide-band LBI observations, whenever necessary. For sampling a bandwidth of minimum 32 MHz, an ADC capable of a sampling rate of 64 MHz is required. For this, we used AD9286[3], a dual channel, interleaved ADC, capable of sampling rates upto 500 MHz. The ready availability of the evaluation board of this component in the observatory helped in accelerating the design process.

[1] https://www.xilinx.com/univ/xupv5-lx110t.htm

[2] https://www.xilinx.com/support/documentation/data_sheets/ds100.pdf

[3] http://www.analog.com/en/products/analog-to-digital-converters/ad9286.html

This ADC outputs 8 bit LVDS data, along with a differential version of the sampling clock. The ADC evaluation board can be interfaced to the FPGA board through the Expansion header. However, the ADC outputs were routed to a ZPACK high density connector on-board the evaluation board. Thus, we built an interface card, that would act as an "adapter" between the different PCBs. Due to pin constraints, only the most significant 6 bits of the digitized outputs are recorded.

The ADC output data and clock will be captured on the FPGA using `IBUFDS` and `IBUFGDS` primitives, respectively. These primitives will receive the digitized data in parallel synchronously. The outputs of the former will be combined in a bus to obtain the 6 bit ditized data. Since the whole system has to synchronously operate with the ADC sampling clock, the output of the `IBUFGDS` is fed to a `DCMPLL`, to obtain phase locked clocks, whenever necessary. The output clock of the PLL will resample the 6 bit digitized data in an array of flip-flops. The PLL output can be programmed to obtain different sampling clocks, as per the analog bandwidth and the data rate constraints.

The independent ADC clocks have to be synchronized to enable voltage correlation at a later point of time. Synchronization has been traditionally been performed using atomic standards like Hydrogen Masers, and Rubidium clocks, etc.. These systems are bulky, and also very costly. Since this experiment was more of a path-finder, we looked for smaller/portable and cost-effective alternatives.

Global Positioning System (GPS) satellites are fitted with an atomic clock for accurate time keeping, and position measurements. The 1 Pulse Per Second (PPS) signal from GPS receivers have been used traditionally as time markers for networks, cellular base stations, and other precision time keeping applications. A new generation of oscillators have taken advantage of this accurate 1 PPS signals by synchronizing them with crystal oscillators. Such a system is called a GPS Disciplined Oscillator. GPSDOs provide an effective trade-off between the accuracy of the atomic clocks, and the compactness of the crystal oscillators. These are effectively "Stratum 2" clocks because the oscillator output is synchronized to the 1 PPS, which in turn is synchronized to the atomic clocks, on board the GPS satellites. The synchronization scheme of our experiment involving GPSDO

is shown in the Figure 3.14. The GPSDO used in our experiment was a Trimble Thunderbolt-E[4].

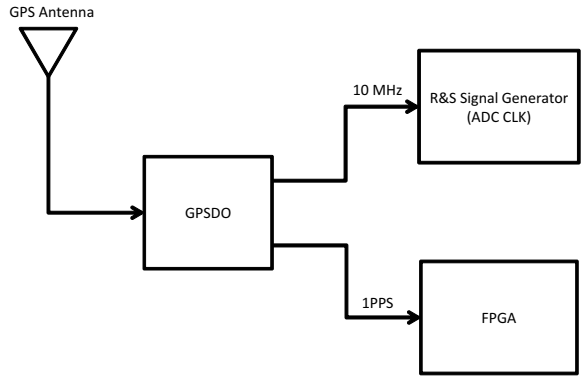

Figure 3.14: Synchronization scheme of the experiment

The GPSDO outputs a 10 MHz CW reference signal, and a 1PPS pulse. The 10 MHz signal is used to lock the Rhode and Schwarz (RS) signal generator, which supplied the ADC sampling clock. The ADC sampling clock was fixed to be 64 MHz.

A SMA connector was provided on the interface card that connected the ADC and the FPGA boards. The 1PPS connector was input to this SMA connector. Since the 1PPS was a Transistor Transistor Logic (TTL) signal, and the FPGA can only tolerate a maximum input of 3.3V, a level shifter was used to translate the signal to the desired level. The GPSDO also has a serial link that is connected to the observation data acquisition server to synchronize its time with respect to GPS time.

The 1PPS signal is sampled by another flip-flop at the same sampling

[4] http://www.trimble.com/timing/thunderbolt-e.aspx

clock as the data and is packed as the most significant bit (MSB) of the data byte. The 7^{th} bit is packed with 0. Thus the constructed data byte will look like: `[1PPS,0,data[5:0]]`. The 1PPS signal thus packed will act as a 1 second boundary marker, and can be used to synchronize the data streams.

The sampled, constructed data bytes have to be buffered and transmitted in a proper time order. For this, the buffering is done in a First-In-First-Out (FIFO) buffer. The FIFO is also important in situations where the data has to be sent across different clock domains. The data output from the FIFO is transmitted through Gbe. Of all the available interfaces, Gbe was chosen due to its ease of development and the fact that it can be used on any readily available data acquisition servers. The maximum bytes that can be transmitted using Gbe normally is 1500. However, jumbo-frames can transmit upto 8000 bytes. In this version of the data recorder, the former was used. Gbe was implemented on the FPGA as an Intellectual Property (IP) core. The core works at a maximum clock rate of 125 MHz. This sets the limit on the write clock, and the depth of the FIFO.

If one proceeds according to this, writing 1 sample to the FIFO, assuming a maximum of 32 MHz band is digitized, will take ≈ 15.625 ns; reading it out will take 8 ns. Thus, for a frame size of 1024 data bytes and header of 58 bytes, a total write-time of 16.90625 μs. Reading this out takes a total of 8.656 μs. Thus, the depth of the FIFO must be atleast twice the size of a data frame. In our case, due to the availability of resources on-board the FPGA, we set the FIFO depth to be 4k. Thus, FIFO overflow can be avoided when data is being streamed.

The data has to be *packetized* before transmission through header. Ethernet communications describes a packet format[5] for this. All the requisite packet data were stored in a text file, which was instantiated to address $0:41$ of `HDRRAM` during synthesis. Along with the ethernet header, two extra words of information were added to the data packet: one was the PPS count elapsed since the beginning of the observation, second was the packet count. Both these counts enabled us to identify ethernet packet loss.

To achieve this streaming, and obtain handshake between the FIFO,

[5] `https://wiki.wireshark.org/Ethernet`

HDRRAM and the Gbe core, a controller was implemented in Verilog. The controller takes the PROGFULL signal of the FIFO, and the clock signal of the Gbe core as the input. Once the PROGFULL is initiated, the reading of header from the HDRRAM commences, along with which the ETHEN and SOF signals are pulled low. SOF is pulled low for just one clock cycle, whereas ETHEN is maintained low for the read duration of a whole packet. A multiplexer is used to alternate loading of data into the Gbe core from the HDRRAM and the FIFO. After the last header byte is read out, a FIFORDEN signal is asserted. This is the input to the multiplexer SEL port, and the RDEN port in the FIFO. Once 1024 data samples are read from the FIFO, an EOF signal is transmitted to the core to indicate the end of a packet.

The FPGA firmware was controlled through a Microblaze[6] soft processor core. Microblaze is interfaced to the data acquisition server to provide user control via UART. Microblaze also accurately counts the number of 1PPS pulses to help in time keeping. A typical observation event progresses as follows: An observation start time is set in the data acquisition server via Python programming; once this time elapses, a initiation signal is sent to the microblaze softprocessor, which initiates the observation; After the observation duration, which is user programmable, has elapsed, microblaze terminates the observation, by pulling the WEN signal of the FIFO low, which prevents further data transmission. On the data acquisition server, TCPDUMP[7], an open source network data capture program, captures the ethernet data and stores it in a binary file. The name of the binary file contains the instant at which the observation started at that respective system.

3.3.3 Characterization

The designed system was characterized before science observations to understand the capabilities and the limitations of the system. Two tests were performed for this: i) Noise tests, ii) Short baseline observations. These tests and their results are described in the subsequent sections.

[6] https://courses.cs.washington.edu/courses/csep567/04sp/pdfs/lectures/L4-MicroBlaze.pdf

[7] http://www.tcpdump.org/tcpdump_man.html

3.3.3.1 Noise Tests

In noise test, correlated noise was provided to both the data recording systems, in parallel. This test was carried out in two phases: i) when both the data recorder clock were from a single signal generator, ii) when the data recorder clocks were from different signal generators, which were synchronized to the GPSDO. The former helps us to ensure the quality of the data recorded in both the recorders, while the latter gives us a handle on the loss of correlation due to using independent clocks, synchronized externally. The Figure 3.15 shows the setup used in both the aforementioned tests.

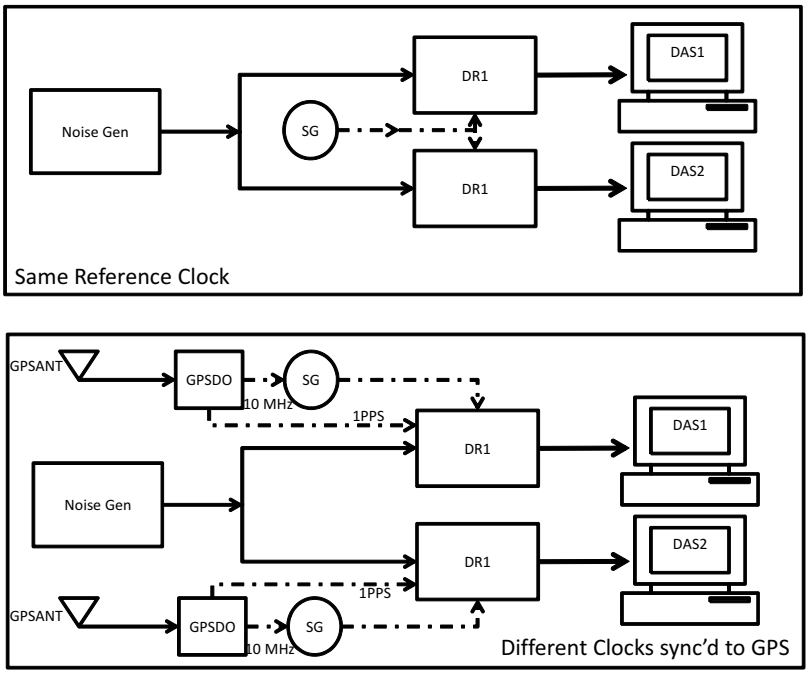

Figure 3.15: Noise Test experimental Setup

Noise signal is power divided using a 2:1 power splitter, and is given as the input to the ADCs of the data recorders. Through different tests carried out on the ADC, it was seen that a total input power of -30 dBm was optimal to obtain an ENOB of 3, while the remaining 3 bits can be used to accommodate transient increase in the power level during observations due to RFI or solar radio bursts. The noise generator output was maintained

at this level during the tests.

During the first test, a single R&S signal generator was used to sample signal at each ADC. The input signal bandwidth was ≈ 2 MHz. The trial as well as science observations were carried over a bandwidth of 2 MHz during the first campaign to keep the data rates to manageable levels. The noise signal was toggled ON-OFF-ON during the duration of the test to find the difference in correlation when a coherent source is present or absent. The data from each recorder were acquired in two independent data acquisition systems, whose times were synchronized to GPS. This ensured that the recording of the noise signal commenced at the same time in both the systems. This test yielded the expected result: during the duration when the noise source was ON, almost full correlation was achieved. In other words, the data was recorded in both the systems at the same clock edge, and the correlation coefficient, $\rho \approx 1$. ρ can be defined as correlation counts that have been normalized with respect to the product of the autocorrelations of the individual channels. In other words:

$$\rho = \frac{C_{12}}{\sqrt{A_1 A_2}}, \tag{3.17}$$

where C_{12} is the cross-correlation between the channels 1 and 2, while A_1 and A_2 are the autocorrelations of channel 1 and 2, respectively. The results of the tests carried out with same sampling clock indicates that there is no loss of coherence due to using the data recorders, or the individual acquisition servers, where the data is recorded. But in actual experiment, we would be using two independent clocks. So the same test was repeated with different clocks.

The difference of this setup with respect to the first one is that the sampling clocks of the two data recorders are now two independent R&S signal generators. These signal generators were referenced externally to 10 MHz signal from two GPSDO modules, whose antennas were mounted $\approx$ 10m apart on the ceiling of the receiver room. This result of this test is shown in Figure 3.16.

It is seen that the maximum value of ρ $\approx$0.65. The spikes in the plot correspond to 1PPS signals. This shows that usage of independent GPSDO modules lead to a loss in correlation of $\approx$0.35. This test was repeated and it was determined that over a long term, ρ varies within 1% of this value.

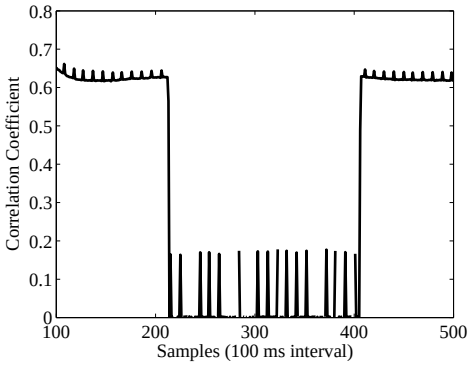

Figure 3.16: Results of noise test with two independent sampling clocks, synchronized externally to GPSDO.

It was attempted to validate the system observationally to verify if the above ρ value obtained when using different clocks are within tolerable limits. This is described in the next section.

3.3.3.2 Short Baseline Observations

In this characterization phase, instead of noise signal, signals from two antenna groups of GRIP/GRAPH were provided as the input to the data recorder. This test was undertaken in three phases. In the first phase, the setup was placed inside the GRAPH receiver room, and the signal from two groups of GRIP, whose antennas were oriented in the same direction was used. The spacing between two such groups in GRIP was ≈120 m. The group outputs were tapped at the input of the analog front-end module in GRIP rack. The tapped signal was bandlimited to 2 MHz, about 37 MHz. The filtered signals from the groups were amplified to provide optimal power levels as input to the data recorder. The observations were performed for ≈ 1 hr around the meridian transit of strong calibrator sources. The fringes obtained from this test for the radio source Cygnus-A is shown in Figure 3.17.

The results of this test validated the performance of the system in short baselines. Next, we carried out the same test using longer baselines available in GRAPH. For this, we selected two groups that had equal length cables running to the receiver room, where the recorder system

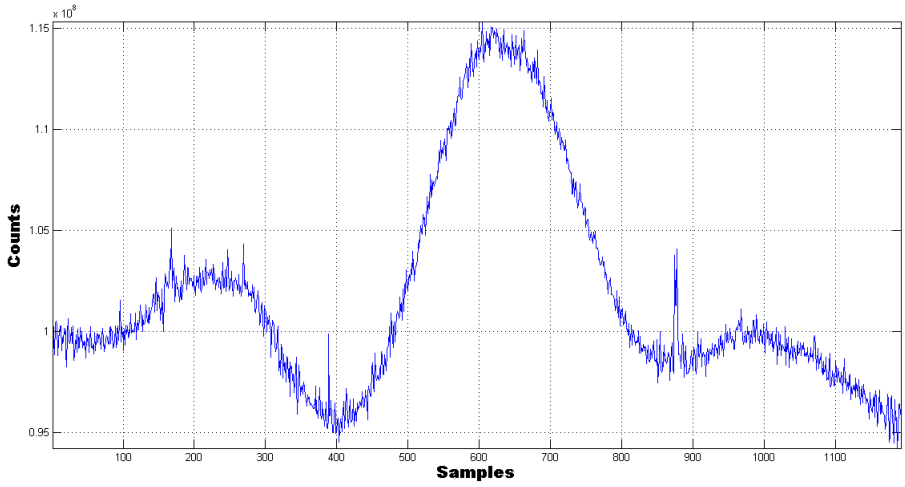

Figure 3.17: Cygnus-A short baseline observations. Observation start time is 19:45 LST, and each sample is ≈ 1.04 s.

was housed, to minimize the complexities. The sensitivity of this system, estimated using Equation 3.8 assuming T_{sys} dominated by sky-noise to be 50000 K, would be ≈ 300 Jy. The observations were carried out for all the four primary calibrators used at Gauribidanur. The Figure 3.18 shows the obtained fringes in the long baseline for all the four sources.

The obtained values of SNR show that the sources are unresolved over the 2 km baseline. The results also indicate that for observation of these strong sources, and the Sun, which during times of activity will be ≈ 3-4 magnitudes stronger than the above sources, the loss in SNR due to different clocks, is not too significant. These tests were repeated by moving the data recorders to the field and placing them in a shed close to the antenna groups. The results from these observations were similar to those obtained when the receivers were placed in close to each other, in a controlled environment. This test showed that the system was sufficiently rugged for field observations.

On this note, we proceeded to the next stage, which would mimic our 8 km long observations. In this set of trials, we used the Antenna described in Section 3.3.1 as one arm of the interferometer. For the other arm, a 16 antenna group from GRIP was used. The single antenna was mounted ≈

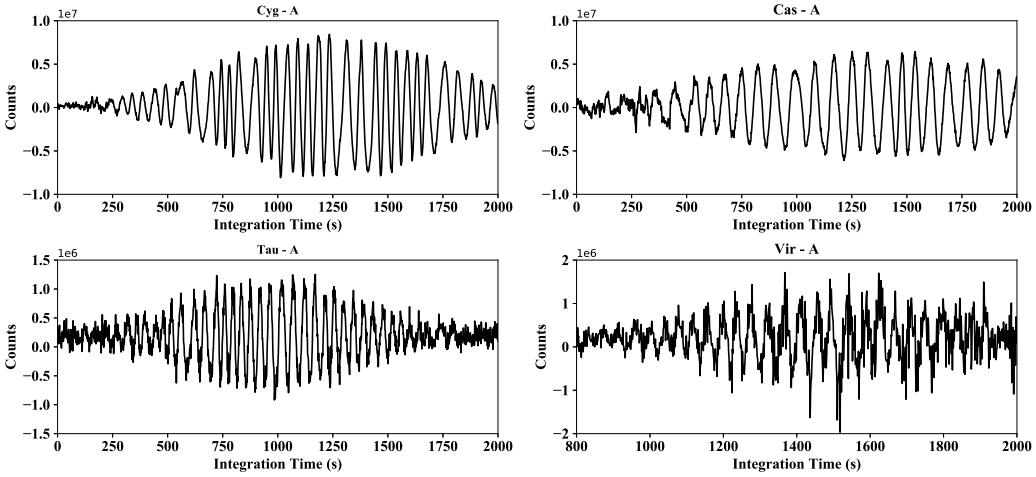

Figure 3.18: Observations of all four calibrator sources in the long baseline. The plot is shown only for the duration of the local meridian transit. The integration time is 1.04 s.

1.5 km from the phase center of the GRIP group. One of the data recorder was housed inside the observatory, where the group signal from GRIP was obtained as described earlier in this section. The other data recorder was placed in a shed close to where the single antenna was mounted.

Initial verification of the RF band showed the presence of an broadband RFI signal. This was later traced to the the Switched Mode Power Supply (SMPS) of the data acquisition server. So, the system was shielded to isolate the RFI from the antenna band.

Figure 3.19 shows a plot of the obtained SNR for all the four calibrator sources observed with this setup.

The next section describes the 8 km LBI experiment.

3.3.4 GRIP-TIFR Interferometer Description

The observational setup used for this experiment was shown in Figure 3.6. The setup comprised of two stations. Station 1 of the interferometer is one of the 16 antenna groups in the Gauribidanur Radio Interferometric Polarimeter. Station 2 consists of a single LPDA. The LPDAs in both the stations are oriented in the east–west direction. The width of the re-

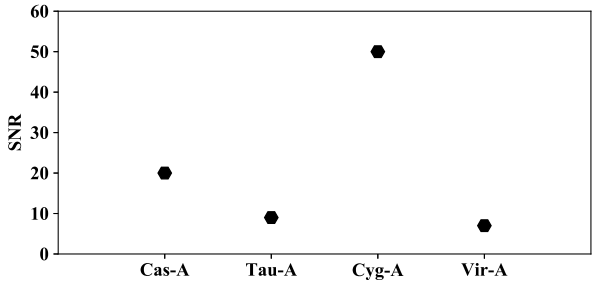

Figure 3.19: SNR of the observed sources

sponse pattern ("beam") of Stations 1 and 2 are ≈ 3°×90° (Right Ascension (R.A.)×Declination (decl.)), and ≈60°×90°, respectively. This indicates that their combined response (field of view, FOV) in the cross-correlation mode is ≈3°×90°. The effective collecting area of Station 1 and Station 2 are $0.5\lambda^2$ and $8\lambda^2$, respectively.

The length (D) of the baseline between the two stations is ≈ 8 km in the east–west direction. Its minimum detectable flux density at 37 MHz is ≈ 1500 Jy (1 Jy=$10^{-26} W m^{-2} Hz^{-1}$) for an observing bandwidth of ≈100 kHz and integration time of ≈50 ms.

Note that the present antenna setup belongs to the category of rectangular or linear aperture with field only at the edges. In such a case, the half-power beam width is ≈ $29\frac{\lambda}{D}°$ [Kraus 1966]. In the present case, D ≈ 8 km and λ=8.1 m. So the beamwidth is ≈1.5′.

3.3.5 Observations

During the first observing run with the LBI system in 2015 July, we carried out observations of Cygnus A (3C405) and the Sun at 37 MHz around their respective transits over the local meridian in Gauribidanur. Figure 3.20 shows the plot of the visibility amplitudes obtained from observations of Cygnus A.

But Cygnus A has an extent of ≈ 2′, and the angular resolution of the LBI experiment in the present case is at 37 MHz is ≈1′. This implies that the source should be marginally resolved [Kassim et al. 1996]. From the calibrated UV-data available in the NRAO archive and assuming a spectral

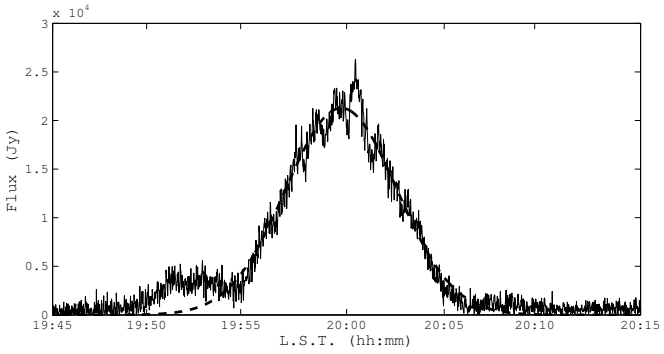

Figure 3.20: Drift scan of Cyg-A obtained with the LBI. The solid line is a Gaussian fit to the data.

index[8] of ≈ -0.7, we calculated the likely flux density of Cygnus A at the above angular resolution at 37 MHz to be S ≈ 21,273 Jy. Moving to solar observations with the LBI, we found that intense nonthermal radio emission from the Sun was observed with the GRAPH at 55 and 80 MHz during the period July 9 – 13 2015. Similar emission was reported from observations elsewhere[9], also around the same time. The long-lasting (∼ days) nature of the activity clearly indicates that it must be a noise storm source, since there are no other known sources of such radio emission from the Sun at low frequencies [Elgarøy 1977, Kai et al. 1985, Ramesh 2011]. Otherwise the Sun was "undisturbed" in 2015 July, particularly close to its transit time in Gauribidanur. Since we had simultaneous observations with the LBI at 37 MHz during July 10-12 2015, we present the same here. Figure 2 shows the plot of the visibility amplitudes obtained from the Sun on 2015 July 10 at 37 MHz in the meridian transit mode. The coordinates of the Sun on the above date were R.A. ≈ 06h55m universal Time (UT) and decl. ≈ 22.3°, respectively. We used Cygnus A observations to calibrate and convert the observed raw solar data to flux density values. There is clear evidence for correlated emission in the FOV of the LBI. Similar emission was observed on July 11 and 12 2015. This indicates that discrete source radio sources of angular size ∼ 1′ are present in the solar corona from

[8]Spectral index (α) is the coefficient of a power law relation ($S \propto \nu^{-\alpha}$) that describes the variation of flux with frequency.

[9]`ftp://ftp.swpc.noaa.gov/pub/warehouse/2015/2015_events/`

where the 37 MHz radiation originates.

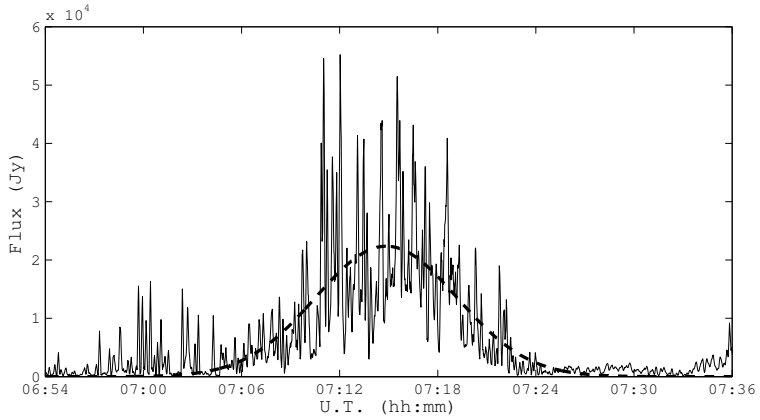

Figure 3.21: Observations of solar noise storm with the LBI. The dotted-line is a Gaussian fit to the data.

3.3.6 Analysis and Results

The angular size of the noise storm continuum sources mentioned in the literature are $\approx 23\,'$ at 38.5 MHz [Kundu and Gopalswamy 1990]. Such large-sized sources are expected to be completely resolved with observing instruments that have an angular resolution of $\approx 1'$ at 37 MHz, as in the present work. This implies that the LBI observations in Figure 3.21 correspond primarily to the noise storm bursts whose angular sizes are smaller than that of the continuum [Kai et al. 1985]. The present observations indicate that the sizes of the above bursts at 37 MHz are $\sim 1'$. Their peak flux densities are in the range $\approx (0.5 - 6.0) \times 10^4$ Jy. Assuming circular symmetry for the source size, we find that the corresponding peak brightness temperatures (T_b) are $\approx (0.1 - 1.7) \times 10^{10}$ K. These values are in reasonable agreement with the predicted T_b ($\approx 5 \times 10^{10}$ K) for strong noise storm bursts at 37 MHz [Thejappa 1991]. We estimated the total flux density of the bursts in the present case from the auto-correlation of the signal received by Station 1 (i.e., the total power measured with zero baseline or spacing interferometer) in the LBI setup, and the value is $\approx 8.3 \times 10^4$ Jy. The contribution of the "background" solar corona to the above can be

neglected, since it is expected to be comparatively very small at 37 MHz, $\approx 2\times10^3$ Jy [Erickson et al. 1977]. These indicate that the flux density of the noise storm bursts observed with the LBI is $\approx (0.06 - 0.72)$ times their total flux density. We also calculated the likely flux density of the background continuum at 37 MHz on July 10 2015 using GRAPH observations at 55 and 80 MHz around the same epoch, and the value is $\approx 1.5 \times 10^4$ Jy. A comparison of this with the flux densities of the bursts at 37 MHz indicates that the latter are $\approx 0.1 - 4$ times the above value. Considering that the bursts are fluctuations of varying amplitude superimposed on the background continuum (Kai 1985), we find that at 37 MHz their flux densities are $\approx (0.3 - 4)$ times above the flux density of the background continuum. Since the latter is resolved in the present LBI observations, we are able to notice even the bursts with small amplitude. The aforementioned range of flux densities of the bursts with respect to the background continuum are consistent with the results reported in the literature (see for example Malik and Mercier [1996], Mercier and Trottet [1997]).

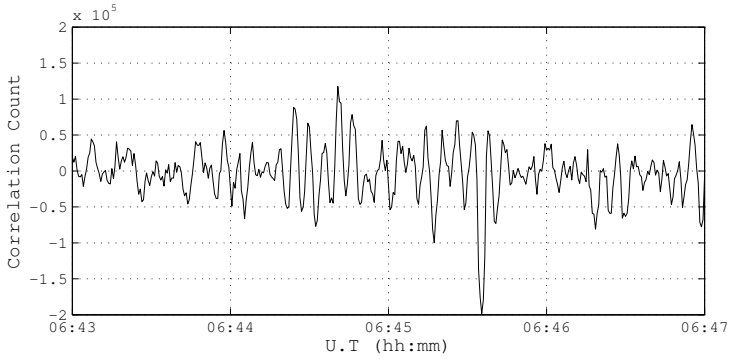

Figure 3.22: Observation of a Group of type III with the LBI on 9 Aug 2015.

Observations with the LBI during a type III burst on August 9 2015 indicate that it has a structure with an angular size of $\approx 1'$ at 37 MHz (see Figure 3.22). The calibrated peak flux density of the burst is ≈2000 Jy. This is about 4% of the total flux density ($\approx 4.8 \times 10^4$ Jy) observed at the same epoch with Station 1 of the LBI as mentioned above. The above values are in the range of flux densities of weak type III-like micro bursts at 38 MHz reported in the literature [Subramanian et al. 1993]. The peak T_b of the type III burst observed with the LBI, estimated assuming

circular symmetry for the source size as in the noise storm burst case, is $\approx 5.6 \times 10^8$ K. Since the lifetimes of type III bursts are limited ($\approx$ 25 s at a frequency like 37 MHz [Suzuki and Dulk 1985a]), we speculate that the interference fringes in Figure 3.22 between $\approx$ 06h17m – 06h18m UT and 06h18m – 06h19m UT could also be attributed to successive emission from two spatially separated type III burst sources that were active at corresponding epochs. Figure 3.23 shows the distribution of the noise storm bursts in Figure 3.21 with respect to their peak flux densities. An integration time of ≈50 ms was used to minimize the possible averaging of different individual bursts with short lifetimes. The fit to the distribution indicates that the latter follows a power-law pattern with an index (γ) of ≈-2.5. The power-law indices of the fit to the distribution of the noise storm bursts observed on 2015 July 11 and 12 are also nearly the same. The average value of γ for the above three days is ≈ -2.4. Considering that noise storm bursts are signatures of nonthermal processes involving small coronal magnetic energy releases [Benz 1995a], the above results are consistent with the prediction that the power-law index for the distribution of weak energy releases in the solar atmosphere should be <-2 [Hudson 1991].

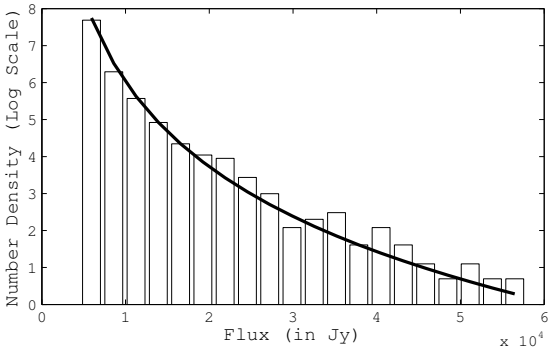

Figure 3.23: Flux distribution of noise storm bursts. The solid line is a power law fit with $\gamma \approx -2.5$

We calculated the energy of the burst source using the relation [Elgarøy 1977],

$$W = S\delta t \delta \nu R^2 \Omega e^{\tau}, \tag{3.18}$$

where δt is the duration of the burst, ν is the observing frequency, $\delta\nu$ is the bandwidth of the burst, R $\approx 150 \times 10^9$ m is the Sun–Earth distance, is the solid angle into which the radio waves are emitted, and τ is the optical depth.

In the present case, S$\approx (0.5 - 6.0) \times 10^4$ Jy, $\delta t \approx 50$ ms, and $\nu = 37\,MHz$. Assuming $\delta\nu = 0.02\nu \approx 0.7 \times 10^6$ Hz [Benz and Wentzel 1981], $\Omega \approx 0.15$ steradians [Steinberg et al. 1974], and $\tau \approx 1$ at 37 MHz (Ramesh 2005), we get $W \approx 6.4 \times 10^{16} - 1.7 \times 10^{18}$ erg for the noise storm bursts in Figure 3.23. Note that the above value was obtained by assuming an efficiency (η) of $\approx 10^{-6}$ for the noise storm emission process, which starts with the acceleration of the associated nonthermal electrons [Elgarøy 1977]. If we assume $\eta \approx 10^{-10}$ [Subramanian and Becker 2004], then $W \approx 6.4 \times 10^{20} - 1.7 \times 10^{22}$ erg. Either way, these are by far the weakest energy releases in the solar atmosphere ever reported observationally [Porter et al. 1995, Mercier and Trottet 1997, Krucker and Benz 1998, Parnell and Jupp 2000, Ramesh et al. 2010a]. This indicates that observations with short integration times and high angular resolution (which fully resolves the "background" corona as well as the noise storm continuum), as in the present case, are important to unambiguously observe the aforementioned weak energy releases. Note that in the presence of the noise storm continuum, the term S in Equation 3.18 can be $\sim 10^6$ Jy at low frequencies [Nelson et al. 1985]. Obviously W will be correspondingly higher.

3.4 GBD-GDK Experiment

The results obtained in the above experiment gave us confidence that small angular scale structures of size $\leq 1'$ can be observed in the solar corona. Given previous results obtained at Gauribidanur during solar eclipses, where sources of sizes $\approx$15" have been observed, we wanted to verify if such sources could be observed with a regular, interferometric observation setup as well. This was the motivation behind setting up the Gauribidanur-Gadanki Long Baseline Solar Interferometer. The description of the interferometer, the observations and the obtained results are discussed in the further sections.

3.4.1 Interferometer Description

We used a two element correlation interferometer setup for the observations. One "arm" of the interferometer was a group of 8 antennas from the Gauribidanur Radio Interferometric Polarimeter (GRIP, Station 1) while the other "arm" was the Indian Mesospheric-Stratospheric-Troposhperic Radar (MST, Station 2) at Gadanki (13.5°N, 79.2°E; Rao et al. [1995], Prasad et al. [2016]). The frequency at which the observations were carried out was 53 MHz. Note that the above corresponds to a heliocentric distance range of $1.48R_{\odot}$. Thus, we will be effectively probing radio-emission from the "middle" corona [Dulk and Sheridan 1974].

Station 1 comprised of 8 Log Periodic Dipole Antennas (LPDA) with the arms oriented parallel to the geographic N-S direction. The beam of Station 1 spans 3° in RA and 90° in Dec in NS. The collecting area of Station 1 is $\approx 128\text{m}^2$ at 53 MHz.

Station 2 is a planar array of 1024 Yagi-Uda antenna elements, power-combined as 32 sub-arrays. The field of view of the Station 2 is 20°x20°(RA x Dec). The antennas are power combined with the help of digitally controlled phase shifters, which provides flexible beam positioning, with $\approx 5°$ resolution, both in elevation (El) and azimuth (Az) axes, respectively. The size of the power combined beam is $\approx 2.5°$ in both the axes. Before the observations, the RA and Dec of the source was converted to Az and El, respectively to point the beam of the MST radar to the source. The collecting area of the MST radar is $\approx 16000\text{m}^2$ at 53 MHz. We characterized the array performance before commencing the experiment using observations of Virgo-A radio source, which is at the zenith at Gadanki's latitude. The Figure 3.24 shows the drift scan of Virgo-A, detected by the MST radar.

From the plot, it is seen that there is a beam offset of $\approx 0.5°$ towards the east. The aperture efficiency of the radar was found to be $\approx 87\%$, and it had a gain ≈ 36 dBi.

The above interferometer setup can be considered to be a linear aperture with field at the edges[Kraus 1966]. For λ ≈5.6m and D≈ 200 km, the angular resolution is ≈ 3″ at 53 MHz. The minimum detectable flux, S_{min} of the interferometer is ≈2000 Jy for a bandwidth of 10kHz and 2.5ms.

Identical analog and digital receivers were used for observations at both the stations. The power combined signals from the antennas at both the

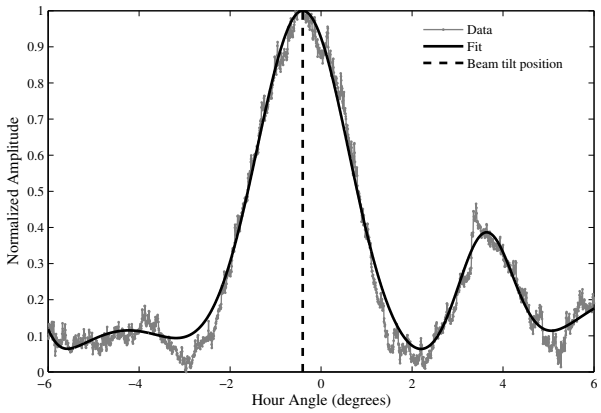

Figure 3.24: Meridian transit observations of Virgo-A using the MST Radar, Gadanki.

stations are band limited with a custom made 5^{th} order filter with lower and upper cut-offs at 48 MHz and 56 MHz, respectively. The output of the band pass filter is then amplified by $\approx$ 25dB before being fed to the Analog to Digital Converter (ADC). The same data recorder used in the previous experiment was used for this campaign as well, but with a minor modification. A PCIe based system was used for transferring the high speed data to the data acquisition system. This was implemented using an open source IP core called Xillybus[10], which enables Direct Memory Access of FIFO buffers on-board the FPGA. There was no data/frame loss when using this interface.

3.4.2 Observations

Trial observation runs were made on the radio source 3C274. This source, during its transit will almost be at the zenith at both the stations, due to which the former was observed with the MST in "Zenith Beam" configuration. While, the transit of the source was detected individually at both the stations, search for fringes returned a negative result. This is because for the baseline length ($\approx 30000\lambda$), there is no unresolved component greater

[10] `xillybus.com`

than the sensitivity of the interferometer on the source[11]. We did not observe any other calibrators as a survey of existing literature indicated that there were no compact sources within the field of view and the sensitivity limit of the interferometer. Thus, we use an alternate calibration strategy which is as follows: the flux measured by the single station of the interferometer, is estimated. This is the total flux of the observed source. The correlated flux, measured by the two element interferometer, is then estimated as a fraction of the total flux. Ideally, for an unresolved source, the total and correlated flux will be the same. In case of a resolved source, the correlated flux is less than the total flux; the difference is dependent on the size of the source.

Meridian transit observations of Sun was carried out over a period one hour for a span of 4 days from 2017, April 05 - April 08. The Sun was active only during the first day of observation i.e. 2017, April 05. We localized the observed bursts in raw voltage sample data from both the stations and correlated the same. The total correlated intensity plot is shown in the Figure 3.25.

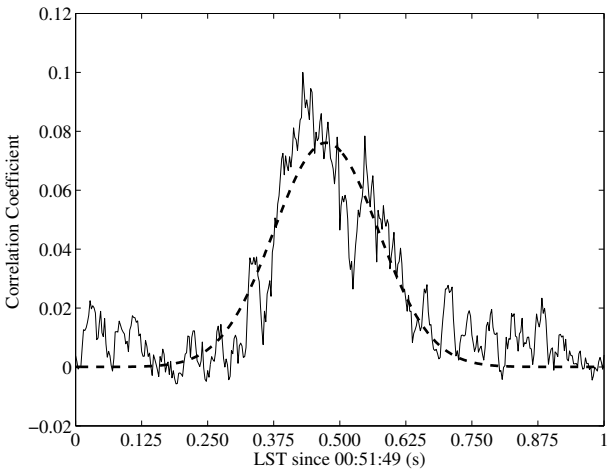

Figure 3.25: The correlated intensity plot of the observed burst. The dashed line is a Gaussian fit to the data. The y-axis is in ρ.

Though the burst is patchy in frequency, there is noticeable intense

[11]This was verified using archival 74 MHz VLA observations of 3C274

emission close to ≈ 53 MHz, the center frequency of the observations with the long baseline interferometer. Similar independent observations with the GRAPH at 53 MHz also confirmed this. The burst was located to the west limb of the Sun (Figure 3.27).

The associated active region is most likely AR12645 located at W65 on the Sun that day (2017 April 5). These imply that the aforementioned radio burst is most likely due to harmonic emission since fundamental emission from bursts near the limb will be attentuated by the overlying denser layers. There were no flaring activity during the burst period [12].

Therefore it is possible that the radio burst described above corresponds likely to the category of weak energy releases in the solar atmosphere. Low frequency radio observations are sensitive indicators of electron acceleration associated with such energy releases [Benz 1995b, Ramesh et al. 2010b, Oberoi et al. 2011, Ramesh et al. 2013, Suresh et al. 2017].

Equipped with the above information, we localized the observed bursts in the independent autocorrelation spectra from Stations 1 and 2 on 2017 April 5. Subsequently we correlated the respective raw voltage samples (corresponding to the same epoch during which the burst was noticed in the autocorrelation spectra) offline as mentioned above. Note that the visibility of a source on a particular interferometer baseline is defined as the ratio of the observed amplitude on that baseline to the observed amplitude on the 'zero' baseline (i.e. the total flux from the source). In the present case, the observed cross-correlation count (i.e. ≈ 2061) on the 200 km interferometer baseline was taken to be the peak burst amplitude on that baseline. The corresponding amplitude on the 'zero' baseline (estimated from the square root of the observed auto-correlation counts due to the burst at Stations 1 and 2) is ≈ 26320. The ratio of the two (≈ 0.1) is considered as the visibility of the burst on the 200 km baseline. The system noise in the above two amplitudes is expected to be nearly the same (since it is 0.5× the square root of the product of the individual system noises in Stations 1 and 2), and hence will get cancelled when we take the ratio. The profile of the burst observed with the long baseline interferometer is shown in Figure 3.25. The time interval of the burst (00:51:49.250 LST - 00:51:49.750 LST) is the same as the period over which the burst was observed with the

[12] ftp://ftp.swpc.noaa.gov/pub/warehouse/2017/2017_events

GLOSS (Figure 3.26). We repeated the correlation procedure with different delay values, however, maximum SNR was obtained only for a particular set of delay values. This gave us confidence that the obtained correlation corresponds to the burst.

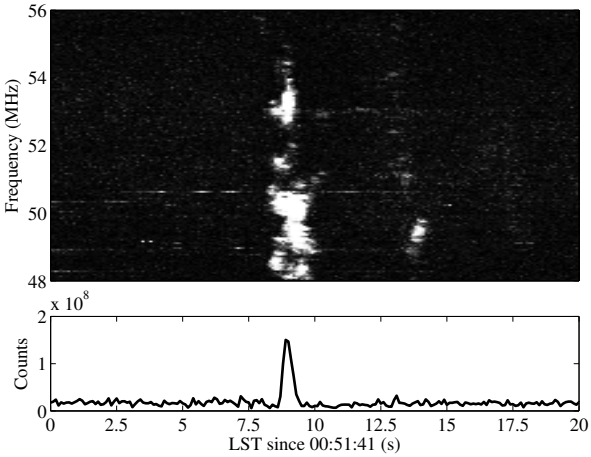

Figure 3.26: The dynamic spectrum of the burst and its time profile (bottom panel)

3.4.3 Analysis and Results

An inspection of the spectral observations of the burst with the GLOSS in Figure 3.26 indicates that they are characterized by narrow-band striae. A survey of the literature indicates that these are type IIIb bursts, a category of the type III bursts from the solar corona whose typical drift speeds are $\sim 0.3c$ [Ellis and McCulloch 1967, Suzuki and Dulk 1985b].

The peak visibility of the burst as observed with the long baseline interferometer at 53 MHz (see Figure 3.25) is ≈ 0.1. This indicates that the burst source has been resolved significantly by the interferometer.

A model fitting analysis was performed to estimate the source size that could give rise to the above visibility. For this, Gaussian source models of various widths were convolved with the response of the interferometer. The results indicate that a source size of $\approx 15''$ would result in the estimated

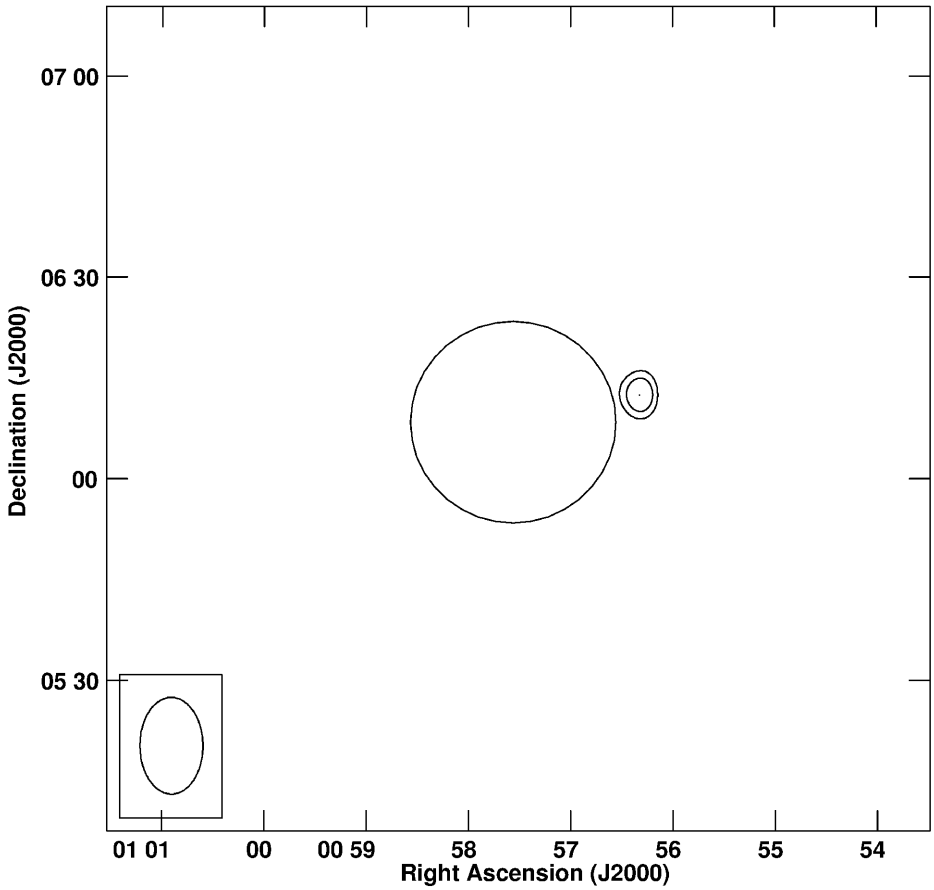

Figure 3.27: Heliograph map of the source region.

visibility. This is consistent with the results of our previous similar long baseline interferometer observations, but on a ≈ 8 km baseline, in which we have shown that compact radio sources with angular size $\lesssim 1'$ could exist in regions of the corona from where 38 MHz radio emission originates [Mugundhan et al. 2016].

The above source size in the present case represents most likely the width of the electron beam that generated the type IIIb burst. The fact that coronal loop structures of angular size $\sim 20''$ can be noticed upto heliocentric distance $r \approx 2.0\ R_\odot$ in the eclipse and coronagraph pictures of the solar corona confirms this (see for example Gergely [1986]).

Based on ray tracing calculations in a spherically symmetric coronal density model (including density inhomogenities and a coronal streamer)

at a typical frequency like 80 MHz, Riddle [1974] had shown that compact radio sources of angular size $\lesssim 30''$ could be observed, particularly in the case of harmonic emission from transient type III solar radio bursts.

Sources close to the solar limb are expected to be broadened than those on the solar disk. McConnell [1983] had presented evidence for the presence of even smaller scale ($\approx 3''$) structures in the solar corona from where the low frequency radio radiation originates. Subramanian and Cairns [2011] had reported source sizes $< 10''$.

The recent results on density turbulence in the solar corona from low frequency observations are also in reasonable support of the above findings [SasikumarRaja et al. 2016, 2017, Mugundhan et al. 2017].

An inspection of the images obtained with the SOHO LASCO C2 coronograph on 2017 April 5 indicates that there was a coronal streamer near the burst source in the present case, as mentioned in Riddle [1974]. Considering all these, the present results clearly indicate that small-sized discrete radio sources are observable in the corona at low frequencies provided the observing instruments have adequate angular resolution. We also speculate that the estimated burst size of 15″ could be an angular broadened version due to scattering and refraction effects, and the size could have been smaller if the location of the burst had been near the center of the solar disk.

3.5 Summary

In this chapter, results from our LBI experiments targeted at detecting the smallest angular structure on the Sun was presented. We recapitulated the basics of radio interferometry and compared the difference between connected element and long baseline interferometry. Due to the special requirements of LBI, we developed a low cost data recording system in the observatory, which can record raw samples without loss upto bandwidths of $\approx$ 32 MHz. We validated the working of the data recorder system, both through lab and field tests. This also shows that for observing strong sources over moderately long baselines just an oscillator linked to GPS may serve as a simple low cost alternative to atomic clocks. After validating the recorders, we began our scientific campaign on our target source Sun.

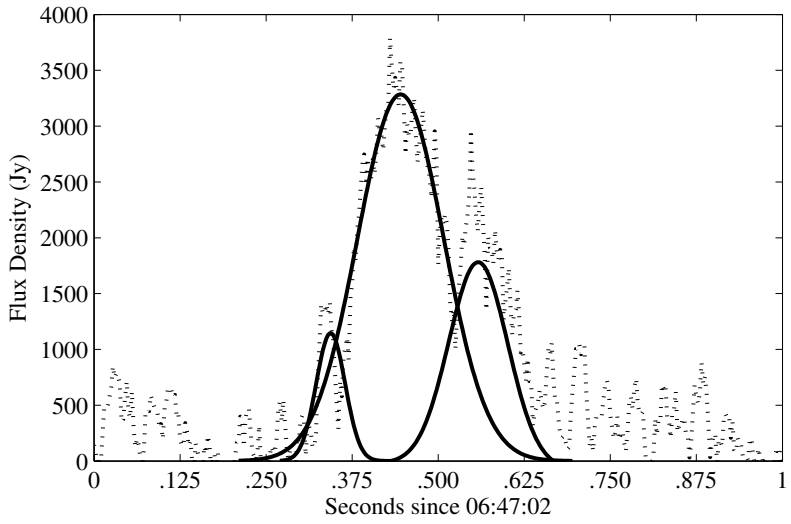

Figure 3.28: Gaussian fits to the observed correlated-intensity profile shown in Figure 3.25. The "solid" lines are the Gaussian fit to the data. The time interval between the maxima of the bursts are $\approx$ 125 ms

The importance of this experiment lies in the fact that such experiments have not been attempted on the sun as theoretical predictions estimate that even sources of small size would get angular broadened in the solar corona, due to density fluctuations. But there have been observational, and numerical studies, which have shown otherwise. The fact that we have been able to detect sources as small as $\approx$ 15" indicate that these structures should be, in principle, observable with future, high dynamic range, high resolution instruments like the MWA, the SKA, and the LOFAR. From the Gauribidanur viewpoint, the experiment has answered the question, it was designed to probe: structures $\sim$ 1′ exist in the solar corona, and thus expansion of the longest baseline upto 10 km, is indeed feasible and would allow us to regularly image the sun in high resolutions.

References

Aubier, M., Leblanc, Y., and Boischot, A. (1971). Observations of the Quiet Sun at Decameter Wavelengths - Effects of Scattering on the Brightness Distribution. *Astron. Astrophys.*, 12:435.

Bastian, T. S. (1994). Angular scattering of solar radio emission by coronal turbulence. *Astrophys. J.*, 426:774–781.

Bastian, T. S. (2004). Low-frequency solar radiophysics with LOFAR and FASR. , 52:1381–1389.

Benz, A. O. (1995a). Flares and Coronal Heating in the Sun and Stars. In Benz, A. O. and Krüger, A., editors, *Coronal Magnetic Energy Releases*, volume 444 of *Lecture Notes in Physics, Berlin Springer Verlag*, page 1.

Benz, A. O. (1995b). Flares and Coronal Heating in the Sun and Stars. In *Coronal Magnetic Energy Releases*, volume 444 of *Lecture Notes in Physics (Berlin: Springer-Verlag)*, page 1.

Benz, A. O. and Wentzel, D. G. (1981). Coronal evolution and solar type I radio bursts - an ion-acoustic wave model. *Astron. Astrophys.*, 94:100–108.

Booth, R. S. (1991). The European VLBI network. *Advances in Space Research*, 11:397–401.

Carrel, R. (1966). The design of log-periodic dipole antennas. In *1958 IRE International Convention Record*, volume 9, pages 61–75. IEEE.

Christiansen, W. N. and Högbom, J. A. (1987). *Radiotelescopes*. CUP Archive.

Clivati, C., Ambrosini, R., Artz, T., Bertarini, A., Bortolotti, C., Frittelli, M., Levi, F., Mura, A., Maccaferri, G., Nanni, M., Negusini, M., Perini, F., Roma, M., Stagni, M., Zucco, M., and Calonico, D. (2017). A VLBI experiment using a remote atomic clock via a coherent fibre link. *Scientific Reports*, 7:40992.

Dewdney, P. E., Hall, P. J., Schilizzi, R. T., and Lazio, T. J. L. (2009). The square kilometre array. *Proceedings of the IEEE*, 97(8):1482–1496.

Dulk, G. A. and Sheridan, K. V. (1974). The Structure of the Middle Corona from Observations at 80 and 160 MHz. *Solar Phys.*, 36:191–202.

Elgarøy, E. Ø. (1977). *Solar noise storms.*

Ellingson, S. W., Clarke, T. E., Cohen, A., Craig, J., Kassim, N. E., Pihlstrom, Y., Rickard, L. J., and Taylor, G. B. (2009). The long wavelength array. *Proceedings of the IEEE*, 97(8):1421–1430.

Ellis, G. R. A. and McCulloch, P. M. (1967). Frequency splitting of solar radio bursts. *Aust. J. Phys.*, 20:583.

Erickson, W. C. (1964). The Radio-Wave Scattering Properties of the Solar Corona. *Astrophys. J.*, 139:1290.

Erickson, W. C., Kundu, M. R., Mahoney, M. J., and Gergely, T. E. (1977). Determination of the decameter wavelength spectrum of the quiet sun. *Solar Phys.*, 54:57–63.

Gergely, T. E. (1986). Lower limits of solar burst source sizes at decameter wavelengths. In Erickson, W. C. and Cane, H. V., editors, *Low Frequency Radio Astronomy*, volume 10 of *Proceedings of NRAO Workshop (West Virginia: National Radio Astronomy Observatory)*, page 97.

Hariharan, K., Ramesh, R., Kathiravan, C., Abhilash, H. N., and Rajalingam, M. (2016). High Dynamic Range Observations of Solar Coronal Transients at Low Radio Frequencies with a Spectro-correlator. *Astrophys. J. Suppl.*, 222:21.

Hudson, H. S. (1991). Solar flares, microflares, nanoflares, and coronal heating. *Solar Phys.*, 133:357–369.

Jacobson, A. R., Massey, R. S., and Erickson, W. C. (1991). A study of transionospheric

refraction of radio waves using the Clark Lake Radio Observatory. *Annales Geophysicae*, 9:546–552.

Kai, K., Melrose, D. B., and Suzuki, S. (1985). *Storms*, pages 415–441.

Kassim, N., Perley, R. A., Carilli, C. L., Harris, D. E., and Erickson, W. C. (1996). *Low Frequency Observations of Cygnus A*, page 182.

Kassim, N. E., Lazio, T. J. W., Erickson, W. C., Perley, R. A., Cotton, W. D., Greisen, E. W., Cohen, A. S., Hicks, B., Schmitt, H. R., and Katz, D. (2007). The 74 MHz System on the Very Large Array. *Astrophys. J. Suppl.*, 172:686–719.

Kathiravan, C., Ramesh, R., Barve, I. V., and Rajalingam, M. (2011). Radio Observations of the Solar Corona During an Eclipse. *Astrophys. J.*, 730:91.

Kathiravan, C., Ramesh, R., and Subramanian, K. R. (2002). Metric Radio Observations and Ray-tracing Analysis of the Onset Phase of a Solar Eruptive Event. *Astrophys. J. Lett.*, 567:L93–L95.

Kerdraon, A. and Delouis, J.-M. (1997). The Nançay Radioheliograph. In Trottet, G., editor, *Coronal Physics from Radio and Space Observations*, volume 483 of *Lecture Notes in Physics, Berlin Springer Verlag*, page 192.

Kishore, P., Ramesh, R., Kathiravan, C., and Rajalingam, M. (2015). A Low-Frequency Radio Spectropolarimeter for Observations of the Solar Corona. *Solar Phys.*, 290:2409–2422.

Kraus, J. D. (1966). *Radio astronomy*.

Krucker, S. and Benz, A. O. (1998). Energy Distribution of Heating Processes in the Quiet Solar Corona. *Astrophys. J. Lett.*, 501:L213–L216.

Kundu, M. R., Erickson, W. C., Gergely, T. E., Mahoney, M. J., and Turner, P. J. (1983). First results from the Clark Lake Multifrequency Radioheliograph. *Solar Phys.*, 83:385–389.

Kundu, M. R. and Gopalswamy, N. (1990). Filament eruption and storm radiation at meter-decameter wavelengths. *Solar Phys.*, 129:133–152.

Labrum, N. R. (1972). The Culgoora Solar Radio Observatory. *Solar Phys.*, 27:496–504.

Lang, K. R. and Willson, R. F. (1987). VLA observations of a solar noise storm. *Astrophys. J.*, 319:514–519.

Malik, R. K. and Mercier, C. (1996). Motions, Relative Positions, and Sizes of Continua and Bursts in Solar Noise Storms. *Solar Phys.*, 165:347–375.

McConnell, D. (1983). Evidence for arc sec radio burst sources in the upper corona. *Solar Phys.*, 84:361.

Mercier, C. and Chambe, G. (2009). High Dynamic Range Images of the Solar Corona Between 150 and 450 MHz. *Astrophys. J. Lett.*, 700:L137–L140.

Mercier, C., Subramanian, P., Chambe, G., and Janardhan, P. (2015). The structure of solar radio noise storms. *Astron. Astrophys.*, 576:A136.

Mercier, C., Subramanian, P., Kerdraon, A., Pick, M., Ananthakrishnan, S., and Janardhan, P. (2006). Combining visibilities from the giant meterwave radio telescope and the Nancay radio heliograph. High dynamic range snapshot images of the solar corona at 327 MHz. *Astron. Astrophys.*, 447:1189–1201.

Mercier, C. and Trottet, G. (1997). Coronal Radio Bursts: A Signature of Nanoflares? *Astrophys. J. Lett.*, 474:L65–L68.

Monstein, C., Ramesh, R., and Kathiravan, C. (2007). Radio spectrum measurements at the Gauribidanur observatory. *Bulletin of the Astronomical Society of India*, 35:473–480.

Mugundhan, V., Hariharan, K., and Ramesh, R. (2017). Solar type iiib radio bursts as tracers for electron density fluctuations in the corona. *Solar Phys.*, 291:155.

Mugundhan, V., Ramesh, R., Barve, I. V., Kathiravan, C., Gireesh, G. V. S., Kharb, P., and Misra, A. (2016). Low-Frequency Radio Observations of the Solar Corona with Arcminute Angular Resolution: Implications for Coronal Turbulence and Weak Energy Releases. *Astrophys. J.*, 831:154.

Napier, P. J. (1994). The Very Long Baseline Array [invited]. In Robertson, J. G. and Tango, W. J., editors, *Very High Angular Resolution Imaging*, volume 158 of *IAU Symposium*, page 117.

Nelson, G. J., Sheridan, K. V., and Suzuki, S. (1985). *Measurements of solar flux density and polarization*, pages 113–154.

Oberoi, D., Matthews, L. D., Cairns, I. H., Emrich, D., Lobzin, V., et al. (2011). First spectroscopic imaging observations of the sun at low radio frequencies with the murchison widefield array prototype. *Astrophys. J. Lett.*, 728:L27.

Parnell, C. E. and Jupp, P. E. (2000). Statistical Analysis of the Energy Distribution of Nanoflares in the Quiet Sun. *Astrophys. J.*, 529:554–569.

Porter, J. G., Fontenla, J. M., and Simnett, G. M. (1995). Simultaneous ultraviolet and X-ray observations of solar microflares. *Astrophys. J.*, 438:472–479.

Prasad, T. R., Patra, A., Anandan, V., and Satyanarayana, P. (2016). Employment of new techniques for characterizing indian mst radar phased array. *IETE Technical Review*, 33(6):584–595.

Ramesh, R. (2000). Low Frequency Radio Emission from the 'Quiet Sun'. *Journal of Astrophysics and Astronomy*, 21:237.

Ramesh, R. (2011). Low frequency solar radio astronomy at the Indian Institute of Astrophysics (IIA). In *Astronomical Society of India Conference Series*, volume 2 of *Astronomical Society of India Conference Series*.

Ramesh, R. and Ebenezer, E. (2001). Decameter Wavelength Observations of an Absorption Burst from the Sun and Its Association with an X2.0/3B Flare and the Onset of a "Halo" Coronal Mass Ejection. *Astrophys. J. Lett.*, 558:L141–L143.

Ramesh, R., Kathiravan, C., Barve, I. V., Beeharry, G. K., and Rajasekara, G. N. (2010a). Radio Observations of Weak Energy Releases in the Solar Corona. *Astrophys. J. Lett.*, 719:L41–L44.

Ramesh, R., Kathiravan, C., Barve, I. V., and Rajalingam, M. (2012). High Angular Resolution Radio Observations of a Coronal Mass Ejection Source Region at Low Frequencies during a Solar Eclipse. *Astrophys. J.*, 744:165.

Ramesh, R., Kathiravan, C., Indrajit V. Barve, Beeharry, G. K., and Rajasekara, G. N. (2010b). Radio observations of weak energy releases in the solar corona. *Astrophys. J. Lett.*, 719:L41.

Ramesh, R., Kathiravan, C., and Narayanan, A. S. (2011). Low-frequency Observations of Polarized Emission from Long-lived Non-thermal Radio Sources in the Solar Corona. *Astrophys. J.*, 734:39.

Ramesh, R., Nataraj, H. S., Kathiravan, C., and Sastry, C. V. (2006). The Equatorial Background Solar Corona during Solar Minimum. *Astrophys. J.*, 648:707–711.

Ramesh, R., Sasikumar Raja, K., Kathiravan, C., and Satya Narayanan, A. (2013). Low-frequency radio observations of picoflare category energy releases in the solar atmosphere. *Astrophys. J.*, 762:89.

Ramesh, R., Subramanian, K. R., Sundararajan, M. S., and Sastry, C. V. (1998). The Gauribidanur Radioheliograph. *Solar Phys.*, 181:439–453.

Rao, P., Jain, A., Kishore, P., Balamuralidhar, P., Damle, S., and Viswanathan, G. (1995). Indian mst radar 1. system description and sample vector wind measurements in st mode. *Radio Science*, 30(4):1125–1138.

Riddle, A. C. (1974). On the Observation of Scattered Radio Emission from Sources in the Solar Corona. *Solar Phys.*, 35:153.

Sasikumar Raja, K., Ramesh, R., Hariharan, K., Kathiravan, C., and Wang, T. J. (2014). An Estimate of the Magnetic Field Strength Associated with a Solar Coronal Mass Ejection from Low Frequency Radio Observations. *Astrophys. J.*, 796:56.

SasikumarRaja, K., Ingale, M., Ramesh, R., Subramanian, P., Manoharan, P. K., and Janardhan, P. (2016). Amplitude of solar wind density turbulence from 10 to 45 $r_{\odot}$. *J. Geophys. Res.: Space Physics*, 121:11605.

SasikumarRaja, K., Subramanian, P., Ramesh, R., Vourlidas, A., and Ingale, M. (2017). Turbulent density fluctuations and proton heating rate in the solar wind from 9 to 20 $r_{\odot}$. *Astrophys. J.*, 850:129.

Sastry, C. V. (1994). Observations of the continuum radio emission from the undisturbed Sun at a wavelength of 8.7 meters. *Solar Phys.*, 150:285–294.

Steinberg, J. L., Caroubalos, C., and Bougeret, J. L. (1974). STEREO-1 measurements of the beam pattern of 169 MHz type I bursts on November 18, 1971. *Astron. Astrophys.*, 37:109–115.

Subramanian, K. R., Gopalswamy, N., and Sastry, C. V. (1993). A new investigation of microbursts at meter-decameter wavelengths. *Solar Phys.*, 143:301–316.

Subramanian, P. and Becker, P. A. (2004). Noise-Storm Continua: Power Estimates for Electron Acceleration. *Solar Phys.*, 225:91–103.

Subramanian, P. and Cairns, I. (2011). Constraints on coronal turbulence models from source sizes of noise storms at 327 MHz. *Journal of Geophysical Research (Space Physics)*, 116:A03104.

Suresh, A., Sharma, R., Oberoi, D., Das, S. B., Pankratius, V., et al. (2017). Low-frequency radio observations of picoflare category energy releases in the solar atmosphere. *Astrophys. J.*, 843:19.

Suzuki, S. and Dulk, G. A. (1985a). *Bursts of Type III and Type V*, pages 289–332.

Suzuki, S. and Dulk, G. A. (1985b). Bursts of Type III and Type V. In McLean, D. J. and Labrum, N. R., editors, *Solar Radiophysics (Cambridge: Cambridge University Press)*, page 289.

Thejappa, G. (1991). A self-consistent model for the storm radio emission from the sun. *Solar Phys.*, 132:173–193.

Thompson, A. R., Moran, J. M., and Swenson, Jr., G. W. (2017). *Interferometry and Synthesis*

in Radio Astronomy, 3rd Edition.

Tingay, S., Goeke, R., Bowman, J. D., Emrich, D., Ord, S., Mitchell, D. A., Morales, M. F., Booler, T., Crosse, B., Wayth, R., et al. (2013). The murchison widefield array: The square kilometre array precursor at low radio frequencies. *Publications of the Astronomical Society of Australia*, 30.

Van Haarlem, M., Wise, M., Gunst, A., Heald, G., McKean, J., Hessels, J., De Bruyn, A., Nijboer, R., Swinbank, J., Fallows, R., et al. (2013). Lofar: The low-frequency array. *Astronomy & astrophysics*, 556:A2.

Wild, J. P. (1967). The radioheliograph and the radio astronomy programme of the Culgoora Observatory. *Proceedings of the Astronomical Society of Australia*, 1:38.

Chapter 4

High Resolution Solar Spectral Observations

This Chapter is based on Mugundhan V., Hariharan K., Ramesh R., 2017, Solar Physics, 292, 155

4.1 Introduction

Ground based spectroscopic observations of the Sun has been carried out with great success since 1960s covering the whole of Radio Frequency Spectrum from a few MHz to a few GHz. These observations have yielded a wealth of information ranging from distribution of electrons, their propagation, and magnetic fields in the solar corona.

As discussed in the first chapter, radiation at different frequencies originate from different height ranges in the solar corona. Observations of the morphology of solar bursts in the time-frequency image of the burst, the so called dynamic spectrum, tells us the history of the radio burst.

These bursts are observed with instruments called spectrographs, which is an antenna system connected to a spectrometer, that measures power at different frequencies. Conventionally, the spectrometer at the backend of such spectrograph systems have been swept frequency spectrum analyzers. But these are not suitable for observing the characteristics of bursts at high time and spectral resolution. This calls for design of specetrometers with suitable time and frequency resolution, and interfaces for transfer of

high resolution data, which will be discussed in this chapter.

The chapter is organized as follows: The existing spectrograph at Gauribidanur which observes the Sun is discussed initially, with emphasis on the back-end. Then preliminary trial runs using a burst mode spectrometer as the back-end receiver for GLOSS is discussed. Based on the obtained preliminary results from the former, a continuous acquisition FPGA based spectrometer was developed. This system and high resolution observations obtained with it is presented. Using the observations, a new technique to estimate the coronal electron density fluctuations in the low corona is proposed.

4.2 Gauribidanur Low Frequency Solar Spectrograph

The Gauribidanur Low Frequency Spectrograph (GLOSS) was commissioned to observe the solar corona in the frequency range of $40-440$ MHz, which generally corresponds to a heliocentric distance range of $1.5-2R_{\odot}$ [Kishore et al. 2014]. GLOSS is a phased array of eight Log Periodic Dipole Antennas (LPDA) in the North-South (NS) direction, with their E-plane along the East-West (EW). The above arrangement synthesizes a beam that is highly directive in the NS($\approx 3°$), but is broad in the EW($\approx 60°$). This broad EW beam ensures that the Sun is in the Field of View of the array for atleast 8 hours a day. The directive NS beam has to be phased to track the Sun along the declination, as it traverses between ± 23°over an year. The RF signals from the individual antennas are amplified and are coherently combined in an analog beam-former, which uses delay shifting to achieve a wideband performance. The tilt angle resolution is $\approx 3°$. More details on the design, characterization, and validation of the analog beam-former is available in Mugundhan [2014].

The beamformed signal is amplified by $\approx$ 30dB once more before being transmitted to the lab for data acquisition and processing. At the Lab, the signal is passed through an notch filter to attenuate strong out of band FM signals. The Data Acquisition is performed in a commercially available

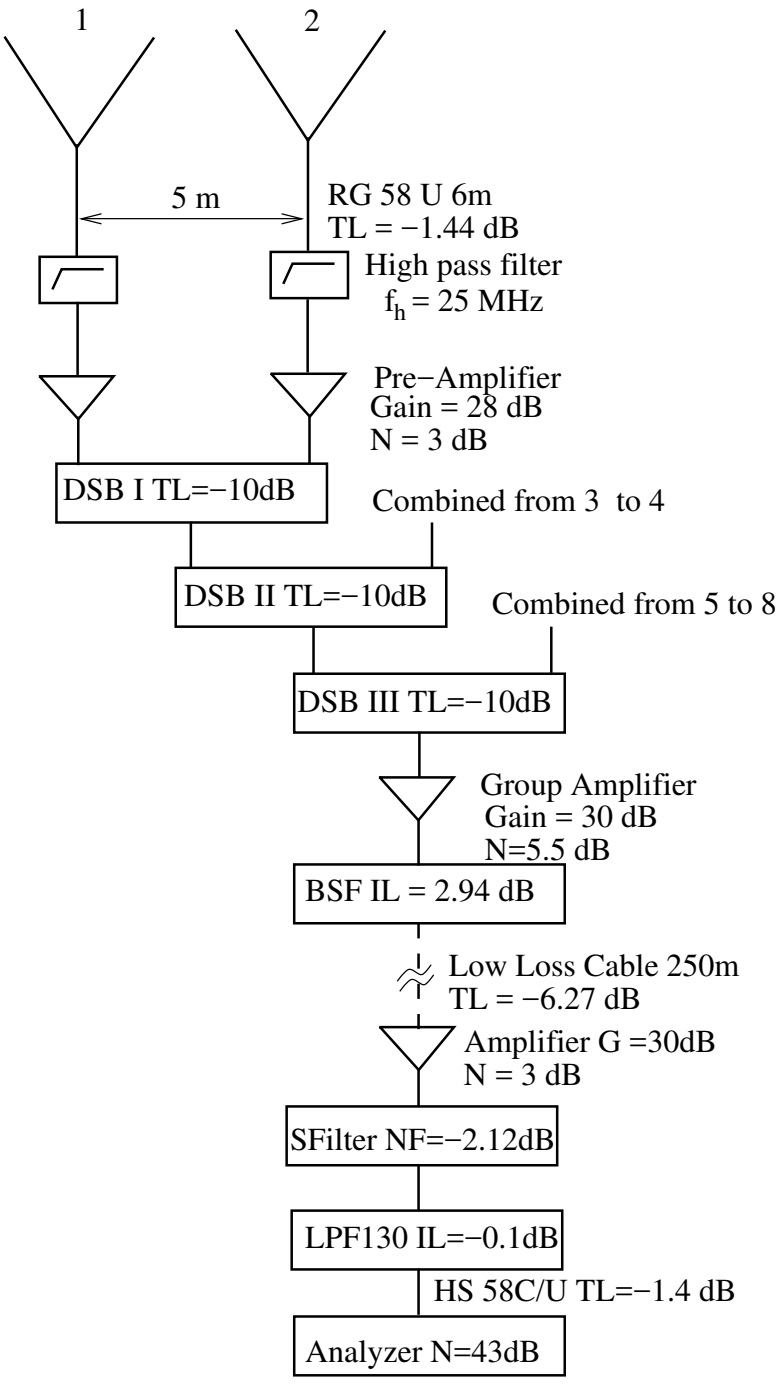

Figure 4.1: Block Diagram of GLOSS, from Kishore [2016]

Agilent E4401B[1] Spectrum analyzer. The Block diagram of the Spectrum Analyzer is shown in Figure 4.2. The E4401B works in a frequency range of 9 kHz to 1.5 GHz, with programmable frequency ranges and outputs 401 spectral points per sweep.

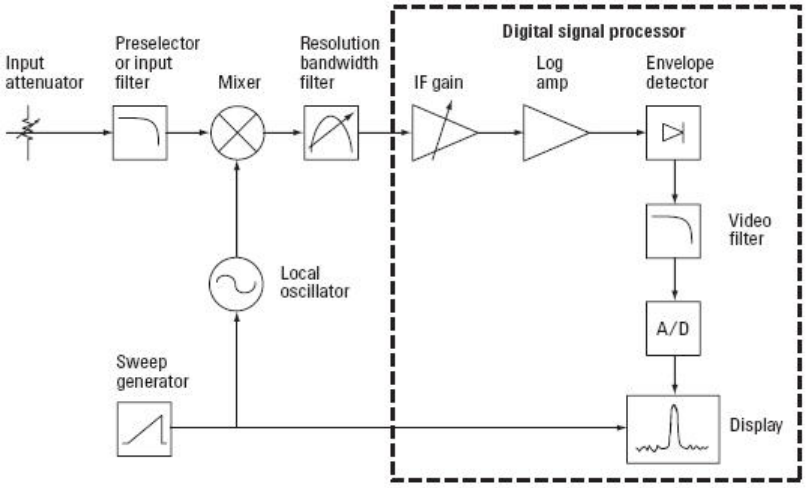

Figure 4.2: Spectrum Analyzer Block Diagram (Image Courtesy: `http://rfmw.em.keysight.com/spectrum-analyzer/`)

At the heart of the spectrum analyzer is a superheterodyne receiver, which consists of a mixer that converts the RF input to a fixed frequency IF output. To keep the IF frequency fixed for any RF frequency, the LO signal has to be swept across a range of frequencies. The time taken for a complete sweep of the LO from its lowest to the highest value, such that the correct RF signal is converted to IF, is called the *sweep time* of the spectrum analyzer. Larger the RF band to be analyzed, larger the sweep time. The amount of time that the spectrum analyzer stays at a single frequency is called the *dwell time*. Two other important parameters are *resolution bandwidth*(RBW) and *video bandwidth*(VBW). The former is the bandwidth of the IF filter at the mixer output, while the latter is the bandwidth of the lowpass filter at the output of the power law detector. The Spectrum analyzer, in the

[1] `http://literature.cdn.keysight.com/litweb/pdf/5966-0676E.pdf?id=1000031886:epsg:dow`

case of GLOSS, is interfaced to a Data Acquisition Server through General Purpose Interface Bus (GPIB). The aforementioned parameters are user configurable through a Visual C++ program. The true sweep time of the spectrum analyzer is ≈ 4 ms, which implies the time spent at every frequency is ≈ 10μs. Ten such spectra are averaged as a single spectrum sample and transferred to the acquisition PC. During the time of data transfer, the spectrum analyzer suspends spectrum measurement. The time resolution of the instrument is ≈ 256 ms, in which ≈ 216 ms is the time for data transfer, which is also the dead-time.

This would adversely affect the Signal to Noise Ratio (SNR) of the instrument, which is an important Figure of Merit. The minimum detectable flux of any radio telescope is defined as

$$\Delta S_{min} = \frac{2k_b T_{sys}}{A_e \sqrt{\beta \tau}} \tag{4.1}$$

where k_b is the Boltzmann's constant, T_{sys} is the system temperature, A_e is the effective Aperture area, β and τ are the frequency and time resolutions, respectively. For a swept frequency system like GLOSS, we can define *duty cycle* d as $\frac{t_{on}}{t_{on}+t_{off}}$, where t_{on} and t_{off} are on- and off-source times. If we substitute t_{on} as τ in terms of d, then Equation 4.1 becomes

$$\Delta S_{min} = \frac{2k_b T_{sys}}{A_e \sqrt{\beta d (t_{on} + t_{off})}} \tag{4.2}$$

For GLOSS, the $t_{on} + t_{off}$) is 256 ms, and d=0.03%. This would result in an increase of ΔS_{min} by ≈ 50 times, resulting in a similar loss of SNR. This problem can be alleviated by using a *Fast Fourier Transform* (FFT) spectrometer.

4.3 Fast Fourier Transform Spectrometer (FFTS)

4.3.1 Fast Fourier Transform and Polyphase Filtering

Fourier Transform is an operation used to decompose a time domain signal into its constituent frequencies. The Fourier Transform of a time domain signal $x(t)$ is defined as:

$$X[\omega] = \int_{-\infty}^{+\infty} x(t)e^{-j\omega t}dt, \tag{4.3}$$

where ω is the angular frequency.

In a practical application, the limits of integration may be a finite time interval. Fourier Transform can be visualized as passing an input signal simultaneously to a number of bandpass filters with different center frequencies. In most cases, such an implementation is not feasible, due to which the transform is performed over a digitized version of the original signal by sampling the latter at Nyquist Rate. The Fourier Transform of a discrete time sequence $x[n]$, also called a DFT is:

$$X[k] = \Sigma_0^N x[n]e^{-j\omega n}, \tag{4.4}$$

where k is the frequency index, N is the total number of samples to be operated up-on. For a time domain signal sampled at a rate of f_s, the $k = 0^{th}$ and $k = N^{th}$ index contain the strength of the signals at frequencies $f = -f_s/2$ and $f = +f_s/2$, respectively. The Fourier transform is periodic over every 2π radians. The various properties of Fourier transform can be found in any standard Digital Signal Processing textbooks (Bracewell and Bracewell [1986], Proakis and Manolakis [1996] and references therein). An important aspect of the DFT to be noted here is that every single $X[k]$ has contribution from all the N input samples used to compute it. Thus, the FFT outputs the frequency information of the signal at all frequency channels "simultaneously". A DFT has $O(N^2)$ multiplications and additions. This implies for DFTs of larger N, there will be a quadratic increase in the number of multiplications.

An algorithm to carry-out the DFT with much lesser number of multiply operation was proposed by Cooley and Tuckey [Cooley and Tukey 1965]. The algorithm exploited the conjugate symmetry[2] and periodicity[3] properties of the DFT and reduced the number of multiplications to $O((N/2)\log_2(N))$.

FIR filters are a class of digital filters, whose response to an impulse function are of a finite duration. This property ensures that the response

[2] $e^{\frac{-j2\pi(k+N/2)}{N}} = -e^{\frac{-j2\pi k}{N}}$

[3] $e^{\frac{-j2\pi(k+N)}{N}} = e^{\frac{-j2\pi k}{N}}$

sequence tends to zero after N/2 samples, where N is the filter order.

The transfer function of a linear time invariant FIR filter in z-transform domain is given as:

$$H(z) = b_0 + b_1 z^{-1} + b_2 z^{-2} + ..., \tag{4.5}$$

where b_0, b_1, b_2 etc., are filter coefficients. These filter coefficients are designed based on the desired response of the filter. Using block diagrams, the FIR filter can be represented as shown in the Figure 4.13.

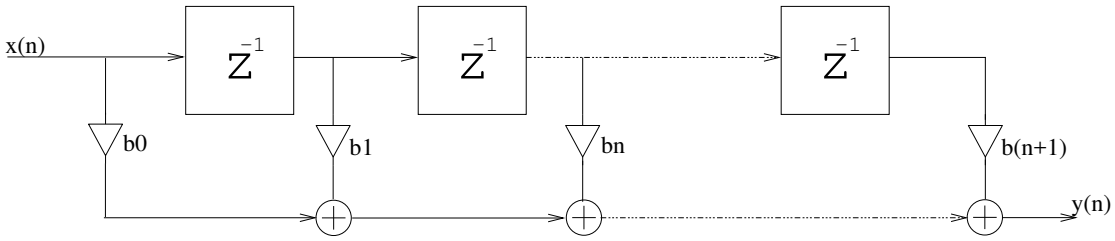

Figure 4.3: Direct form implementation of a FIR filter

From the above equation, we see that an FIR filter is a windowed moving average of the sequence x(n). For efficient usage of computational resources, the filter structure can be re-arranged as shown in Figure 4.14. Here we see that the filter coefficients are split into three sections, and each section can operate at 1/3 the original speed. Also, the filter coefficients can be chosen in such a way that the pass band can be shaped. This is called a polyphase filter.

Both these algorithms can be easily implemented in modern-day computing devices such as Micro-processors, FPGAs, *etc.*.

The FFTS described in the subsequent sections implements the spectrometer on an FPGA. The advantage of using FPGAs over traditional computing devices are their concurrency and low-power. Modern day FPGAs like those of the Virtex 5 Family have on-board high speed tranceivers, and digital signal processing (DSP) resources that can be used to interface ADCs and carry out compute intensive signal processing operations.

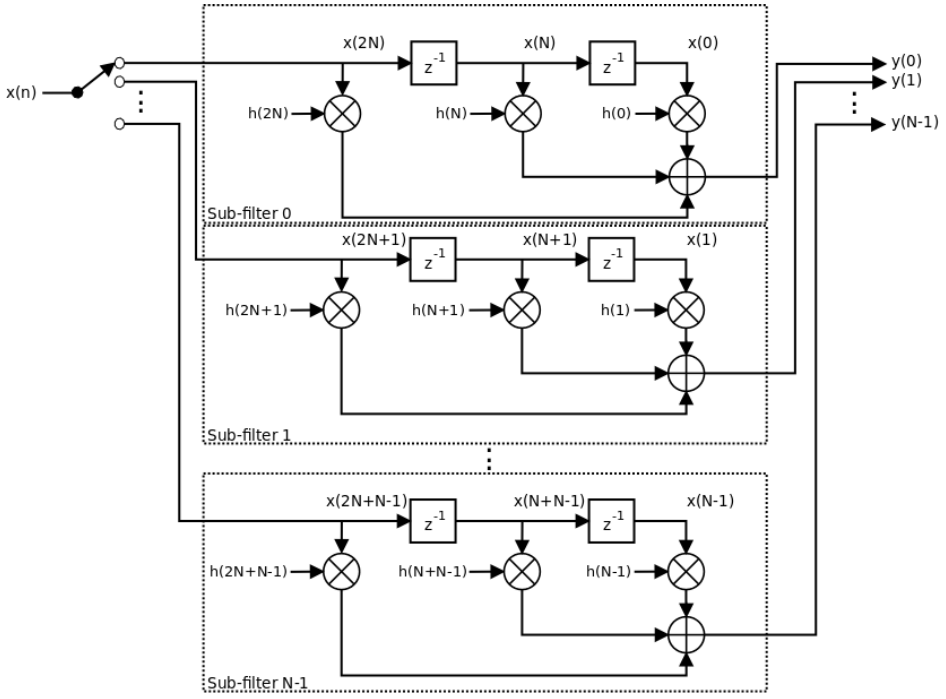

Figure 4.4: Polyphase filter implementation (Image Courtesy: `https://casper.berkeley.edu/wiki/The_Polyphase_Filter_Bank_Technique`)

4.4 AD9286 Data Capture Board Prototype[4]

An initial prototype of the FFTS was built on an Analog Devices AD9286 ADC evaluation board coupled to a data capture board, HSC-ADC-EVALCZ (EVALCZ). Refer Chapter 2 and Chapter 3 on more details about the ADC and its characterization. The EVALCZ consists of a Virtex-4 family FPGA, whose primary task is to capture the digitized samples and transfer them to a computer via Universal Serial Bus (USB). The ADC is interfaced to EVALCZ via [5] high density connectors. Serial Programming of the ADC to control dc offset, V_{ref} etc. were implemented using an SPI control software provided by the manufacturer.

[4]Section 4.4 and 4.5 are covered in detail in the thesis *Solar Radio Observations at Low Frequencies with High Spectral and Temporal Resolutions* by K. Hariharan. Here it is recapitulated for the sake of completeness.

[5]`http://catalog.tycoelectronics.com/TE/GeneralInfo/electrical_performance.pdf`

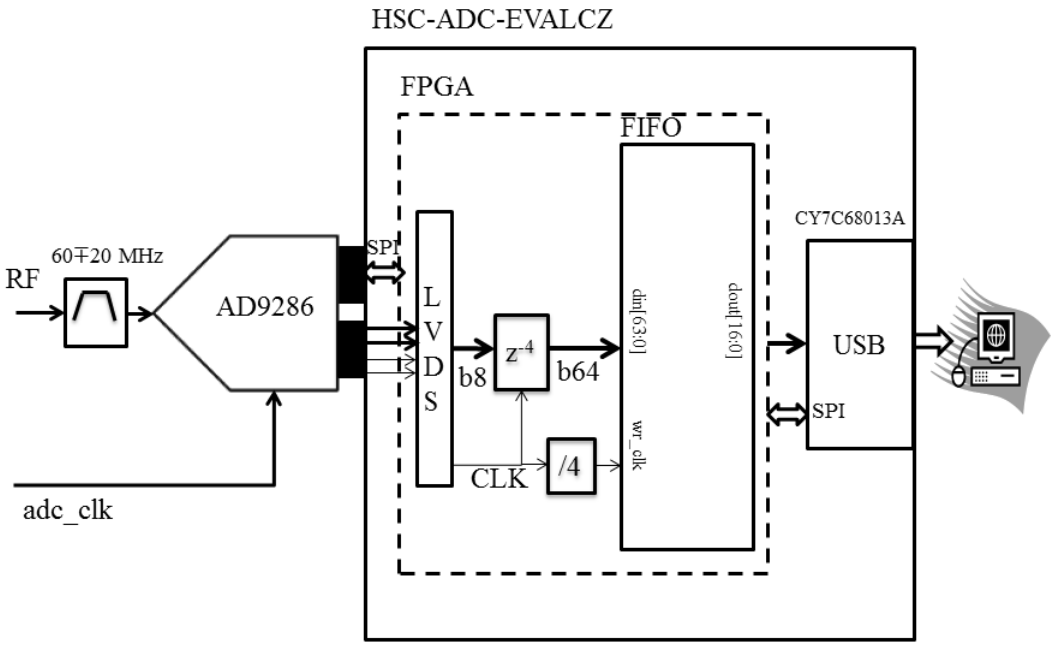

Figure 4.5: AD9286 Data Capture Board Prototype Spectrometer – Block Diagram

The Spectrometer block diagram is shown in Figure 4.5. The data is sampled using an external clock at 200 MHz. The sampled data is transmitted to the FPGA as Low Voltage Differential (LVDS) signals, as parallel bits. These signals are received on the FPGA using differential input buffers (IBUFDS instances) and are formed as 16 bit words (2× 8 bit samples). To make the data source synchronous, the sampling clock is also transmitted along with the data. The sampling clock acts as the reference to a Digital Clock Manager (DCM) module, from which an in-phase and divided-by-4 (`div4`) version of the sampling clock is output. The in-phase output is used to resample the formed 16 bit words. The 16 bit words are pipelined and concatenated as 64 bit words. The 64 bit words act as the input to the FIFO, whose write clock is the `DIV4` output of the DCM module. The FIFO is read out on the assertion of `rden` signal and the output words are transmitted

to the USB peripheral controller, CY7C68013A. This IC acts as the interface between the PC and the FPGA.

The captured data is visualized on PC using a *Visual Analog*(VA) software. VA is a Graphical User Interface (GUI) based software, where library components can be placed according to the analysis to be performed. For the application described here, a FFT component was used. The length of the FFT was 4096, out of which only one half of the spectrum is saved to an `ascii` file. The frequency resolution is $\approx$ 49 kHz. The `ascii` file was later converted to a binary file to reduce storage space. Solar observations were carried out using this backend, which is described in the next section.

4.5 Preliminary Observations in Burst Mode

During the period of February – April, 2014, observations using the aforementioned backend, simultaneously with the commercial spectrum analyzer backend. The Figure 4.6 shows the dynamic spectrum of a Type III burst observed with the GLOSS Spectrum analyzer backend in the top panel, and the Data-capture-board backend in the bottom panel. The time profile of the events at typical frequencies like 53 MHz, and 80 MHz is plotted on Figure 4.6.

On close inspection of the dynamic spectrum, we see that the bottom panel appears more pixelated due to the lack of enough spectral points, while the dynamic spectrum in the top panel has shows the event with a better contrast. The improvement in SNR was approximately 2 times was measured. This was attributed to the fact that source was observed simultaneously at all frequencies using the EVAL-CZ spectrometer, but observing in continuous mode was not possible because: The evaluation board used for this experiment, was provided by analog devices, exclusively for evaluating the capture performance of the FPGA, and the analysis was performed on PC using visual analog, which placed an upper limit on the maximum data that can be processed, along with USB 2.0 link, which proved to be a bottleneck, when trying to transfer data at higher speed. Thus it was decided to develop a system, where continuous acquisition and spectral analysis can be carried out real time, with also capability to transfer data at high speed.

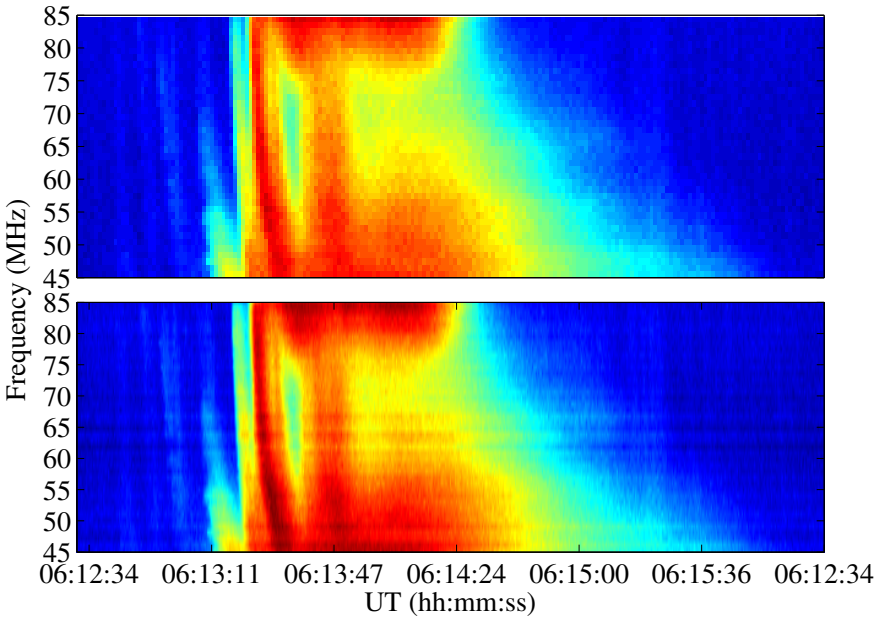

Figure 4.6: A Type III burst observed using the GLOSS EVAL-CZ burst mode backend (Top panel) and the conventional Spectrum Analyzer backend (Bottom Panel)

4.6 XUPV5-AD9286 Spectrometer

Based on the success of the spectrometer described in the previous section, it was sought design a spectrometer where the dead-time would be alleviated. For this it was decided to perform the FFT on-board the FPGA itself, rather than transferring the data to a PC and performing the transform there. For this, the same FPGA and ADC system that was used for the VLBI observations was utilized. The complete system setup is shown in figure 4.7.

The Virtex 5 FPGA onboard the XUPV5 was capable of performing mid-range DSP operations with through embedded DSP48E slices, and had options for high speed data transfer in the form of Gbe and PCIe. The FPGA is a completely configurable device, and the specific function of the FPGA is decided by the firmware with which the FPGA is programmed.

The main design goals for the firmware design were:

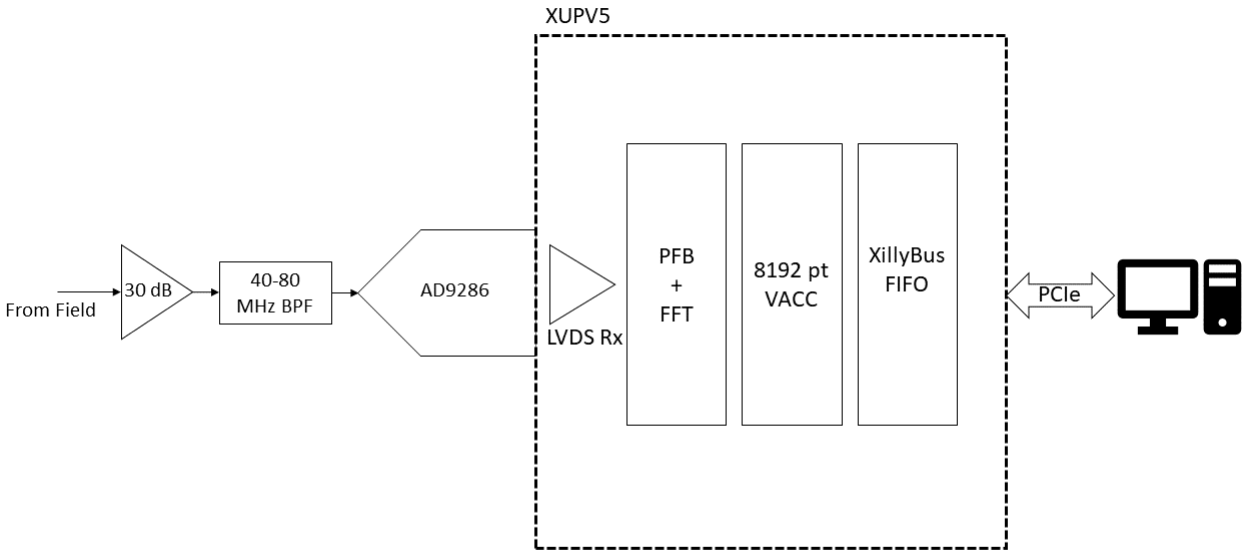

Figure 4.7: XUPV5-AD9286 Spectrometer Block Diagram

1. Capture the high speed data from ADC
2. Carry-out pre-filtering
3. Real time fourier transforming of the data
4. Accumulation of the data to obtain the spectrum with reasonable SNR, and
5. Transfer of the spectrum data to a data acquisition computer.

For acquiring the LVDS data from the ADC, the same strategy that was used for the VLBI system was used. The acquired data was passed through a Polyphase Filter Bank (PFB). The PFB is used to reduce leakage of signal to neighboring channel and to flatten the pass band. The filtered output is then fourier transformed using a Real FFT Block. A Real FFT uses only half the amount of resources required for the complex FFT. The magnitude of the FFT output is estimated and is accumulated for an

integration time, which is specified by the user before the commencement of the observations.

Since the operations are all fixed point, it becomes important to keep track of how the bit size grows as the processing happens. The data from the ADC is 8-bit wide and is a 8.7 fixed point number. This data grows upto 18.17 after the filtering stage, and 36.34 after the FFT module. This data is accumulated in a 64.40 bit accumulator, and the accumulated data is requantized to 32.30 bits.

This output spectrum is packetized and is stored in a FIFO. The write-to FIFO function of the FIFO is enabled by the data-valid output of the accumulator. This data is then transferred to the PC through PCI Express (PCIe) wrapped in a Xillybus IP Core.

Xillybus is a PCIe based IP core which allows the host PC to access FIFOs on-board the FPGA like they were linux device files. The reading of the FIFO is controlled completely by the IP's internal signalling layers. The data is transferred to a shared memory on the host computer and then to a destination specified by the user.

Once preliminary tests of the firmware were carried out successfully, the system was used for solar observations. The intention was to observe fine structures in time and frequency in Solar radio bursts. This is elaborated in the next section.

During this time, simultaneous observations with the conventional spectrum analyzer backend of GLOSS was also carried out, which facilitated the comparison of data obtained from both the instruments. The FPGA system was observed to provide a SNR improvement of ≈ 20 times to that of the former. This is because the number of samples that is being integrated is more in the case of the new backend. Also, the superior temporal and spectral resolution of the instrument enabled us to observe fine structures that hitherto were unobserved with the spectrum analyzer backend.

4.7 Coronal Electron Density Diagnostics using Solar Type IIIb bursts

4.7.1 Introduction to Type IIIb bursts

Inhomogeneities in the solar corona and the solar wind lead to turbulent density fluctuations. Study of the latter is important to understand the low values of observed radio brightness temperature of the "undisturbed" Sun and the angular broadening/location of compact solar radio sources [Aubier et al. 1971, Bastian 1994, Sastry 1994, Thejappa and Kundu 1994, Ramesh 2000, Ramesh and Sastry 2000, Ramesh et al. 2000, Kathiravan and Ramesh 2004, Subramanian 2004, Ramesh et al. 2006, 2010b, Subramanian and Cairns 2011, Ramesh et al. 2012b, Morosan et al. 2014, Mercier and Chambe 2015, Morosan et al. 2015]. Measurements of density fluctuations have been carried out over large heliocentric distances from $10R_\odot$ up to $215R_\odot$ [Bavassano and Bruno 1995, Woo et al. 1995, Ramesh et al. 2001, Spangler 2002, Tokumaru et al. 2012, Bisoi et al. 2014, Sasikumar Raja et al. 2016]. However such measurements below $10R_\odot$ have not been possible to date due to various technical difficulties. Cairns et al. [2009] have suggested that observations of transient radio emission over the frequency range 30 – 300 MHz may be used to probe the density profile of the solar corona corresponding to $r \leq 2R_\odot$.

Type III solar radio bursts are thought to be generated through plasma oscillations induced by energetic electron streams travelling along "open" magnetic field-lines [Ginzburg and Zhelezniakov 1958, Sasikumar Raja and Ramesh 2013, Reid and Ratcliffe 2014]. They appear as individual or a group (of 10 or more bursts) of fast drifting ($\delta f / \delta t \approx 100\,\mathrm{MHz\,s^{-1}}$) enhanced features in the dynamic spectral records during impulsive phase of flares (see for *e.g.* Nindos et al. [2011]) with a duration of a few tens of seconds. Occasionally, however, they appear when there is little (refer *e.g.* Alissandrakis et al. [2015]) or no associated activity at other wavelengths.

At times, a chain of short duration narrow-band bursts have been observed to occur with an overall envelope having a drift rate similar to that of type III bursts and are called type IIIb bursts [Ellis and McCulloch 1967, de La Noe and Boischot 1972]. The spectral fragmentations within the type

IIIb bursts are sometimes referred to as “stria" [de La Noe and Boischot 1972]. Individual striae have been observed to have an average bandwidth and duration of ≈ 50 kHz and ≈ 1.2 s, respectively. Takakura and Yousef [1975] have suggested that stria-like features in type IIIb bursts could be caused by density inhomogeneities along the path of the electron beams [Smith and de La Noe 1976, Tun Beltran et al. 2015]. This has been verified subsequently through numerical modelling [Kontar 2001, Li et al. 2011b,a, 2012, Loi et al. 2014]. It has also been suggested by Loi et al. [2014] that the aforementioned properties of type IIIb bursts can be used to probe the density inhomogeneities in the solar corona and the solar wind.

To address the above, we present and analyze here the spectral observations of solar type IIIb radio bursts in the frequency range of $80-40$ MHz from GLOSS. The radio emission from the Sun corresponding to the above frequency interval typically originates in the distance range $r \approx 1.6-2.2R_{\odot}$ in the solar corona.

4.7.2 Observations

The observations described here were obtained over a period of July - October, 2016 with the Fast Fourier Transform Spectrometer (FFTS) as the backend for GLOSS. The observations were carried out in the spectral band of $40-80$ MHz, with a spectral and temporal resolution of 24 kHz and 5 ms, respectively. The data was then integrated in time to upto 40 ms to improve the SNR.

During the aforementioned observing period, type IIIb radio bursts were detected on four different days. Figure 4.8 shows a typical type IIIb radio burst observed with the GLOSS-FFTS on 20 July 2016, around 07:45 UT. The burst was not particularly associated with any flare at the time of occurrence[6] although a SF class Hα and a B6.6 class X-ray flare during 08:16 – 08:25 UT were reported from the active region AR 12565 located at the heliographic coordinates N01W34. We note that during the time of observation of the type IIIb bursts no particular flares at other wavelengths were reported. These bursts probably belong to the category of weak energy releases [Ramesh et al. 2010a, 2013, Suresh et al. 2017]. A total of

[6]See `http://www.swpc.noaa.gov/`.

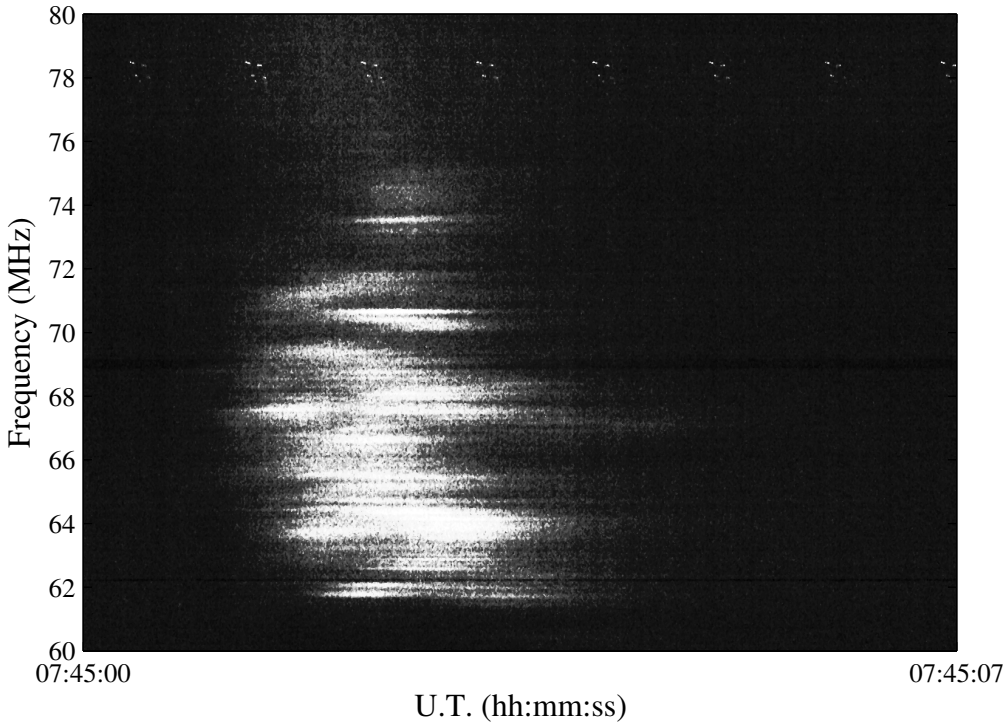

Figure 4.8: Type IIIb radio burst event recorded on 20 July 2016. The narrow-band features are striae which the constitute the type IIIb burst.

19 type IIIb bursts were recorded with our instrument, each with a typical duration and bandwidth of ≈ 3 seconds and ≈ 15 MHz respectively (refer Table 5.2). Each of the type IIIb events were found to be composed of $\approx 15-60$ stria within the bandwidth of the burst. Figure 4.9 shows the instantaneous spectral profile of the type IIIb burst shown in Figure 4.8. The amplitude variations seen in the spectral-cut correspond to the striae within the type IIIb event. The individual striae were found to have a spectral width between 24 kHz – 100 kHz with a duration of ≈ 1 second and did not show any significant drift in frequency. These are consistent with previously reported observations of type IIIb bursts [de La Noe and Boischot 1972, Krishan et al. 1980, Melnik et al. 2009, 2011].

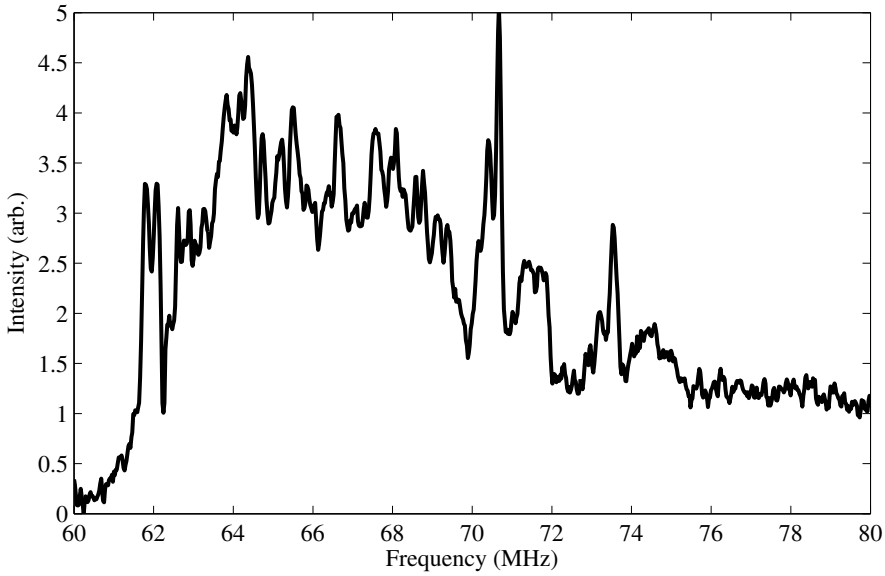

Figure 4.9: Spectral profile of the type IIIb radio burst event shown in Figure 4.8.

4.7.3 Analysis and Results

4.7.3.1 Estimation of $\frac{\delta N_e}{N_e}$

For the present work we have considered only the single individual stria bursts within the type IIIb events (see Table 4.1) for analysis in order to avoid ambiguities. The choice of the striae were constrained as follows: i) the stria are bright enough to be distinguishable from the smooth type III background; ii) the stria remain stationary in frequency with no noticeable frequency drift. From the spectral profile we marked and noted the upper (f_u), lower (f_l) and central (f_c) frequencies corresponding to the spectral width of the striae. The above values were then used to estimate $\frac{\delta N_e}{N_e}$ by applying Equations 4.6 and 4.7:

$$f_p = 8980\sqrt{N_e} \quad \text{Hz} \tag{4.6}$$

and

$$\frac{\delta N_e}{N_e} = \frac{f_u^2 - f_l^2}{f_c^2}. \tag{4.7}$$

Table 4.1: List of type IIIb bursts recorded with FFTS.

Date	Time UT (hh:mm:ss)	Duration (seconds)	Frequency range (MHz)
20 July 2016	07:45:02	3	75 – 60
13 August 2016	05:37:14	3	68 – 54
	05:37:34	2	71 – 55
	05:38:04	4	72 – 54
	06:37:45	5	87 – 52
	08:58:02	2	80 – 55
10 October 2016	05:38:36	5	70 – 48
	06:15:21	4	65 – 48
	06:58:22	4	68 – 45
12 October 2016	06:03:57	3	59 – 47
	06:04:14	4	60 – 46
	06:05:11	2	58 – 47
	06:05:14	3	6 – 47
	06:05:40	3	62 – 48
	08:39:18	4	65 – 50
	08:39:23	2	70 – 55
	08:39:25	3	68 – 53
	08:39:30	2	70 – 48
	08:40:39	3	58 – 43

The above analysis was carried out for each of the individual stria selected from all the type IIIb events reported in Table 5.2. Figure 4.10 shows the histogram distribution of the estimated values of $\frac{\delta N_e}{N_e}$ from all the type IIIb bursts listed in Table 4.1. It can be noted that the most frequent value of $\frac{\delta N_e}{N_e}$ is found to be $\approx 0.006 \pm 0.002$. This is consistent with the values of $\frac{\delta N_e}{N_e}$ at distances < 1 AU reported in the literature [Woo et al. 1995, Bavassano and Bruno 1995, Huddleston et al. 1995, Bisoi et al. 2014].

We adopted the Baumbach-Allen electron density model [Baumbach 1937, Allen 1947] in-order to study the radial dependence of $\frac{\delta N_e}{N_e}$. Assuming that the spectral fine-structures in type IIIb bursts are due to density

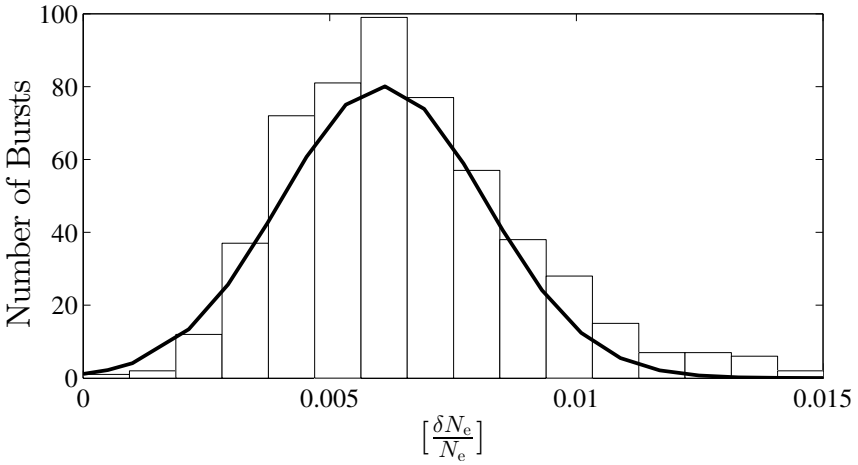

Figure 4.10: A histogram of $\frac{\delta N_e}{N_e}$ obtained from type-IIIb events. The *solid* line is a Gaussian fit to the distribution.

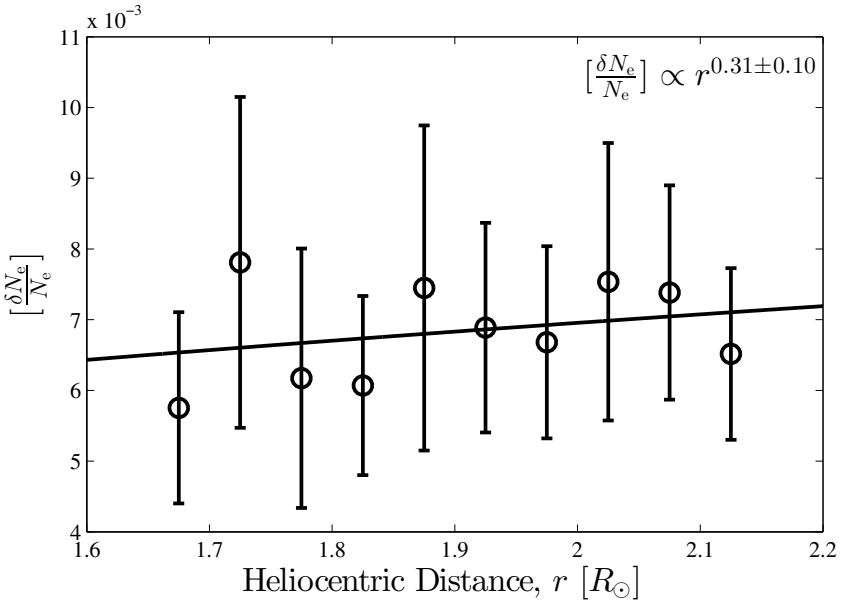

Figure 4.11: Distribution of mean $\frac{\delta N_e}{N_e}$ over $r \approx 1.6-2.2R_\odot$. The *solid* line is a least-squares power law fit (refer Table 5.3 for details). The *error-bars* represent the spread in the data at the respective values of r.

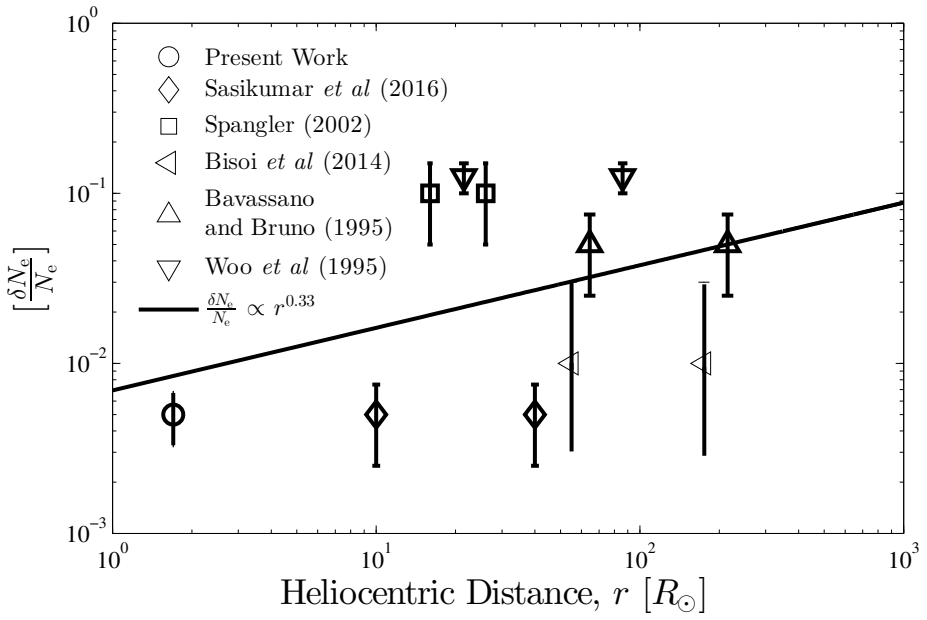

Figure 4.12: Distribution of Density modulation index ($\frac{\delta N_e}{N_e}$) over the heliocentric distance range from $\approx 1.5-215 R_\odot$ (1 AU). The axes are in log-log scale. The *error-bars* represent the spread in the data at the respective values of r. The solid line represents a least square power law fit to the data, with a power law index of ≈ 0.33.

inhomogeneities along the path of the type III beam, we considered an enhancement factor of 10 similar to that considered in the simulation studies by Li et al. [2012] and Loi et al. [2014]. Also, 10× Baumbach-Allen model represents a reasonable estimate of electron density enhancement in the corona during times of activity [Maxwell and Thompson 1962, Stewart 1976, Dryer and Maxwell 1979, Ramesh et al. 2005]. Thus, when using the above model, our observing frequency range of 40 – 80 MHz then translates to $r \approx 1.6-2.2 R_\odot$. The study on the radial dependence of $\frac{\delta N_e}{N_e}$ was carried out for all the events on individual days of observation and also for the combined data set from all four days, the results of which are summarized in Table 4.2.

Figure 4.11 shows the distribution of $\frac{\delta N_e}{N_e}$ values over heliocentric distance obtained from the combined data of all four days. A least squares

power law fit ($\propto r^{\beta}$) to the data indicates that $\frac{\delta N_e}{N_e}$ shows a weak variation with heliocentric distance, with an index, $\beta \approx 0.31 \pm 0.10$. When estimated separately for each day, the obtained β is found to lie in the range of $0.28 - 0.40$. Further, we find that mean value of $\frac{\delta N_e}{N_e}$ obtained from our measurements when combined with those obtained through other methods (*viz*. Interplanetary Scintillation (IPS), Radio Source occultation, *Very Long Baseline Interferometry* (VLBI) and Spacecraft observations), also show a power law variation with $\beta \approx 0.33$ over $r = 1.5 - 215 R_{\odot}$ (refer Figure 4.12). Reid and Kontar [2010] also predicted similar variation of $\frac{\delta N_e}{N_e}$ ($\propto r^{0.25}$) to be up to 1 AU for transport of type III electrons. This shows that the $\frac{\delta N_e}{N_e}$ ratio obtained here is consistent with previously reported values and follows the same trend in the inner corona as well.

Table 4.2: Summary of analysis.

Date	$\frac{\delta N_e}{N_e}$ (%)	Heliocentric Distance (r) ($R_{\odot}$)	Power Law Index (β)
20 July 2016	0.5±0.11	1.6 – 2.0	0.29±0.13
13 August 2016	0.6±0.19	1.6 – 2.1	0.40±0.15
10 October 2016	0.5±0.12	1.7 – 2.2	0.31±0.10
12 October 2016	0.6±0.23	1.7 – 2.2	0.28±0.11
Overall	0.6±0.20	1.6 – 2.2	0.31±0.10

4.7.3.2 Nature of Density Fluctuations

It has been suggested that the solar corona and solar wind follow a Kolmogorov-like power law spectrum with wavenumber, $k = 2\pi/l$, where l is the scale size involved in the turbulence cascade [Marsch 1991, Goldstein et al. 1995, Cranmer 2007]. Since we carried out spectral observations, the largest and smallest measurable scales depend on the observation bandwidth and frequency resolution, respectively. The scales are estimated using the density model assumed in the previous section. Since the spectral enhancements in the type IIIb could be due to local density

inhomogeneities, the bandwidth of the stria at different frequencies correspond to the turbulence scale there [Loi et al. 2014]. Figure 4.13 shows the $(\frac{\delta N_e}{N_e})^2$ spectrum in log scale, where the small and intermediate scales correspond to the spectral width of the individual stria and their fluctuating background, respectively while the large scales correspond to the overall spectral extent of the type IIIb burst.

A fit to the data shows that the spectrum has an index $\alpha \approx$-1.70±0.02. This is in close agreement with the one-dimensional Kolmogorov spectral index [$\propto k^{-5/3}$] [Reid and Kontar 2010, Loi et al. 2014]. The minimum scale length estimated from our data corresponds to $l_{min} \approx$520 km. But even after reaching this scale, there is no evidence of spectral flattening which is expected beyond the inner scale. This suggests that the inner scale[7] (l_i) could be smaller than the minimum scale obtained from this dataset. Note that flattening of the spectrum ($\propto k^{-1.1}$) at distances $\leq 20R_\odot$has been observed [Woo and Armstrong 1979]; The former has been reported to set in at shorter scales ($\approx 3-300$ km), shifting to larger k sunward [Coles et al. 1991, Imamura et al. 2005, Mullan 1990].

4.7.3.3 Determination of $C_n^2(R)$

As a corollary, we used the estimated $\frac{\delta N_e}{N_e}$ and α to calculate the amplitude of density fluctuations, $C_n^2(R)$. To date, estimation of $C_n^2(R)$ has only been performed for r=$10-60R_\odot$, using *in situ* spacecraft and VLBI observations (refer Section 4.7.1). Sasikumar Raja et al. [2016] used data from the occultation of the radio source 3C144 by the solar corona to obtain $C_n^2(R)$ for r=$10-45R_\odot$. They found a solar-cycle dependent power law variation of $C_n^2(R)$ with r.

The relation between $(\frac{\delta N_e}{N_e})^2$, α and $C_n^2(R)$, for a one-dimensional turbulence spectrum at the inner scale usually is (Sasikumar Raja et al. [2016], Subramanian and Cairns [2011] and references therein) :

$$C_n^2(r) \propto \frac{[\frac{\delta N_e}{N_e}]^2 {N_e}^2}{4\pi k_i^{2-\alpha} e^{-1}}, \tag{4.8}$$

where the wavenumber at the inner scale (l_i) is k_i=$\frac{2\pi}{l_i}$. Note that for a three-dimensional turbulence spectrum k_i is raised to 3-α.

[7]The scale beyond which turbulence cascade energy begins to dissipate.

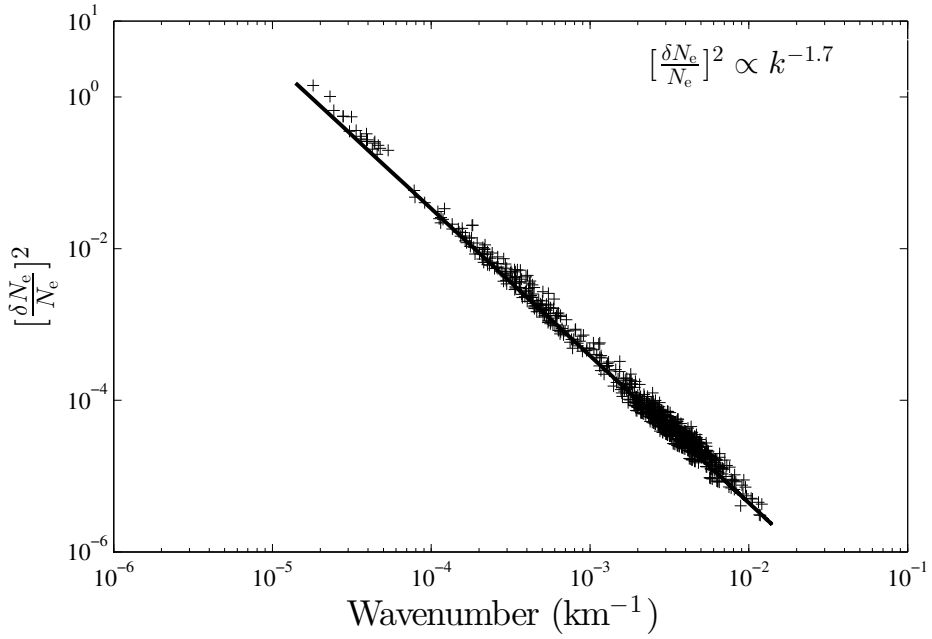

Figure 4.13: Spectrum of $(\frac{\delta N_e}{N_e})^2$ fluctuations. Both axis are plotted in log-scale.

There has been considerable debate as to what is the smallest scale present in the corona and the solar wind [Mullan 1990]. Sasikumar Raja et al. [2016] have shown that scales of the order of 1.6 km exist at $r < 10R_\odot$. In view of recent *in situ* spacecraft and IPS observations [Bale et al. 2005, Alexandrova et al. 2009, 2012, Bisoi et al. 2014], it has been suggested that dissipation could occur down to proton and electron gyro-radii scales (ρ_p) [Chen et al. 2014]. The proton gyroradius (ρ_p) is given by:

$$\rho_p(r) = 102\sqrt{\mu T_i}B(r)^{-1} \quad [\text{cm}], \tag{4.9}$$

where μ is the ratio of the mass of ions to that of protons, which is ≈ 1, and where T_i is the proton temperature in eV, and $B(r)$ is the coronal magnetic field, which can be modelled as $B(r) = 0.5(r-1)^{-1.5}$ [G] [Dulk and McLean 1978, Ramesh et al. 2010c, 2011].

The electron gyroradius (ρ_e) is:

$$\rho_e = 2.38\sqrt{T_e}B(r)^{-1} \quad [\text{cm}]. \tag{4.10}$$

In this work, we consider both electron and proton gyroradii as the inner scale for $C_n^2(R)$ estimation. We used Equation 4.8 to obtain the $C_n^2(R)$ values corresponding to $\frac{\delta N_e}{N_e}$ using α estimated earlier in this paper (see Section 4.7.3.2) for both the inner scale estimates. The $C_n^2(R)$ calculated was "binned" to different solar radii and its scatter with respect to r was obtained. A least squares power law of the form Ar^γ was fit to the data obtained for both the inner scale considerations. We show a representative scatter of the behaviour of $C_n^2(R)$ against r, considering $l_i = \rho_e$ in Figure 4.14. A similar fit with $l_i = \rho_p$ yielded the following fit parameters: A $\approx 4.79 \pm 1.50 \times 10^{11}$ m$^{-11/3}$ and $\gamma \approx -4.09 \pm 2.00$. However, the $C_n^2(R)$ estimates have to be treated with caution as these depend strongly on l_i, which is not yet precisely known.

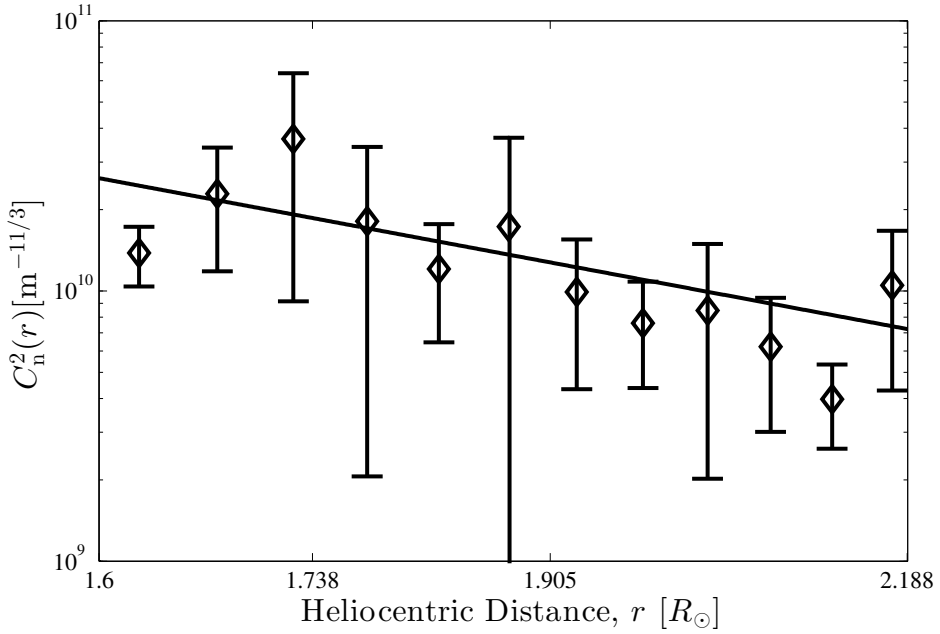

Figure 4.14: Log-Log plot of $C_n^2(R)$ with r, for a spectrum with $\alpha \approx$ -1.7 and inner scale as electron gyroradius. The *solid* line is a power law fit of the form Ar^γ. The fitted values are A=1.8±1.0×10^{11} m$^{-11/3}$ and γ=−4.11±1.75. The *error-bars* represent the spread in the data at the respective values of r.

4.8 Summary

The first estimate $\frac{\delta N_e}{N_e}$ and $C_n^2(R)$ for r=1.6 – 2.2$R_\odot$ from the observations of type IIIb solar radio bursts has been described in this chapter. $\frac{\delta N_e}{N_e}$ varies with r as a power law with index $\beta \approx 0.33$. Note that previous estimates of $\frac{\delta N_e}{N_e}$ through techniques like IPS, Radio Source occultation, VLBI and *in situ* spacecraft measurements were limited to $r \geq 10R_\odot$ [Woo et al. 1995, Bavassano and Bruno 1995, Ramesh et al. 2001, Spangler 2002, Bisoi et al. 2014, Sasikumar Raja et al. 2016]. It has been suggested by several authors [Takakura and Yousef 1975, Smith and de La Noe 1976, de La Noe and Boischot 1972, Tun Beltran et al. 2015] that striations in type IIIb radio burst emission can be due to electron density variations along the path the electron beams causing the type III bursts. Subsequent numerical modelling has shown that stria-like fine structure emissions can indeed arise from density or temperature inhomogeneities along the path of the exciter and thus can be effective probes of the same [Kontar 2001, Li et al. 2011a,b, 2012, Loi et al. 2014]. We use the values of $(\frac{\delta N_e}{N_e})^2$ obtained from the data and determine that the density modulation index follows a Kolmogorov-like spectrum ($\propto k^{-1.7}$) for the range of values of r examined in this work.

As a corollary, we use the obtained values of $(\frac{\delta N_e}{N_e})^2$ and α to estimate the behaviour of $C_n^2(R)$ with r. It is found that the former shows a power law variation radially with an index ≈ -4.2.

The results presented here are consistent with those obtained using other techniques *viz.* IPS, VLBI and occultation experiments. Studies like the one presented here are useful to understand scattering due to density fluctuations in the solar corona, and the spatial extent of the smallest observed compact sources there [Ramesh et al. 1999, Ramesh and Sastry 2000, Ramesh and Ebenezer 2001, Mercier et al. 2006, 2015, Kathiravan et al. 2011, Ramesh et al. 2012a, Mugundhan et al. 2016]. Thus, we suggest that observations of fine-structure/fragmented radio emission [Thejappa et al. 2003, Pohjolainen et al. 2008, Tun Beltran et al. 2015] with high spectro-temporal resolution [Hariharan et al. 2016] can be a used as a proxy for density turbulence measurements in the solar corona, particularly in the range $r < 10R_\odot$ which is presently unavailable.

References

Alexandrova, O., Lacombe, C., Mangeney, A., Grappin, R., and Maksimovic, M. (2012). Solar Wind Turbulent Spectrum at Plasma Kinetic Scales. *Astrophys. J.*, 760:121.

Alexandrova, O., Saur, J., Lacombe, C., Mangeney, A., Mitchell, J., Schwartz, S. J., and Robert, P. (2009). Universality of Solar-Wind Turbulent Spectrum from MHD to Electron Scales. *Physical Review Letters*, 103(16):165003.

Alissandrakis, C. E., Nindos, A., Patsourakos, S., Kontogeorgos, A., and Tsitsipis, P. (2015). A tiny event producing an interplanetary type III burst. *Astron. Astrophys.*, 582:A52.

Allen, C. W. (1947). Interpretation of Electron Densities from Corona Brightness. *Mon. Not. Roy. Astron. Soc.*, 107:426.

Aubier, M., Leblanc, Y., and Boischot, A. (1971). Observations of the Quiet Sun at Decameter Wavelengths - Effects of Scattering on the Brightness Distribution. *Astron. Astrophys.*, 12:435.

Bale, S. D., Kellogg, P. J., Mozer, F. S., Horbury, T. S., and Reme, H. (2005). Measurement of the Electric Fluctuation Spectrum of Magnetohydrodynamic Turbulence. *Physical Review Letters*, 94(21):215002.

Bastian, T. S. (1994). Angular scattering of solar radio emission by coronal turbulence. *Astrophys. J.*, 426:774–781.

Baumbach, S. (1937). Strahlung, ergiebigkeit und elektronendichte der sonnenkorona. *Astronomische Nachrichten*, 263(6):121–134.

Bavassano, B. and Bruno, R. (1995). Density fluctuations and turbulent Mach numbers in the inner solar wind. *J. Geophys. Res.*, 100:9475–9480.

Bisoi, S. K., Janardhan, P., Ingale, M., Subramanian, P., Ananthakrishnan, S., Tokumaru, M., and Fujiki, K. (2014). A Study of Density Modulation Index in the Inner Heliospheric Solar Wind during Solar Cycle 23. *Astrophys. J.*, 795:69.

Bracewell, R. N. and Bracewell, R. N. (1986). *The Fourier transform and its applications*, volume 31999. McGraw-Hill New York.

Cairns, I. H., Lobzin, V. V., Warmuth, A., Li, B., Robinson, P. A., and Mann, G. (2009). Direct Radio Probing and Interpretation of the Sun's Plasma Density Profile. *Astrophys. J. Lett.*, 706:L265–L269.

Chen, C. H. K., Leung, L., Boldyrev, S., Maruca, B. A., and Bale, S. D. (2014). Ion-scale spectral break of solar wind turbulence at high and low beta. *Geophysical Research Letters*, 41(22):8081–8088.

Coles, W., Liu, W., Harmon, J., and Martin, C. (1991). The solar wind density spectrum near the sun: Results from voyager radio measurements. *Journal of Geophysical Research: Space Physics*, 96(A2):1745–1755.

Cooley, J. W. and Tukey, J. W. (1965). An algorithm for the machine calculation of complex fourier series. *Mathematics of computation*, 19(90):297–301.

Cranmer, S. R. (2007). Turbulence in the solar corona. In Shaikh, D. and Zank, G. P., editors, *Turbulence and Nonlinear Processes in Astrophysical Plasmas*, volume 932 of *American Institute of Physics Conference Series*, pages 327–332.

de La Noe, J. and Boischot, A. (1972). The Type III B Burst. *Astron. Astrophys.*, 20:55.

Dryer, M. and Maxwell, A. (1979). Radio data and a theoretical model for the fast-mode MHD shock wave generated by the solar flare of 1973 September 5, 18:26 UT. *Astrophys. J.*, 231:945–959.

Dulk, G. A. and McLean, D. J. (1978). Coronal magnetic fields. *Solar Phys.*, 57:279–295.

Ellis, G. R. A. and McCulloch, P. M. (1967). Frequency splitting of solar radio bursts. *Australian Journal of Physics*, 20:583.

Ginzburg, V. L. and Zhelezniakov, V. V. (1958). On the Possible Mechanisms of Sporadic Solar Radio Emission (Radiation in an Isotropic Plasma). *Soviet Astron.*, 2:653.

Goldstein, M. L., Roberts, D., and Matthaeus, W. (1995). Magnetohydrodynamic turbulence in the solar wind. *Annual review of astronomy and astrophysics*, 33(1):283–325.

Hariharan, K., Ramesh, R., Kathiravan, C., Abhilash, H. N., and Rajalingam, M. (2016). High Dynamic Range Observations of Solar Coronal Transients at Low Radio Frequencies with a Spectro-correlator. *Astrophys. J. Suppl.*, 222:21.

Huddleston, D. E., Woo, R., and Neugebauer, M. (1995). Density fluctuations in different types of solar wind flow at 1 AU and comparison with results from Doppler scintillation measurement near the Sun. *J. Geophys. Res.*, 100:19951–19956.

Imamura, T., Noguchi, K., Nabatov, A., Oyama, K.-I., Yamamoto, Z., and Tokumaru, M. (2005). Phase scintillation observation during coronal sounding experiments with NOZOMI spacecraft. *Astron. Astrophys.*, 439:1165–1169.

Kathiravan, C. and Ramesh, R. (2004). Estimation of the Three-Dimensional Space Speed of a Coronal Mass Ejection Using Metric Radio Data. *Astrophys. J.*, 610:532–536.

Kathiravan, C., Ramesh, R., Barve, I. V., and Rajalingam, M. (2011). Radio Observations of the Solar Corona During an Eclipse. *Astrophys. J.*, 730:91.

Kishore, P. (2016). *Development of a broadband radio spectropolarimeter for solar observations*. PhD thesis, Indian Institute of Astrophysics.

Kishore, P., Kathiravan, C., Ramesh, R., Rajalingam, M., and Barve, I. V. (2014). Gauribidanur Low-Frequency Solar Spectrograph. *Solar Phys.*, 289:3995–4005.

Kontar, E. P. (2001). Dynamics of electron beams in the solar corona plasma with density fluctuations. *Astron. Astrophys.*, 375:629–637.

Krishan, V., Subramanian, K. R., and Sastry, C. V. (1980). Observations and interpretation of solar decameter type IIIb radio bursts. *Solar Phys.*, 66:347–355.

Li, B., Cairns, I. H., and Robinson, P. A. (2011a). Effects of Spatial Variations in Coronal Electron and Ion Temperatures on Type III Bursts. II. Variations in Ion Temperature. *Astrophys. J.*, 730:21.

Li, B., Cairns, I. H., and Robinson, P. A. (2011b). Effects of Spatial Variations in Coronal Temperatures on Type III Bursts. I. Variations in Electron Temperature. *Astrophys. J.*, 730:20.

Li, B., Cairns, I. H., and Robinson, P. A. (2012). Frequency Fine Structures of Type III Bursts Due to Localized Medium-Scale Density Structures Along Paths of Type III Beams. *Solar Phys.*, 279:173–196.

Loi, S. T., Cairns, I. H., and Li, B. (2014). Production of Fine Structures in Type III Solar Radio Bursts Due to Turbulent Density Profiles. *Astrophys. J.*, 790:67.

Marsch, E. (1991). Turbulence in the Solar Wind. In Klare, G., editor, *Reviews in Modern*

Astronomy, volume 4 of *Reviews in Modern Astronomy*, pages 145–156.

Maxwell, A. and Thompson, A. R. (1962). Spectral Observations of Solar Radio Bursts. II. Slow-Drift Bursts and Coronal Streamers. *Astrophys. J.*, 135:138.

Melnik, V., Rucker, H., Konovalenko, A., Abranin, E., Dorovskyy, V., Boiko, A., and Lecacheux, A. (2009). Observation of powerful solar Type III bursts at frequencies 10-30MHz. In *European Planetary Science Congress 2009*, page 421.

Melnik, V. N., Rucker, H. O., Konovalenko, A. A., Dorovskyy, V. V., and Tan, S. (2011). Decameter IIIb-III pairs. In *EPSC-DPS Joint Meeting 2011*, page 796.

Mercier, C. and Chambe, G. (2015). Electron density and temperature in the solar corona from multifrequency radio imaging. *Astron. Astrophys.*, 583:A101.

Mercier, C., Subramanian, P., Chambe, G., and Janardhan, P. (2015). The structure of solar radio noise storms. *Astron. Astrophys.*, 576:A136.

Mercier, C., Subramanian, P., Kerdraon, A., Pick, M., Ananthakrishnan, S., and Janardhan, P. (2006). Combining visibilities from the giant meterwave radio telescope and the Nancay radio heliograph. High dynamic range snapshot images of the solar corona at 327 MHz. *Astron. Astrophys.*, 447:1189–1201.

Morosan, D., Gallagher, P., Zucca, P., O'flannagain, A., Fallows, R., Reid, H., Magdalenić, J., Mann, G., Bisi, M., Kerdraon, A., et al. (2015). Lofar tied-array imaging and spectroscopy of solar s bursts. *Astron. Astrophys.*, 580:A65.

Morosan, D. E., Gallagher, P. T., Zucca, P., Fallows, R., Carley, E., Mann, G., Bisi, M., Kerdraon, A., Konovalenko, A., MacKinnon, A., et al. (2014). Lofar tied-array imaging of type III solar radio bursts. *Astron. Astrophys.*, 568:A67.

Mugundhan, V. (2014). *Beam-former for single beam, total power mode observations with Gauribidanur Radioheliograph*. PhD thesis, Indian Institute of Astrophysics.

Mugundhan, V., Ramesh, R., Barve, I. V., Kathiravan, C., Gireesh, G. V. S., Kharb, P., and Misra, A. (2016). Low-Frequency Radio Observations of the Solar Corona with Arcminute Angular Resolution: Implications for Coronal Turbulence and Weak Energy Releases. *Astrophys. J.*, 831:154.

Mullan, D. J. (1990). Sources of the solar wind - What are the smallest-scale structures? *Astron. Astrophys.*, 232:520–535.

Nindos, A., Alissandrakis, C. E., Hillaris, A., and Preka-Papadema, P. (2011). On the relationship of shock waves to flares and coronal mass ejections. *Astron. Astrophys.*, 531:A31.

Pohjolainen, S., Pomoell, J., and Vainio, R. (2008). CME liftoff with high-frequency fragmented type II burst emission. *Astron. Astrophys.*, 490:357–363.

Proakis, J. G. and Manolakis, D. G. (1996). Digital signal processing 3 rd edition.

Ramesh, R. (2000). Low Frequency Radio Emission from the 'Quiet Sun'. *Journal of Astrophysics and Astronomy*, 21:237.

Ramesh, R. (2011). Low frequency solar radio astronomy at the Indian Institute of Astrophysics (IIA). In *Astronomical Society of India Conference Series*, volume 2 of *Astronomical Society of India Conference Series*.

Ramesh, R. and Ebenezer, E. (2001). Decameter Wavelength Observations of an Absorption Burst from the Sun and Its Association with an X2.0/3B Flare and the Onset of a

"Halo" Coronal Mass Ejection. *Astrophys. J. Lett.*, 558:L141–L143.

Ramesh, R., Kathiravan, C., Barve, I. V., Beeharry, G. K., and Rajasekara, G. N. (2010a). Radio Observations of Weak Energy Releases in the Solar Corona. *Astrophys. J. Lett.*, 719:L41–L44.

Ramesh, R., Kathiravan, C., Barve, I. V., and Rajalingam, M. (2012a). High Angular Resolution Radio Observations of a Coronal Mass Ejection Source Region at Low Frequencies during a Solar Eclipse. *Astrophys. J.*, 744:165.

Ramesh, R., Kathiravan, C., Kartha, S. S., and Gopalswamy, N. (2010b). Radioheliograph Observations of Metric Type II Bursts and the Kinematics of Coronal Mass Ejections. *Astrophys. J.*, 712:188–193.

Ramesh, R., Kathiravan, C., and Narayanan, A. S. (2011). Low-frequency Observations of Polarized Emission from Long-lived Non-thermal Radio Sources in the Solar Corona. *Astrophys. J.*, 734:39.

Ramesh, R., Kathiravan, C., and Sastry, C. V. (2001). Low-Frequency Radio Observations of the Angular Broadening of the Crab Nebula Due to a Coronal Mass Ejection. *Astrophys. J. Lett.*, 548:L229–L231.

Ramesh, R., Kathiravan, C., and Sastry, C. V. (2010c). Estimation of Magnetic Field in the Solar Coronal Streamers Through Low Frequency Radio Observations. *Astrophys. J.*, 711:1029–1032.

Ramesh, R., Lakshmi, M. A., Kathiravan, C., Gopalswamy, N., and Umapathy, S. (2012b). The Location of Solar Metric Type II Radio Bursts with Respect to the Associated Coronal Mass Ejections. *Astrophys. J.*, 752:107.

Ramesh, R., Narayanan, A. S., Kathiravan, C., Sastry, C. V., and Shankar, N. U. (2005). An estimation of the plasma parameters in the solar corona using quasi-periodic metric type III radio burst emission. *Astron. Astrophys.*, 431:353–357.

Ramesh, R., Nataraj, H. S., Kathiravan, C., and Sastry, C. V. (2006). The Equatorial Background Solar Corona during Solar Minimum. *Astrophys. J.*, 648:707–711.

Ramesh, R., Sasikumar Raja, K., Kathiravan, C., and Narayanan, A. S. (2013). Low-frequency Radio Observations of Picoflare Category Energy Releases in the Solar Atmosphere. *Astrophys. J.*, 762:89.

Ramesh, R. and Sastry, C. V. (2000). Radio observations of a coronal mass ejection induced depletion in the outer solar corona. *Astron. Astrophys.*, 358:749–752.

Ramesh, R., Subramanian, K. R., and Sastry, C. V. (1999). Eclipse Observations of Compact Sources in the Outer Solar Corona. *Solar Phys.*, 185:77–85.

Ramesh, R., Subramanian, K. R., and Sastry, C. V. (2000). Estimation of the altitude and electron density of a discrete source in the outer solar corona through low frequency radio observations. *Astrophysical Letters and Communications*, 40:93–102.

Reid, H. A. S. and Kontar, E. P. (2010). Solar Wind Density Turbulence and Solar Flare Electron Transport from the Sun to the Earth. *Astrophys. J.*, 721:864–874.

Reid, H. A. S. and Ratcliffe, H. (2014). A review of solar type III radio bursts. *Research in Astronomy and Astrophysics*, 14:773–804.

Sasikumar Raja, K., Ingale, M., Ramesh, R., Subramanian, P., Manoharan, P. K., and Janardhan, P. (2016). Amplitude of solar wind density turbulence from 10 to 45 R.

Journal of Geophysical Research (Space Physics), 121:11.

Sasikumar Raja, K. and Ramesh, R. (2013). Low-frequency Observations of Transient Quasi-periodic Radio Emission from the Solar Atmosphere. *Astrophys. J.*, 775:38.

Sastry, C. V. (1994). Observations of the continuum radio emission from the undisturbed Sun at a wavelength of 8.7 meters. *Solar Phys.*, 150:285–294.

Smith, R. A. and de La Noe, J. (1976). Theory of type IIIb solar radio bursts. *Astrophys. J.*, 207:605–629.

Spangler, S. R. (2002). The Amplitude of Magnetohydrodynamic Turbulence in the Inner Solar Wind. *Astrophys. J.*, 576:997–1004.

Stewart, R. T. (1976). Source heights of metre wavelength bursts of spectral types I and III. *Solar Phys.*, 50:437–445.

Subramanian, K. R. (2004). Brightness temperature and size of the quiet Sun at 34.5 MHz. *Astron. Astrophys.*, 426:329–331.

Subramanian, P. and Cairns, I. (2011). Constraints on coronal turbulence models from source sizes of noise storms at 327 mhz. *Journal of Geophysical Research: Space Physics*, 116(A3):n/a–n/a. A03104.

Suresh, A., Sharma, R., Oberoi, D., Das, S. B., Pankratius, V., Timar, B., Lonsdale, C. J., Bowman, J. D., et al. (2017). Wavelet-based Characterization of Small-scale Solar Emission Features at Low Radio Frequencies. *Astrophys. J.*, 843:19.

Takakura, T. and Yousef, S. (1975). Type IIIb radio bursts - 80 MHz source position and theoretical model. *Solar Phys.*, 40:421–438.

Thejappa, G. and Kundu, M. R. (1994). The effects of large- and small-scale density structures on the radio from coronal streamers. *Solar Phys.*, 149:31–49.

Thejappa, G., Zlobec, P., and MacDowall, R. J. (2003). Polarization and Fragmentation of Solar Type II Radio Bursts. *Astrophys. J.*, 592:1234–1240.

Tokumaru, M., Kojima, M., and Fujiki, K. (2012). Long-term evolution in the global distribution of solar wind speed and density fluctuations during 1997-2009. *Journal of Geophysical Research (Space Physics)*, 117:A06108.

Tun Beltran, S. D., Cutchin, S., and White, S. (2015). A New Look at Type-III Bursts and Their Use as Coronal Diagnostics. *Solar Phys.*, 290:2423–2437.

Woo, R. and Armstrong, J. W. (1979). Spacecraft radio scattering observations of the power spectrum of electron density fluctuations in the solar wind. *Journal of Geophysical Research: Space Physics*, 84(A12):7288–7296.

Woo, R., Armstrong, J. W., Bird, M. K., and Patzold, M. (1995). Variation of fractional electron density fluctuations inside 40 R_0 observed by ULYSSES ranging measurements. *Geophys. Res. Lett.*, 22:329–332.

Chapter 5

Low Frequency Spectropolarimetry

This Chapter is based on Mugundhan V., Ramesh R., et al., 2018, Solar Physics, 293, 41.

5.1 Introduction

Activity in the solar corona is dominated by the ambient magnetic fields present there. These magnetic fields are believed to originate on the photosphere and extend all the way into the interplanetary space. It is believed that electric currents within the Sun give rise to this magnetic field.

Schwabe in 1844 discovered the 11 year periodicity of the sun-spot cycle[Schwabe 1844]. Hale measured the magnetic field of sun-spots and also found that sun-spot pairs are of opposite polarities[Hale 1908, Hale and Nicholson 1925]. Thus, it was recognized measurement of these magnetic fields are important to obtain a better understanding of the Sun and its surroundings.

The effect of the solar magnetic fields on the electromagnetic radiation can be observed as Zeeman Effect[Lin et al. 2004], Hanle Effect[Stenflo 1982], gyro and synchrotron radiation and Faraday rotation of Radio waves[Beckers 1971, Pätzold et al. 1987]. Zeeman effect refers to the splitting of spectral lines in the presence of a magnetic field. When the field is strong, the effect of this splitting is directly observable, but in case of

weak fields, it manifests as a change in polarization. Hanle effect is the resonant scattering of bound electrons in the presence of a magnetic field. When the magnetic field is zero, in the presence of dipole transitions, the scattering results in linear polarization with the polarization angle parallel to the solar limb. But in the presence of weak-fields, the direction and the degree of polarization changes as a function of the magnetic field. Estimation of magnetic fields from Hanle effect has been used with success for field estimation in prominences.

Free electrons, as they spiral around a magnetic field, emit radiation at the gyro-frequency, given by $\omega_l = \frac{eB}{m_e c}$. For electrons with small kinetic energies, this radiation occurs only at ω_l. The radiation is strongly circularly polarized. This radiation can be observed at frequencies < 10GHz. Faraday rotation, or the rotation of the plane of polarization of incident radiation as it passes through a magnetic medium has also been used in the past for observing coronal magnetic fields using beacon signals from spacecraft.

But all the aforementioned techniques provide methods to only measure the fields either in the lower corona or in the outer corona, beyond $10R_\odot$.

Radio waves observed at meter wavelengths from the Sun originate from the region of corona corresponding to $1.5-3.0R_\odot$. Dulk and McLean [1978] suggested that magnetic fields in the above region can be derived using polarimetric observations at meter wavelengths.

The polarization of any radiation can be quantitatively measured using four Stokes Parameters, namely:

1. Stokes I: The total intensity of the observed radiation,
2. Stokes Q: The amount of light polarized at 0°or 180°,
3. Stokes U: The amount of light polarized at 45°or 135°and
4. Stokes V: The amount of circularly polarized radiation.

They are defined mathematically as follows:

$$I = E_x {E_x}^* + E_y {E_y}^* \tag{5.1}$$

$$Q = E_x {E_x}^* - E_y {E_y}^* \tag{5.2}$$

$$U = E_x {E_y}^* + {E_x}^* E_y \tag{5.3}$$

and

$$V = i[E_x {E_y}^* - {E_x}^* E_y], \tag{5.4}$$

Where E_x and E_y are the electric fields parallel and perpendicular to the reference, which in our work is taken to be the celestial North-South (NS) axis.

Antennas, which are the primary sensing elements at low frequencies lend themselves easily for observing these electric field components: An antenna oriented along the NS axis will be sensitive to the E_x component, while that perpendicular will measure E_y. The measured electric field can then be used to estimate the Stokes parameters given in Equations 5.1 – 5.4. An array of antennas to measure the x and y components of the electric field can be setup to obtain increased gain. The use of such an array to measure polarization is described in the rest of this chapter.

5.2 Wideband Backend for Gauribidanur Radio Interferometric Polarimeter (GRIP)

GRIP is a one-dimensional array of 24 Antennas divided into three groups of 8 antennas. Out of these three groups, one is oriented parallel to the celestial north, while the other two are oriented perpendicular to it. The signals from two parallel groups are correlated to obtain Stokes I parameter, while that of two orthogonal groups are correlated to produce Stokes V. The array uses LPDAs as primary receiving elements. The LPDAs are designed to operate in the frequency range of 30 – 120 MHz with a gain of $\approx$ 6dBi. The baseline over which Stokes I and V are measured are $\approx$ 80 m

The signals from the antennas are amplified to $\approx$ 30dB by a Minicircuits MAN-1LN amplifier and are combined using a 8-way power combiner. This signal is then amplified by another 30dB to compensate for losses

Table 5.1: The truth table of an XNOR Gate, which is used as a 1 bit correlator.

A	B	O
0	0	1
0	1	0
1	0	0
1	1	1

incurred during transmission via co-axial cables. Phase-equalized, equal length co-axial cables are used for the signal transmission.

The RF signal from the field is fed into an analog receiver, which comprises a super-heterodyne receiver. The heterodyning is done in two stages: in the first stage, the RF frequency is up-converted to a first IF of ≈250 MHz, which is down-converted using a second LO of 180 MHz to an IF of ≈ 1 MHz bandwidth, centered around 10.7 MHz. This system uses a dual mixing system to ensure that the IF/LO does not fall in the RF band of interest. The second stage, where the down-conversion is done to center the IF at 10.7 MHz is to satisfy the analog bandwidth requirements of the comparator, which is used for 1-bit sampling the data.

The comparator used is AD790. This is used to quantize the data to one bit two level. When signal is higher than a reference (usually GND), the comparator output swings to the $+V_{cc}$ rail, and vice-versa when the signal is less than the reference. These signals from the three groups are sampled by a D Flip-Flop IC at 4 MHz. This signal is correlated in XNOR gate. The truth table of the XNOR gate is shown in Table 5.1.

The number of ones at the output of the XNOR gate is counted in 24 bit counter for a predefined integration time. After this time elapses, the count value is transferred to a register, from where it is transmitted to the data acquisition system.

5.2.1 Wideband Digital Correlator Backend

Recent advances in electronics have enabled the manufacture of data converters with better signal to noise ratio (SNR) and dynamic range, which allow the detection of faint bursts. Digital signal processing in high speed Field Programmable Gate Arrays (FPGA) provide real time signal processing capabilities namely polyphase filtering, fast fourier transform and integration operations. The high spectral resolution would allow us to "flag" channels corrupted by RFI more accurately, resulting in a minimal loss of spectral data.

The main task of the digital receiver is to process the received RF signal and estimate the Stokes parameters. The digital receiver is built around a CASPER[1] Reconfigurable Open Architecture Computer Hardware (ROACH) board. The first stage of the digital receiver is an analog to digital converter (ADC). A CASPER QADC is used for this purpose. QADC has four AD9480 8 bit ADCs from Analog Devices[2]. These four ADCs share a common sampling clock. The maximum possible sampling clock is 250 MHz, which implies a maximum baseband of 125 MHz can be sampled by the ADC. Since the band of interest here is $35-85$ MHz, the sampling frequency used was 200 MHz.

The 8 bits provide a dynamic range of ≈ 48 dB. This is sufficient to accommodate the increase in signal levels during solar bursts [Nelson et al. 1985]. The digitized signal is transmitted to further stages as a low voltage differential signal (LVDS). LVDS signalling transmits a bit of data in two parallel lanes as in-phase and out-of-phase components. This reduces common mode noise in the digitized signal. In order to maintain synchronization with the digitizer, the data has to be captured by the LVDS receiver using the same clock frequency and phase. So, the sampling clock also is transmitted differentially from the ADC. Thus for an 8 bit ADC, there are 16 data lines and 2 clock lines. These lines are interfaced to ROACH using a ZDOK connector. The output signals are captured by the LVDS receivers present in the FPGA on board the ROACH.

The firmware for the system was developed using CASPER Matlab-

[1] see casper.berkeley.edu/

[2] see www.analog.com/en/products/analog-to-digital-converters/ad-converters/ad9480.html

Simulink-System-Generator-Embedded (MSSGE) Development Kit toolflow. The ADC signal is converted from a signed integer to signed fixed point number with 8.7 bit precision. This signal is then operated upon by a polyphase filter bank [Price 2016, Crochiere and Rabiner 1983, Vaidyanathan 1993]. PFB is a combination of a finite impulse respose (FIR) filter followed by an fast Fourier transform (FFT) operation. Polyphase filtering reduces spectral leakage into adjacent channels by ≈ 60 dB and reduces the data rate for further stages of processing. The FFT size is 4096, which resulted in a frequency resolution of ≈ 48.8 kHz. This frequency resolution enabled us to study finer frequency structures in radio emission from the Sun. Also, it helps us identify narrow-band RFI, which is confined to about two or three spectral channels, based on the bandwidth of the interfering signal. The outputs of the individual stages of the FFT are normalized to prevent bit growth and overflow during multiplication operations. Note from the Figure 5.1 that the inputs and the outputs of the FFT block have the same bit width.

The spectrum of signals from each of the antennas are correlated to obtain the Stokes I and Stokes V visibilities. Note that due to the destruction of linearly polarized components because of Faraday rotation in the solar corona for our spectral resolution, we do not estimate or record the Stokes Q and Stokes U components [Ramesh et al. 2008]. The FFT and correlation operations are multiplication intensive, which results in bit growth of the output product. Thus, before correlation, in order to prevent overflow, the spectra is requantized to 8.7 bits. This bit resolution is sufficient to provide correlation that is $\approx 99\%$ of analog correlation [Thompson et al. 2001, Benkevitch et al. 2016].

The quantizer output is fed to the Stokes estimators. The signals from groups 1 and 3 are correlated to estimate Stokes I. The signals from groups 2 and 3 are correlated to obtain Stokes V. Each Stokes estimator has a complex multiplier and an adder block. The output of the adder block is 17.14 bits wide. This output is integrated in the 32 bit wide vector accumulator (VACC).

The vector accumulator is implemented using block RAMs (BRAM) present in the FPGA. The depth of the accumulator is the same as the FFT size. Based on the desired time resolution, the number of spectra

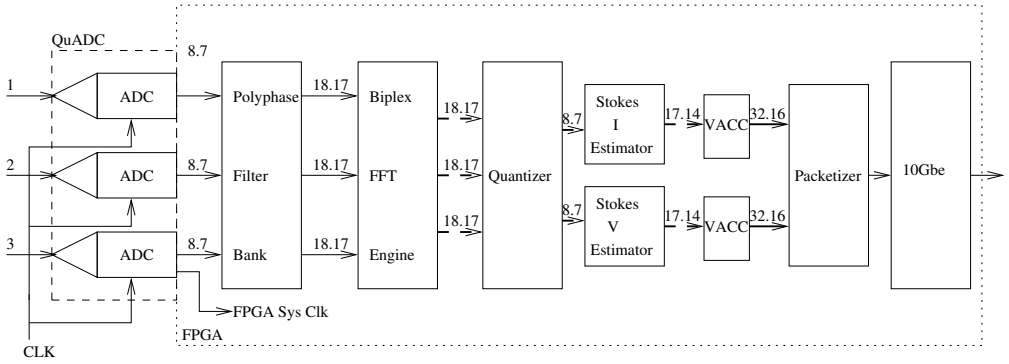

Figure 5.1: The architecture of Digital Backend firmware. Numbers 1,2 and 3 at the input are the respective antenna groups (see Table 5.3). Numbers of format $x.y$ represent the bit-width of the signal being propagated to the next stage, x being the integer component and y, the fractional component. *Broken lines* represent complex numbers. In such case, the $x.y$ denotes the bit width of real/imaginary part.

to be accumulated can be programmed by the observer during the initial configuration of the FPGA. Once the predefined number of spectra have been accumulated, the VACC block generates a pulse, which indicates that the data is ready for processing by further stages.

The accumulated signal has to be prepared for transmission to the data acquisition server (DAS). A Ten Gigabit Ethernet (10Gbe) connection is used for communication to the DAS. A 10Gbe core, which is a part of CASPER toolflow is used for this. The core accepts a 64 bit input. The input samples are stored in an elastic buffer[3], which has a depth equal to the number of bytes (payload) to be transferred. The maximum payload size of 10Gbe is 9000 bytes.

The signal has to be packetized before transmission. The packetizer inputs are the integrated real and imaginary components that are output from the accumulators. The four first in first out (FIFO) buffers present in the packetizer module are used to capture the accumulated spectra synchronously from the VACC blocks. The size of each spectrum is ≈ 8 kB (which is also the size of each FIFO); four spectra amount to ≈ 32 kB. However, the maximum payload capacity of 10Gbe is only 9kB. Thus, the

[3]a FIFO buffer of variable size and read/write clocks

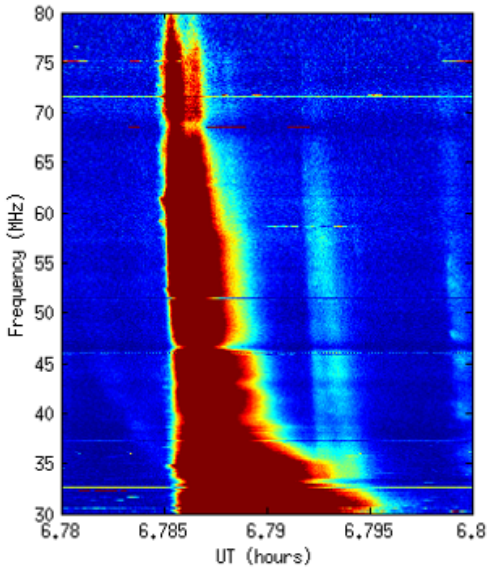

Figure 5.2: Sample observation of a Solar Type III burst with the ROACH Based backend.

four spectra must be transmitted sequentially for smooth operation of the 10Gbe core, without overflow of the transmit FIFO buffers.

After the last spectral sample is written to the FIFO, the `FIFOFULL` signal is asserted. On the assertion of this signal, the reading of spectrum data from the FIFO commences. After reading out the first FIFO completely, a delay is provided before the second FIFO is read out. This is to ensure that the 10Gbe core does not malfunction between data transmission. The packetizer control state machine was implemented in Simulink using a Matlab M-code block. On the DAS, a shell script is written to configure, control and acquire data during observation. Each set of four spectra are output as four 10Gbe packets for a single integration time. The delay between subsequent packets are ≈ 5 μs.

Observations of a Type III burst with the backend described above is shown in the Figure 5.2. We see that the burst does not exhibit any fine structures, and there also is a second weak doublet-like component which is seen $\approx$ 18 seconds later.

5.3 Long Baseline Low Frequency SpectroPolarimeter (LFSP)

During the first cycle of observations with the low frequency spectropolarimeter, it was found that some bursts extended to frequencies below the cut-off frequency of GRIP (see Figure 5.2). Previous observations from Gauribidanur showed that the ionospheric cut-off there could reach as low as 15 MHz. So we decided to increase the operating frequency of the array to study the nature of polarization of radiation arriving from the Sun at frequencies close to ionospheric cut-off.

5.3.1 Instrument

An important parameter in choosing the necessary antenna architecture is the required bandwidth of operation. Our goal was to study the characteristics of solar transients in metric and decametric wavelengths. The low frequency cut-off will thus be the ionospheric cut-off frequency at Gauribidanur, which is ≈ 15 MHz. The high-frequency cut-off is decided by the frequency beyond which the terrestrial radio frequency interference starts dominating the RF band, which in the present case is the FM transmissions (88 MHz – 108 MHz). Thus we chose our upper frequency cut-off to be ≈ 85 MHz. The required bandwidth ratio is $\approx 6{:}1$. This requires a frequency independent antenna, whose electrical characteristics are to be identical throughout a wide range of frequencies.

We chose the log periodic dipole antenna (LPDA) as our primary element due to its relative ease of construction and uniform gain characteristics throughout the band of interest. Standard techniques described by Raja et al. [2013], Kishore et al. [2014], and references therein were followed for the preliminary design of the LPDA. This initial design was repeatedly tuned to match the impedance throughout the band of operation. We used an inductive stub to counter the capacitive reactance at low frequencies. The voltage standing wave ratio (VSWR) of the antenna at various stages of design is shown in Figure 5.3. Note that between frequencies 15 MHz – 85 MHz, the VSWR is less than two, which implies ≈ 90 % power transfer from source to load. The parameters of the designed LPDA is listed in

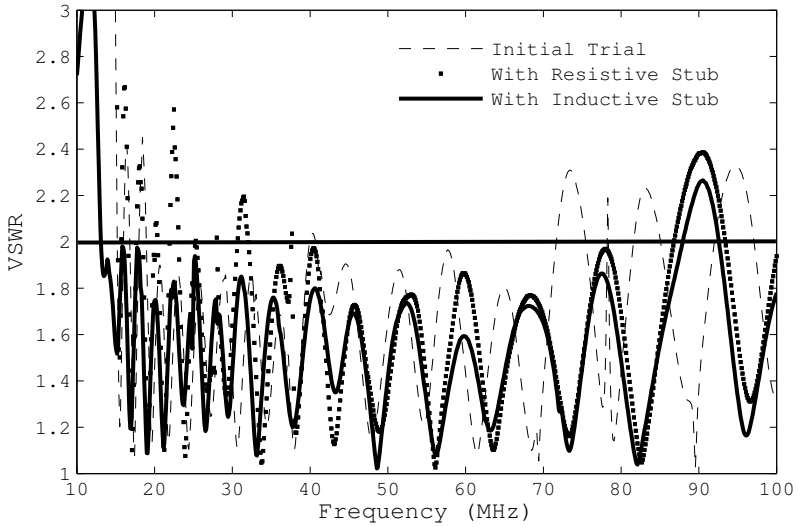

Figure 5.3: VSWR of antennas during an initial trial, with resistive stub and inductive stub. Note the improvement of VSWR in the operational band after the inclusion of the inductive stub.

Table 5.2

The received signal from each antenna passes through an analog front end (AFE) system. The AFE is composed of a five stage high pass (HPF) and low pass Filter (LPF) and an amplifier. The HPF is used to cut off strong low-frequency short-wave transmissions <15 MHz. The LPF is used to cut off the FM band. The filtered signals are amplified by ≈ 30 dB. The characteristics of the filters and amplifier are shown in Figure 5.4.

The signal is then transmitted via phase-matched RG58U coaxial cables of length ≈ 50m to the group center, where it is power combined with signals from other antennas of the group. The cables are phase matched to an accuracy of ±2.5°. The spacing between individual antennas in a group is ≈ 10 m. There are three such groups (see Table 5.3), of which two are oriented parallel to east-west (EW; "90 °" group) and the third is parallel to the NS (NS; "0 °" group). The groups are laid out as an one dimensional EW interferometer. A Schematic of a single group with the AFE is shown in Figure 5.5. An image of a 90°group is shown in Figure 5.6.

Table 5.2: Antenna Parameters

Parameters	Values
Number of Arms	19
Apex Angle	37
Design Constant(τ)	0.87
Spacing Factor (σ)	0.032
Gain	5.5 dBi
E-Plane HPBW	60
H-Plane HPBW	110
Collecting Area	$0.5\lambda^2$
VSWR in operating Band	< 2

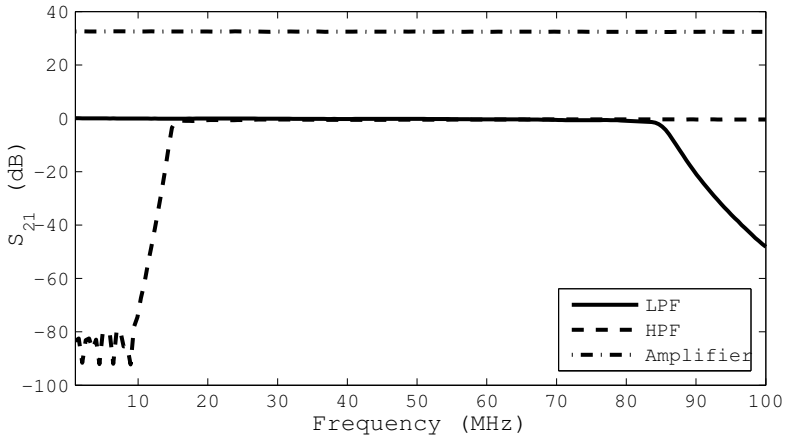

Figure 5.4: The Transfer characteristics of the LPF, HPF and Amplifier.

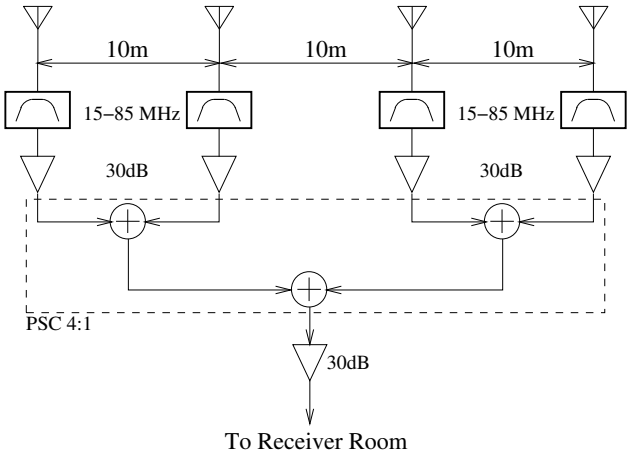

Figure 5.5: Schematic of the AFE of a single group. The other groups also have a similar AFE setup.

Table 5.3: Group Parameters

S. No.	Number of Antennas	Orientation	Group Extent (m)	Group HPBW
1	4	0	30	1.91λ
2	4	90°	30	1.91λ
3	8	90°	70	0.82λ

The power combined group signal is amplified by ≈ 30 dB and transmitted to the central receiving station via RG8U cables of varying lengths. These signals are amplified and filtered in the receiving station once more before digitization to: i) compensate for cable loss, and ii) attenuate out of band signals before being input to the digital backend. The digital backend used for this system had a similar architecture to the original GRIP version, but had a 2× improved spectral resolution.

The mutual coherence between group 1 and 3 is a measure of Stokes V and that between group 2 and 3 is a measure of Stokes I. The effective baseline lengths are ≈ 1.2 km. This is to remove all contribution from the extended corona and observe only transient energy releases.

Figure 5.6: Image of a single group. The antennas are nearly 6m tall and 5m wide. The smaller antennas on the far side are a part of GRIP array.

Table 5.4: Instrument Parameters

Parameter	Value
Primary Element	Log Periodic Dipole Antenna (LPDA)
Operation Frequency	15 - 85 MHz
Number of Groups	3
Collecting Area	$16\lambda^2$ (Stokes I and Stokes V)
Field of View	$\approx 0.82\lambda$ x 90 (RA x Dec)
Spectral Resolution	48.8 kHz
Time Resolution	typ. 0.1 s (programmable)
Dynamic Range	$\approx$ 48 dB

5.3.2 Calibration

Calibration of polarimeters is usually carried out by feeding a switched noise input at the antenna feed, feeding noise from another antenna which is located higher than the array to be calibrated or using drones [Pupillo et al. 2015]. However, due to the extent of the array (≈ 1.2 km) implementing the aforementioned techniques for polarization calibration was not possible in our case. A strong unpolarized calibrator source like Cygnus-A can be used to set the flux Scale for Stokes I and also to estimate the instrumental polarization [Sault et al. 1996]. Also, due to the high radio brightness of Cygnus-A (>15000 Jy in 15-85 MHz), it can be used to unambiguously calibrate high time resolution (≈ 0.1 s) observations.

The deflection obtained for Cygnus-A in Stokes V can be used to remove instrumental polarization that arises due to mutual coupling between antennas, spurious ground reflections, polarization induced by signal path, etc.

The Stokes - I and Stokes - V solutions obtained for the calibrator can be directly applied to solar observations for estimating the flux and the error in degree of circular polarization (dcp) of solar transients. Note that due to the baseline lengths involved, the extended emission from the background is completely resolved and mutual coupling between Stokes - I and Stokes - V interferometers are minimized. We also use this instrument to carry out only transit observations, thus avoiding source-position dependent errors.

5.3.3 Noise Storm Observations

The noise-storm observation presented here were carried out during 18 – 19 June 2016. This storm was found to be associated with active region AR12567. The mutual coherence between two groups of antennas oriented in the same direction yield Stokes - I, while that of 2 groups oriented orthogonally is used to estimate Stokes - V. LFSP operates in the frequency range of 15 – 85 MHz. The time resolution of the data is ≈ 0.1 second and the spectral resolution is ≈ 48 kHz. The Stokes - I and Stokes - V dynamic spectra observed on 19 July 2016, using LFSP is shown in Figure 5.7.

We also use imaging data from *Gauribidanur RAdio HeliograPH* (GRAPH: Ramesh98, Ramesh06, Ramesh11) for obtaining two-dimensional radio im-

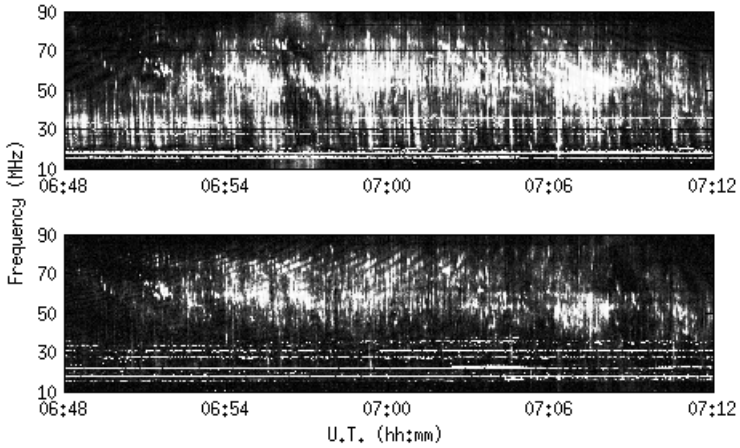

Figure 5.7: Dynamic Spectrum of Stokes - I (top) and Stokes - V (bottom) of the noise storm obtained using the LFSP. The spot-like features are Type I bursts, the vertical stripe-like features are Type III bursts. The horizontal lines are due to narrow-band RFI.

ages of the corona. GRAPH images the Sun at two interference free spot-frequencies (53.3 MHz and 80 MHz) with a time resolution of one second. The angular resolution of the final maps are $5' \times 7'$ and $7' \times 9'$ at 80 MHz and 53.3 MHz, respectively. A 2-D image of the active region at 80 MHz and 53.3 MHz obtained using GRAPH is shown in Figure 5.9. The GRAPH images are used to infer the heights of the source regions above the corona, and estimate the density model.

We used *Gauribidanur Low Frequency Solar Spectrograph* (GLOSS: Ebenezer et al. [2001], Kishore et al. [2014]) dynamic spectrum to find the largest frequency at which Type I and Type III bursts are observed during the days of observation. GLOSS is a phased array of eight antennas oriented in the NS direction. The response of GLOSS has to be electrically *tilted* in the declination axis to point it towards the Sun. The broad response of GLOSS in RA enables observation of the Sun for upto eight hours per day. GLOSS operates in a frequency band of 40 – 440 MHz with a spectral resolution of 1 MHz and a temporal resolution of 250 ms.

The data used for this observation was obtained for ≈ 30 minutes about the local meridian transit of the Sun using the LFSP. This was done to: i) avoid confusion arising due to array's side-lobes and grating-lobes at

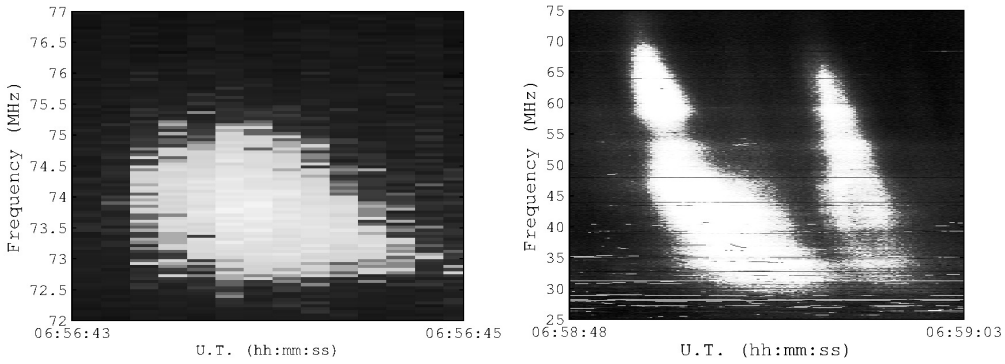

Figure 5.8: A sample isolated Type I (left) and Type III burst.

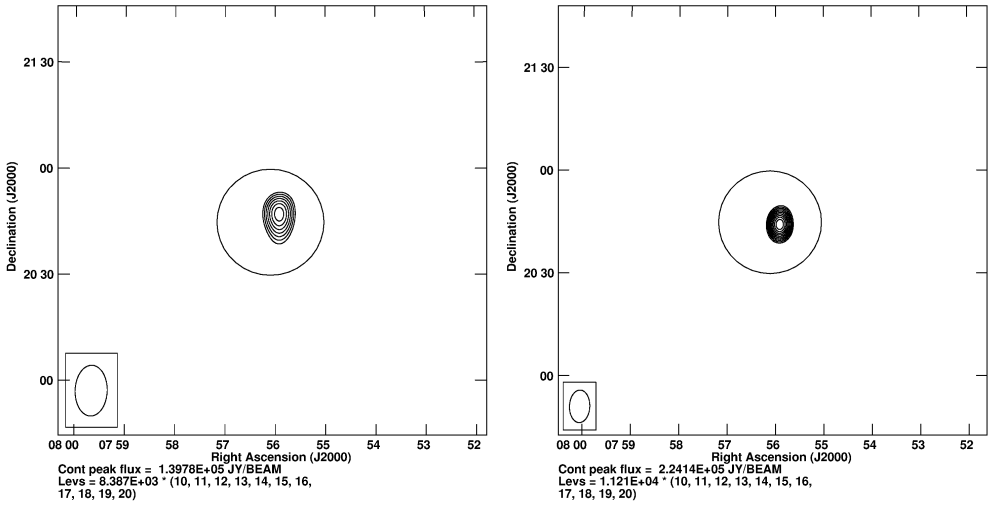

Figure 5.9: GRAPH images at 53.5 MHz (left) and 80 MHz. The circle is the solar photospheric disc. The *contours* indicate the presence of a noise-storm source close to the disk center. Also note that the flux at 80 MHz is greater than that at 53.3 MHz

higher frequencies, and ii) minimize errors in polarization due to parallactic angle. Cygnus A observations performed on the same day was used for flux calibration and to remove errors arising due to instrumental polarization.

The GRAPH images were made at both the frequencies by integrating the visibilities for ±10 seconds about the meridian transit. The GRAPH images also were calibrated using Cygnus A. An inspection of the GRAPH images at both the frequencies reveal the presence of a compact source on the disk, which is the storm source region.

From the spectropolarimeter observations, we chose only isolated Type I bursts for further analysis (see left panel, Figure 5.8). Those bursts that are a part of a chain, drifting chain, or those that appear to be indistinguishable from the background have not been considered for analysis. Similarly, Type III bursts which show peculiar drifts or those with some other features superimposed on them have not been considered.

5.3.3.1 Analysis and Results

From the Stokes-*I* spectrum (top panel, Figure 5.7), we observe that at lower frequencies, the bright background and spot-like features (Type I bursts) are not visible. Storm observations in the past indicate the existence of a transition frequency around which the Type I bursts transcend to Type III bursts. Type III bursts are broad-band short-lived emission excited by an electron beam traversing across the plasma layers at relativistic velocities. Keeping this in view, we carried out a statistical analysis of the data. We use fractional bandwidth as a figure of merit for studying the spectral characteristics of both Type I and Type III bursts. Fractional bandwidth is defined as the ratio of the bandwidth of the burst to that of the center frequency.

A MATLAB program was used to semi-automatically detect individual bursts. The detected bursts were integrated in time to obtain the frequency profile. A Gaussian of the form $a \exp\left(-((f - f_c)/\delta f)^2\right)$, where f_c is the center frequency, δf is the bandwidth of the burst and a is the peak amplitude, was fitted to the obtained frequency profiles in the case of Type I bursts. For Type III bursts, the frequencies of first and last appearance were used for estimating the fractional bandwidth. For both of the days,

we obtained > 100 individual Type I and Type III bursts. We found that the lower cut-off of Type I bursts occurred around ≈ 50 MHz. The bursts were observed up to the high frequency cut-off of the instrument. The bursts were well dispersed in both time and frequency planes. Type III bursts had a fractional bandwidth in the range of 0.4 to 1.2. A scatter plot of fractional bandwidth and center frequency of Type I and Type III bursts is shown in Figure 5.11. The transition frequency occurs at ≈ 53 MHz.

Based on this result, we carried out further analysis of the bursts and the continuum background to study the characteristics of these bursts in detail and also identify any change in the radio emission characteristics above and below the transition frequency.

For continuum analysis, we used the temporal intensity variation profile at the frequencies of interest. The lower envelope of the profile was used as the continuum background (see Figure 5.10). This is justified if the storm continuum is considered to be a broad-band long lived background over which bursts are superposed. The presence of only a single source in the radio image indicates that continuum emission at both high and low frequencies arise from the same region. On detailed analysis of the continuum profiles obtained at different frequencies, we found that the spectral indices of metric continuum (> 50 MHz) were different from those of the decametric continuum (< 50 MHz). By fitting a power law to the flux as a function of frequency, we found that the spectral indices for the metric and decametric continuum were +2.9 and -1.6 respectively (see Figures 5.12 and 5.13). This sets an upper limit on the extent of the Type I continuum source region.

Since the bursts were dispersed in time and frequency, we used amplitude and frequency of all the observed bursts as they belong to the same burst complex to study the spectral index of Type I bursts. By fitting a power law to the above distribution, we found that the spectral index of Type I bursts was ≈ +3.4 (see Figure 5.14). Note that the trend in frequency shown by the flux of Type I bursts as well as the metric continuum are similar.

We used the Type III bursts observed during the two days to study the spectral characteristics of the bursts. Flux for different bursts at frequencies within the upper and lower cut-off was estimated from their individual

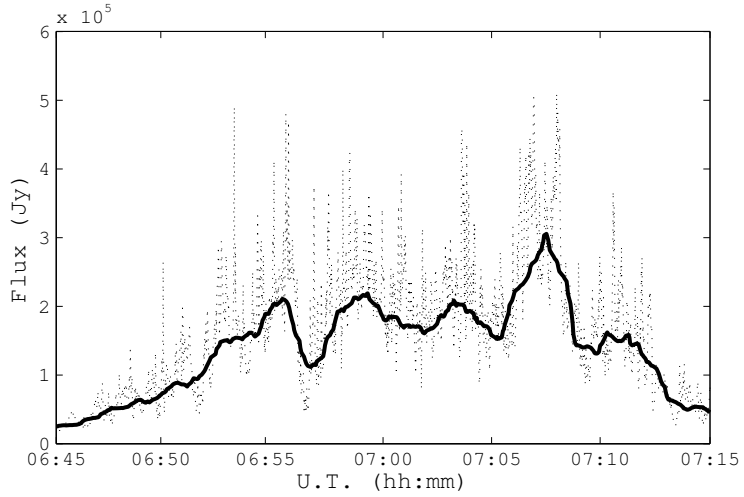

Figure 5.10: The *solid* line is the continuum background at 55 MHz. The *dots* are the fluctuation in the received power during the storm.

time profiles. A power-law curve was fit for the flux as a function of frequency for all the bursts. For all the Type III bursts, the flux decreased with frequency. The mean spectral index was -2.7±0.2 (see Figure 5.15). Note that similar to Type I burst and continuum, Type III burst and continuum also show the same spectral variation.

From the inspection of the Stokes - V dynamic spectrum (see bottom panel, Figure 5.7),we see that at low frequencies, there is a decrease in the circularly polarized intensity. So, we carried out an analysis of the degree of circular polarization (dcp) for both Type I and Type III bursts respectively. We define dcp as the absolute value of the ratio of Stokes - I and Stokes - V fluxes. For Type I bursts, we estimated the dcp as the ratios of the peak of the Gaussian fit for both Stokes I and Stokes V. For Type III bursts, the peak values at the center frequency of the burst was used for DCP calculation. From the distribution of DCP (see Figure 5.16) we see that Type I bursts are more polarized than Type III bursts. The minimum % DCP for Type I bursts is $\approx$ 55%, while most Type I bursts are strongly polarized (DCP > 90%). On the other hand, Type III bursts were only moderately polarized. Out of the observed bursts, only $\approx$ 50% showed any detectable Stokes - V deflection. The distribution of DCP for these bursts are shown in Figure 5.17.

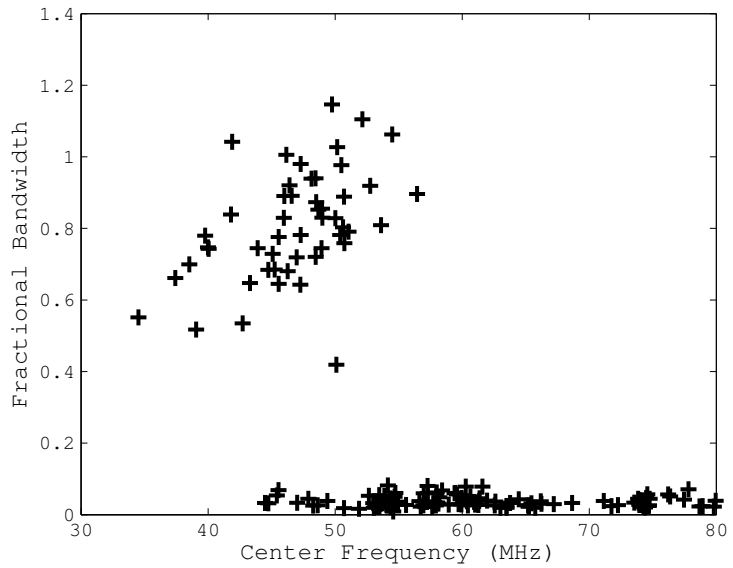

Figure 5.11: Scatter of fractional bandwidth and center frequency of bursts. Note the disappearance of Type I bursts at frequencies <50 MHz.

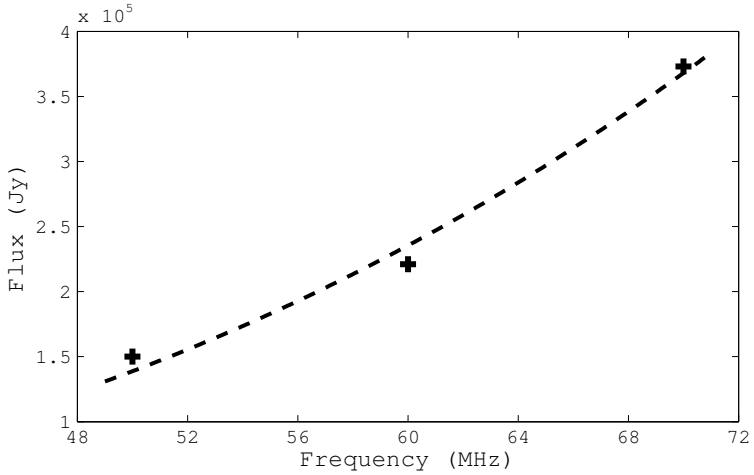

Figure 5.12: Spectral index of the metric continuum. The *dashed line* is a power-law fit of index +2.9

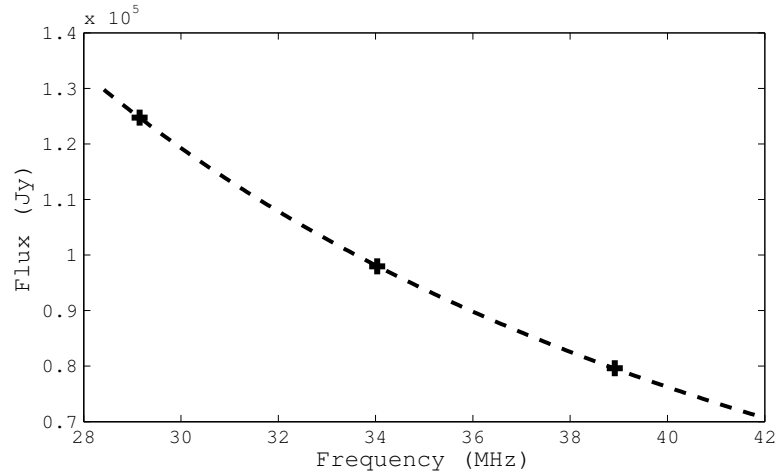

Figure 5.13: Spectral index of the decametric continuum. The *dashed line* is a power-law fit of index -1.6

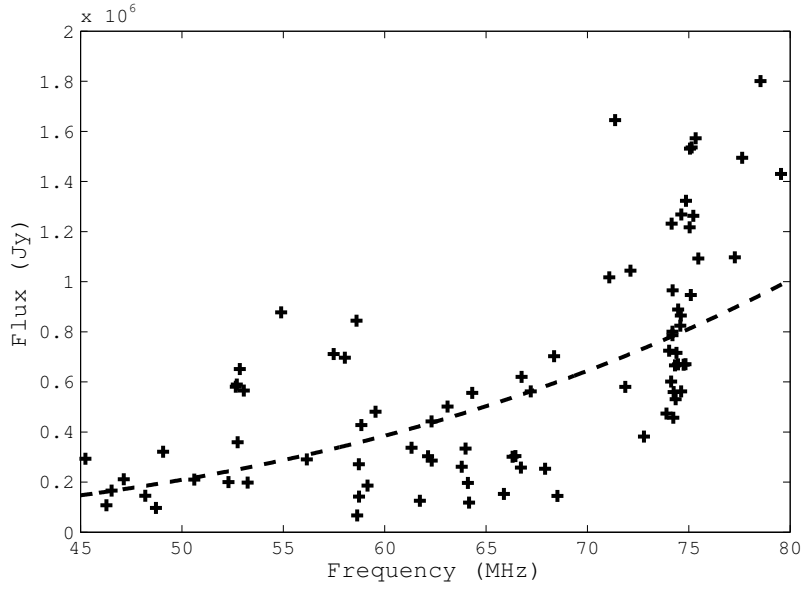

Figure 5.14: Spectral index of Type I bursts. The dashed line is a power-law fit of index +3.4

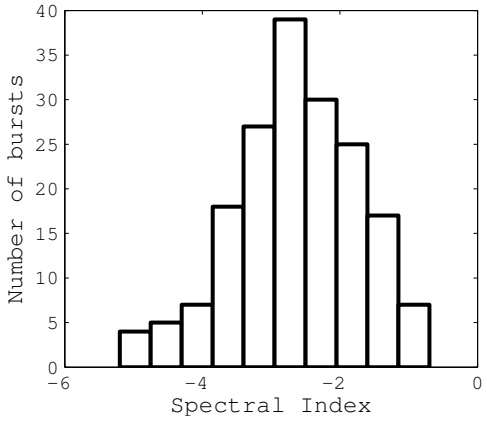

Figure 5.15: Spectral index distribution of Type III bursts

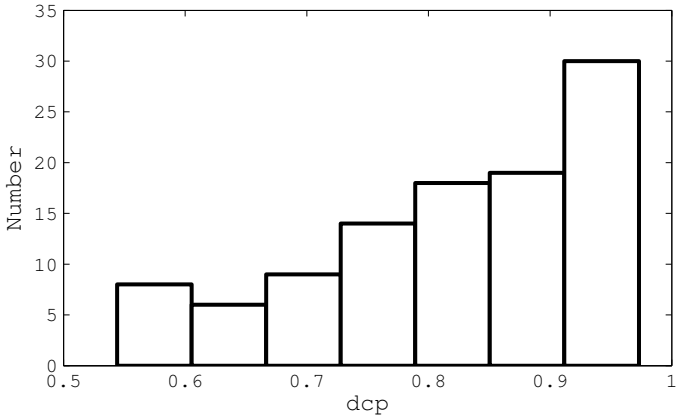

Figure 5.16: Bar plot showing dcp distribution of Type I bursts

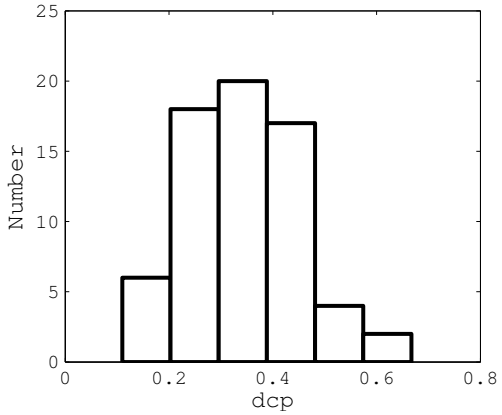

Figure 5.17: Bar plot showing dcp distribution of Type III bursts

5.3.3.2 Discussions

Using the result of the analysis presented in the previous section, we attempt to put forward a possible scenario for the observed characteristics (see Figure 5.18). Noise storm emission is generally thought to emanate from electron acceleration in closed magnetic arches. The exact mechanism of electron acceleration is not known. Since the corona is a plasma medium, the laws governing propagation through a plasma dictate that electromagnetic radiation occurring at a frequency [f] must originate at or near regions of plasma frequency [f]. Inspection of GLOSS data for the duration of the noise storm revealed that beyond 220 MHz, there was no Type I activity. From the low frequency spectro-polarimeter observations, we also see that there was no Type I emission at frequencies < 50 MHz.

Thus using an appropriate density model, the extent of the Type I source region can be constrained. We used the heliograph images for this. Using the above, we estimate the rotation rate [β], of the sources at both the frequencies. From this, the radial distance [r], can be estimated using the relation: $r\phi = D\beta$, where $\phi \approx 13.3°$is the angular displacement of the associated Active region on the solar disk per day and D is the sun–earth distance which is $\approx 215\,R_\odot$ [Ramesh et al. 2011]. The estimated radial distances and frequencies were then used to numerically solve to find an appropriate density model. Baumbach–Allen density model with an enhancement factor of two provided the closest match, with minimized

least square error, to the radial distances obtained from the previous step. Based on this, we find that the Type I source region extends from 1.03 $R_\odot$ to 1.51 $R_\odot$.

Based on the results obtained from our spectral index analysis of Type I continuum and bursts described in Section 5.3.3.1, we find that both have a positive spectral index. The positive spectral index obtained for both the continuum and bursts are consistent with previous results reported by Sundaram and Subramanian [2004] in the 50 – 80 MHz range and Iwai et al. [2012] at frequencies greater than 100 MHz, respectively. This gives us confidence in the approach we used for analysis. Thus, we suggest that both Type I bursts and continuum have the same emission mechanism. Numerous, indistinguishable Type I bursts of different energy levels form the continuum emission. Those bursts, which are brighter than the continuum (albeit still a part of the continuum) are observed as the Type I bursts. Plasma emission from suprathermal electrons [Thejappa 1991] are the cause of Type I bursts. The finite bandwidth and time of these bursts can be explained as fluctuations in the suprathermal electron density.

We find from GLOSS observations on 18 – 19 July 2016 that Type III bursts coinciding with our time of observation were restricted at frequencies < 100 MHz. The start frequencies of these bursts are around 50 – 60 MHz. This shows that Type III bursts observed during storms also originate from the Type I source region. Also it indicates that the open magnetic field lines along which Type III electrons travel originate at the height range corresponding to the above frequency range.

The fact that no Type III burst was observed to originate from frequencies >220 MHz during the observation time of LFSP indicates that all of the Type III bursts observed are indeed associated with the noise-storm radio emission region [Gergely and Erickson 1975, Gergely and Kundu 1975]. The Type III start frequencies are close to the cut-off frequency of the Type I storm emission, which suggests that these Type III electrons are beamed from regions close to the edge of the Type I source. Thus, the claim that Type III bursts observed during noise storms arise from the same electron population of Type I bursts may seem plausible, if we constrain Type III bursts to originate from escaping electrons that are close to the cusp of the magnetic arch. Type III electrons may be left over electrons that were

responsible for Type I bursts, which escape the magnetic arches at a lower velocity into the open field lines, thus exciting the plasma layers there, and are manifested as Type III bursts.

The spectral index values obtained for the Type III continuum and bursts are -1.6 and -2.7 respectively. This suggests that the continuum may just be an agglomeration of Type III bursts occurring in rapid succession. Since the Type III continuum is observed only < 50 MHz, this is an indication that the emission regions of Type I and Type III continuum do not overlap.

We also find that Type I bursts are more polarized than Type III bursts. Magneto-ionic theory describes two modes of wave propagation: ordinary mode (o-mode) and extra-ordinary mode (e-mode). The cut-off frequency of o-mode is at ω_p, while that of the e-mode is at $\frac{1}{2}(-\omega_e + \sqrt{\omega_e^2 + 4\omega_p^2})$, where ω_p is the electron plasma frequency and ω_e is the electron gyro-frequency. The above equations show that the e-mode cut-off occurs higher in the corona than the o-mode cut-off. All of the radiation emitted by the source at frequency $< \omega_p$ will not escape and thus no radiation will be observed. Radiation from the source emitted at frequencies between the o-mode and the e-mode cut-off frequencies will escape with polarization at o-mode and will have a strong circularly polarized signature. Radiation emitted at frequencies greater than o-mode and e-mode cut-off will escape with both modes, but the net polarization will be lower. The above theory can be applied to Type I bursts. If Type I bursts emanate from plasma layers having cut-off frequency between that of o-mode and e-mode frequencies, then one would expect to measure high degrees of circular polarization, similar to the one measured here. This suggests that Type I bursts may be a result of fundamental plasma emission.

As far as the polarization of Type III bursts are concerned, we detect low polarization values ($\approx 25\,\%$), which is consistent with that reported for fundamental Type III emission [Dulk and Suzuki 1980, Sasikumar Raja and Ramesh 2013]. The low values of polarization can be due to mixing of magneto–ionic modes, which would result in a net decrease of DCP.

We note here that due to the wide instantaneous bandwidth, we were able to obtain simultaneous observations of Type I and Type III storm radio emission. With the superior spectral and temporal resolutions, we

are able to distinguish between the continuum and burst components of each emission type. We also find that the nature of the polarization of Type I and Type III bursts are entirely different, a deduction which was possible because of the spectro-polarimetric capabilities of the instrument. This has enabled us to constrain the properties of both Type I and Type III bursts and their continuum.

5.4 Wideband Low Frequency Spectropolarimeter Backend for the Gauribidanur RAdio SpectroPolarimeter (GRASP)

Gauribidanur RAdio SpectroPolarimeter (GRASP) is a spectro-polarimeter instrument which extends the high frequency capability of polarimeter instruments at Gauribidanur. The array, during its initial installation was designed to observe solar radio emission in the frequency range of 35-85 MHz. But during this time, bursts extending beyond the band-pass of the instrument were noticed, and it was decided to build a prototype Crossed-Log Periodic Dipole Antenna, which extended the high frequency cut-off to 400 MHz [Kumari 2015]. This antenna replaced the original LPDAs of the GRASP instrument.

5.4.1 GRASP with CLPDA

The outputs from the orthogonal arms of the CLPDA are connected to an amplifier, and is converted to intensity modulated optical signal using an RF over Fiber (RFoF) module, after rejecting the FM band. The optical signal is demodulated at the receiver and is amplified once more to compensate for the conversion loss in the RFoF link. The final spectra is recorded in a commercially available spectrum analyzer, at a spectral and temporal resolution of 1 s, and 1 MHz, respectively.

But observations with the LFSP (see previous section) and FFTS (see Chapter 4) have revealed bursts with lifetime and bandwidths less than the spectral and temporal resolutions of the existing GRASP. So, using similar wide-band digital receiver techniques it was sought to increase the

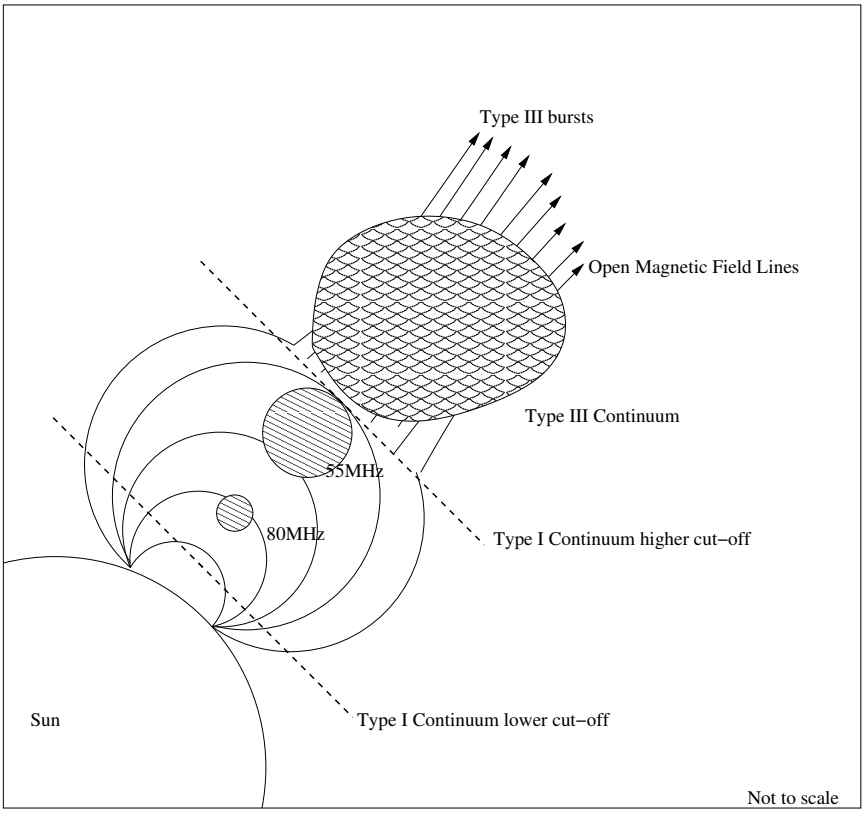

Figure 5.18: A scenario suggested for unified Type I and Type III storm emission. The hatched region is from where the Type I radiation originates. The radiation extends all the way along the open field lines. The Type I radiation originates from the region constrained between the two lines representing the upper and lower storm radiation cut-offs as obtained from GLOSS and the spectro-polarimeter respectively. The hatched circles are the positions of storm source region as observed from GRAPH.

instantaneous bandwidth of the instrument to 400 MHz.

5.4.2 400 MHz Spectropolarimeter Backend

Since the requirement for the instantaneous bandwidth was ≈ 400 MHz, to sample the RF band directly, an ADC that could sample at atleast 800 MHz is required. For this purpose, a Casper iADC capable of sampling speeds upto 1 GHz was used. The ADC connects to a ROACH-1 board through a ZDOK connector.

The ADC signal undergoes a similar path on the FPGA, as outlined in the previous section, with the following differences:

1. The data from the ADC is transferred to the FPGA at the rate of 800 MSPS as 4 parallel lanes at 200 MSPS each. These samples are Fourier transformed using the Wide-band FFT block. The Wide-band FFT block is similar to the biplex-FFT block that was used for the previous backends, but calculates the FFT for the odd and even samples separately, and outputs the odd and even spectra. These spectra are requantized and accumulated separately to avoid increasing the data rate of the intermediate steps. Post-accumulation, the odd and even values of the Stokes I and Stokes V spectra are combined as a 64 bit number and is stored in a FIFO for transmission through 10 GBe. A packetizer was designed to sequentially transmit these from the FPGA to a DAQ PC.

2. In this system, there is only a single antenna, for each polarization. Thus, the auto-correlation spectra of the orthogonal arms are added to obtain the Stokes I spectra, and are correlated to obtain the Stokes V spectra.

The captured data is then analyzed using standard analysis routines written in MATLAB. The block diagram of the firmware is shown in Figure 5.19.

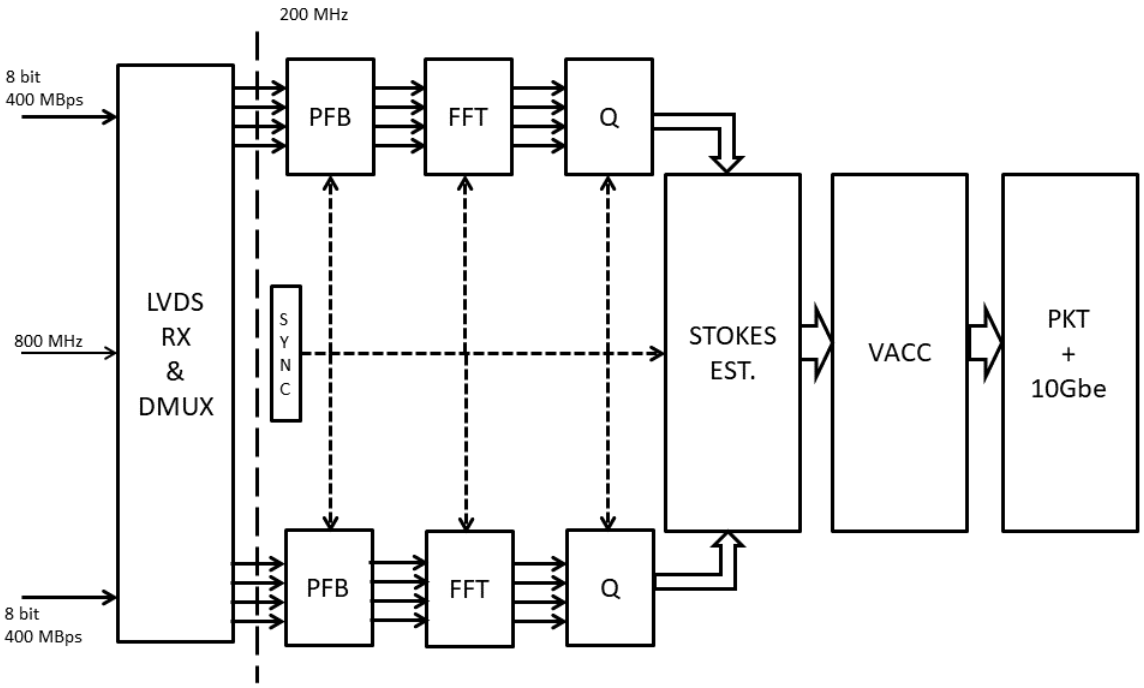

Figure 5.19: The firmware architecture of the 400 MHz spectropolarimetric backend.

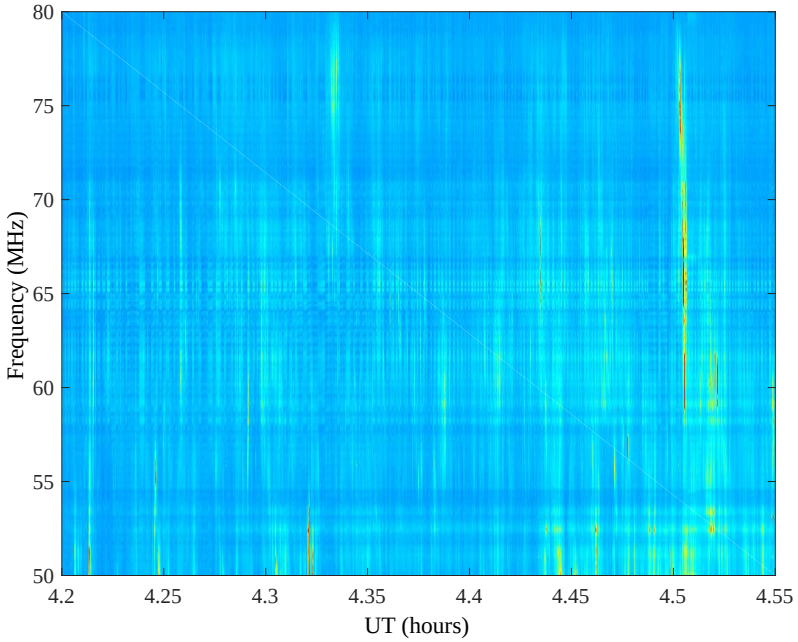

Figure 5.20: A dynamic spectra of a noise storm observed with the ROACH backend for the CLPDA antenna.

5.4.3 Noise Storm Observations: Comparison of Old and New Backends

Solar observations were carried out simultaneously with the old and new backends. By the time of observation using this instrument, the Sun had entered a minimum phase, and bursts become a rare occurrence. So, only a single noise storm was observed with this instrument.

The dynamic spectra of the figure is shown in Figure 5.20. We see shortlived broad-band stripes through out the dynamic spectrum, which indicate Type III storm activity. The same time span from the Spectrum Analyzer is shown in Figure 5.21. Both the data sets were integrated for the same time and frequency resolutions.

We see that the weak events seen in the ROACH system are not observed in the Spectrum Analyzer observations. For comparison between the two systems, we analyzed the noise fluctuations in the spectrum. The comparison between both the systems is shown in Figure 5.22.

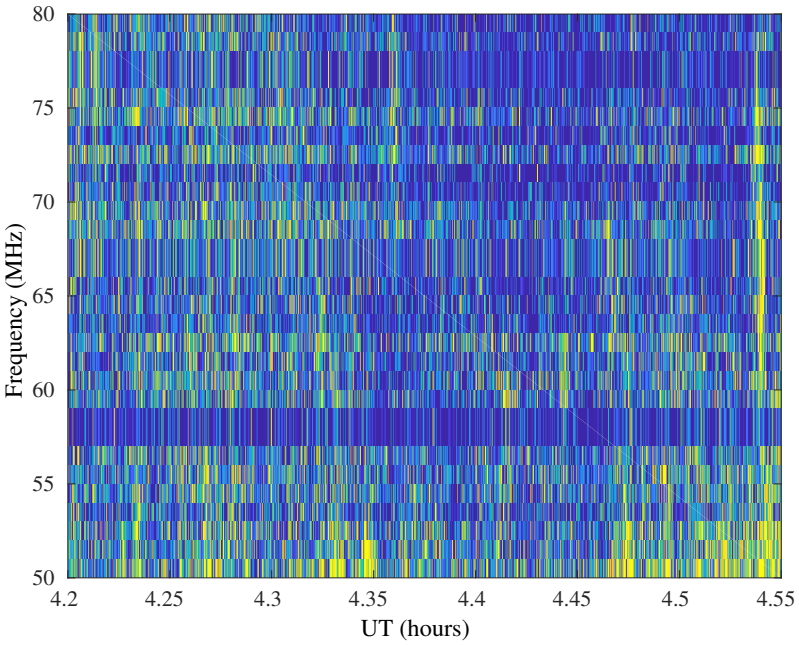

Figure 5.21: The same time span seen in Figure 1.9, but from Spectrum Analyzer observations.

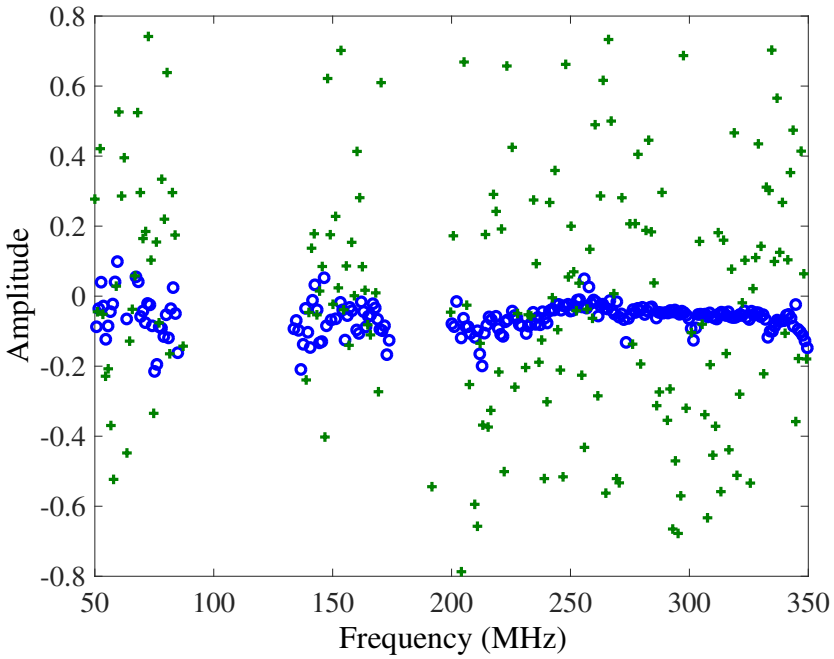

Figure 5.22: Comparison of the noise fluctuations in the ROACH and Spectrum Analyzer based systems.

We see that on an average, the noise fluctuations in the spectrum analyzer is atleast 8 times higher than that obtained from ROACH backend. This could be the reason why weak bursts are seen in the ROACH, but not on the Spectrum Analyzer backend, where they are buried in noise.

More observations using the above backend can reveal interesting properties of weak energy releases in the solar corona, and their polarization properties.

5.5 Summary

In this chapter, development of a end-to-end low frequency spectro-polarimetric system for low frequency solar radio observations was discussed. The instrument was used to observe solar noise storms at high temporal and spectral resolutions, which revealed fine structures in these bursts. Using these observation, we proposed a scenario for noise storms at low frequency, which is also in agreement with results by previous workers.

The preliminary results from a wide-band digital backend for GRASP was presented. The new backend was found to give a 8× better SNR compared to the existing commercial spectrum analyzer based backend. Future observations with this instrument is expected to reveal interesting features of weak radio bursts, which could be useful to study weak magnetic fields in the Corona.

References

Beckers, J. M. (1971). The Measurement of Solar Magnetic Fields. In Howard, R., editor, *Solar Magnetic Fields*, volume 43 of *IAU Symposium*, page 3.

Benkevitch, L. V., Rogers, A. E. E., Lonsdale, C. J., Cappallo, R. J., Oberoi, D., Erickson, P. J., and Baker, K. A. V. (2016). Van Vleck correction generalization for complex correlators with multilevel quantization.

Crochiere, R. and Rabiner, L. (1983). *Multirate Digital Signal Processing*, volume 1 of *Prentice-Hall Signal Processing Series: Advanced monographs*. Prentice-Hall, Upper Saddle River, 4 edition.

Dulk, G. A. and McLean, D. J. (1978). Coronal magnetic fields. *Solar Phys.*, 57:279–295.

Dulk, G. A. and Suzuki, S. (1980). The position and polarization of Type III solar bursts. *Astron. Astrophys.*, 88:203–217.

Ebenezer, E., Ramesh, R., Subramanian, K. R., Sundara Rajan, M. S., and Sastry, C. V. (2001). A new digital spectrograph for observations of radio burst emission from the Sun. *Astron. Astrophys.*, 367:1112–1116.

Gergely, T. E. and Erickson, W. C. (1975). Decameter storm radiation. I. *Solar Phys.*, 42:467–486.

Gergely, T. E. and Kundu, M. R. (1975). Decameter storm radiation. II. *Solar Phys.*, 41:163–188.

Hale, G. E. (1908). On the probable existence of a magnetic field in sun-spots. *The astrophysical journal*, 28:315.

Hale, G. E. and Nicholson, S. B. (1925). The law of sun-spot polarity. *The Astrophysical Journal*, 62:270.

Iwai, K., Tsuchiya, F., Morioka, A., and Misawa, H. (2012). IPRT/AMATERAS: A New Metric Spectrum Observation System for Solar Radio Bursts. *Solar Phys.*, 277:447–457.

Kishore, P., Kathiravan, C., Ramesh, R., Rajalingam, M., and Barve, I. V. (2014). Gauribidanur low-frequency solar spectrograph. *Solar Physics*, 289(10):3995–4005.

Kumari, A. (2015). *Development of cross-polarized log-periodic dipole antenna for low frequency radio spectral observations*. PhD thesis, Indian Institute of Astrophysics.

Lin, H., Kuhn, J., and Coulter, R. (2004). Coronal magnetic field measurements. *The Astrophysical Journal Letters*, 613(2):L177.

Nelson, G. J., Sheridan, K. V., and Suzuki, S. (1985). *Measurements of solar flux density and polarization*, pages 113–154.

Pätzold, M., Bird, M., Volland, H., Levy, G., Seidel, B., and Stelzried, C. (1987). The mean coronal magnetic field determined from helios faraday rotation measurements. *Solar Physics*, 109(1):91–105.

Price, D. C. (2016). Spectrometers and Polyphase Filterbanks in Radio Astronomy. *ArXiv e-prints*.

Pupillo, G., Naldi, G., Bianchi, G., Mattana, A., Monari, J., Perini, F., Poloni, M., Schiaffino, M., Bolli, P., Lingua, A., Aicardi, I., Bendea, H., Maschio, P., Piras, M., Virone, G., Paonessa, F., Farooqui, Z., Tibaldi, A., Addamo, G., Peverini, O. A., Tascone, R., and Wijnholds, S. J. (2015). Medicina array demonstrator: calibration and radiation pattern characterization using a UAV-mounted radio-frequency source. *Experimental Astronomy*, 39:405–421.

Raja, K. S., Kathiravan, C., Ramesh, R., Rajalingam, M., and Barve, I. V. (2013). Design and performance of a low-frequency cross-polarized log-periodic dipole antenna. *The Astrophysical Journal Supplement Series*, 207(1):2.

Ramesh, R., Kathiravan, C., and Narayanan, A. S. (2011). Low-frequency observations of polarized emission from long-lived non-thermal radio sources in the solar corona. *The Astrophysical Journal*, 734(1):39.

Ramesh, R., Kathiravan, C., SundaraRajan, M. S., Barve, I. V., and Sastry, C. V. (2008). A low-frequency (30 – 110 mhz) antenna system for observations of polarized radio emission from the solar corona. *Solar Physics*, 253(1):319–327.

Sasikumar Raja, K. and Ramesh, R. (2013). Low-frequency Observations of Transient Quasi-periodic Radio Emission from the Solar Atmosphere. *Astrophys. J.*, 775:38–43.

Sault, R. J., Hamaker, J. P., and Bregman, J. D. (1996). Understanding radio polarimetry. II. Instrumental calibration of an interferometer array. *Astron. Astrophys. Suppl.*, 117:149–159.

Schwabe, H. (1844). Sonnenbeobachtungen im Jahre 1843. Von Herrn Hofrath Schwabe in Dessau. *Astronomische Nachrichten*, 21:233.

Stenflo, J. (1982). The hanle effect and the diagnostics of turbulent magnetic fields in the solar atmosphere. *Solar Physics*, 80(2):209–226.

Sundaram, G. A. S. and Subramanian, K. R. (2004). Spectrum of Solar Type I Continuum Noise Storm in the 50-80 MHz Band and Plasma Characteristics in the Associated Source Region. *Astrophys. J.*, 605:948–959.

Thejappa, G. (1991). A self-consistent model for the storm radio emission from the sun. *Solar Phys.*, 132:173–193.

Thompson, A. R., Moran, J. M., and Swenson, G. W. (2001). *Interferometry and Synthesis in Radio Astronomy; 2nd ed.* Wiley-VCH, Weinheim.

Vaidyanathan, P. P. (1993). *Multirate Systems and Filter Banks*, volume 1. Prentice-Hall, Inc., Upper Saddle River.

Chapter 6

Conclusion

"The road goes ever on and on" — J.R.R. Tolkien, The Hobbit

Over the previous three chapters, instruments designed for various types of solar observations at low frequencies, their characterization and results obtained from performing observations with them have been presented.

In the Chapter 3, we built a Long baseline interferometer data recording system from scratch using low cost ADCs and FPGAs. Contrary to using costly atomic clocks, we established that LBI systems can work with standalone GPS disciplined units. It would be advantageous to study and compare the short and long term effects of using stand along GPSDOs with that of systems using atomic clocks. Also, this was studied only for two baselines, and the working of this over longer baselines is something that is still to be explored. This would be useful from the point of view of future LBI arrays targeting transients like Sky Watch Array Network (SWAN) [1] and Radio Array of Portable Interferometric Detectors (RAPID)[Lind et al. 2013]. Using this instrument, we were able to observe point sources on the Sun of sizes down to 15″, which have previously been observable only during eclipse observations. This implies that existing and future arrays can still have high resolution radio observation of radio emission from Sun as one of the primary science goals. These results also have set a new upper limit on the smallest size of angular broadening due to scattering in the

[1] http://www.rri.res.in/SWAN/SWANRRI.html

solar corona. It was also found that the bursts observed belonged to the category of weak energy releases from the solar corona, which was two orders of magnitude lesser than previously detected releases. These results were supported by further observations using the Murchison Widefield Array [Suresh et al. 2017]. Given the capabilities of present and future instruments like the Low Frequency ARray (LOFAR) [Van Haarlem et al. 2013] and Square Kilometer Array (SKA) [Dewdney et al. 2009] in terms of sensitivity and resolution, it is expected that the limits reported here will be refined.

In Chapter 4, we discussed the design and commissioning of a high resolution Fast Fourier Transform Spectrometer (FFTS) as a backend for the Gauribidanur Low Frequency Solar Spectrograph (GLOSS). Using this backend, we were able to resolve independent time and frequency structures of solar radio bursts, categorized as Type IIIb. We found that these bursts can be used as a new tool to probe turbulence in the 1.2 - 3 $R_{\odot}$, which has not been studied extensively in the past. Using the properties of the Striae, we derived electron density fluctuation versus the scale lengths, where we found that this followed a pattern similar to Kolmogorov turbulence. Follow up studies of this work has been published using similar bursts observed using LOFAR has also been published [Sharykin et al. 2018, Kolotkov et al. 2018]. These work has re-asserted our suggestion that this method can indeed be used as a technique to probe turbulence, whence low frequency radio radiation originates.

In Chapter 5, we elaborated the design and commissioning of a low frequency Radio Spectropolarimeter array and the various types of Digital backends used for them. Using knowledge gained from previous observations, we designed a system that can operate close to ionospheric cut-off frequencies, thus enabling us to probe the polarization of radio bursts to larger heliocentric distances. Noise storm observations using this array indicates a clear demarcation between type I and type III bursts, in terms of their bandwidth and polarization. Using this data, we presented a unified picture of storm emission, which is consistent with that presented by the previous workers [Stewart and Labrum 1972, Del Zanna, G. et al. 2011]. This instrument is still under operation, and a long term polarimetric study using the former would be useful to understand the variation of coronal

magnetic fields and the usage of radio bursts as their probes [Hariharan et al. 2014, 2016, Kishore et al. 2016, Kumari et al. 2017a,b].

6.1 Future work

The instrumentation development described in this thesis was carried out as feasibility study for expansion/upgrade the instruments at Gauribidanur Solar Radio Observatory (GSRO). On that front, it has been shown that using digital instruments for solar observations enables us to study bursts with high time and spectral resolution with also high dynamic range. Compared to the legacy instruments at GSRO, these instruments, due to their wide band of operation have managed provide data even during situations of high RFI. They also have a higher dynamic range, that enables us to study weaker radiation from the source. Thirdly, it has also led to new science results, which is the ultimate validation of the working of any instrument. The future work would now be to upgrade the legacy backends to the new digital ones. This would be as simple as a linear scaling operation, as the platforms on which the development was done was highly reconfigurable. This would result in enhanced spectral and temporal resolutions for solar imaging, and would lead to an unprecedented 3-D view of both quiet and active Sun.

From the science front, the results obtained from long baseline interferometric studies is promising to pursue it with a low frequency interferometric array and make arc-second scale resolution images of the solar corona at low frequencies. The GRAPH instrument is currently on the path to this. High spectral resolution imaging observations using scaled back-ends similar to the one used in Chapter 4 can provide a spatial as well as a radial distribution of coronal turbulence. The results in Chapter 5 also promise that an extension of the existing arrays to add polarimetric capabilities down to 15 MHz would be particularly advantageous to study coronal events affecting space weather.

These would be complemented by a new range of space based instruments like Parker Solar Probe [2], Solar Orbiter [3] and India's Aditya - L1

[2]https://www.nasa.gov/content/goddard/parker-solar-probe
[3]http://sci.esa.int/solar-orbiter/

mission [4], which have been equipped with an array of instruments to probe the sun in multiple wavelengths, in situ. Particularly, the Parker probe will reach distance as close to 7 $R_{\odot}$, where it will carry out the first in-situ observations of the coronal plasma close to the Sun.

The L5 Lagrangian point, which is a vertex of an equilateral triangle (show diagram) will be a suitable point to observe the Sun from (see Figure 6.1). This point provides a stable vantage, where the space craft can be parked to observe the sun continuously. Observations from this point will be advantageous from space weather point of view where earth directed CMEs can be studied readily, and an early warning system can be put in place. L5 point is at a distance of 1 au both from the Sun and the Earth. Radio payloads deployed from this point may not be affected from terrestrial RFI as much as a payload at L1 point.

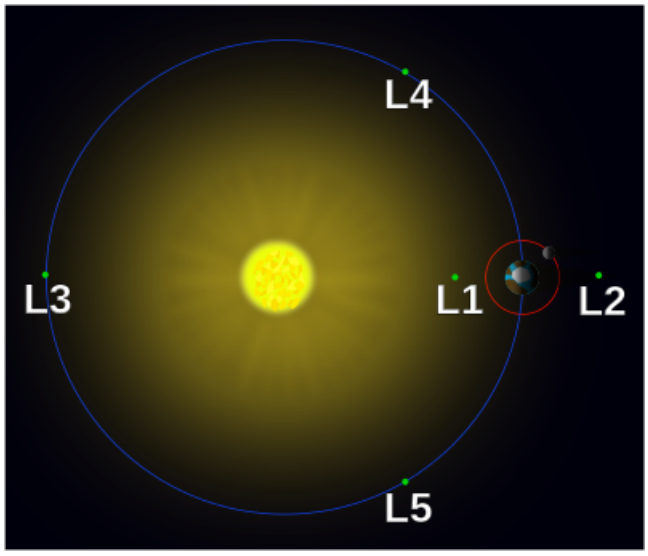

Figure 6.1: The Lagrange points. Note that L1 is where most of the present missions to study sun from space are located. L5 position is the vertex of an equilateral triangle, with 1 au long sides (Image Courtesy: `https://en.wikipedia.org/wiki/Lagrangian_point`).

With advent of cheap electronics and manufacturing technologies, CubeSats, which are a generation of small satellites have proved to be useful for

[4] http://aditya.iiap.res.in/about

dedicated science observations. SunRISE [Alibay et al. 2017], an interferometric cubesat experiment has been proposed to make low frequency interferometric observations of radio bursts.

All these techniques are complementary to each other, which is required to have a more complete picture of our closest star.

References

Alibay, F., Kasper, J. C., Lazio, T. J. W., and Neilsen, T. (2017). Sun radio interferometer space experiment (sunrise): Tracking particle acceleration and transport in the inner heliosphere. In *2017 IEEE Aerospace Conference*, pages 1–15.

Del Zanna, G., Aulanier, G., Klein, K.-L., and Török, T. (2011). A single picture for solar coronal outflows and radio noise storms. *Astron. Astrophys.*, 526:137.

Dewdney, P. E., Hall, P. J., Schilizzi, R. T., and Lazio, T. J. L. (2009). The square kilometre array. *Proceedings of the IEEE*, 97(8):1482–1496.

Hariharan, K., Ramesh, R., Kathiravan, C., and Wang, T. J. (2016). Simultaneous near-sun observations of a moving type iv radio burst and the associated white-light coronal mass ejection. *Solar Physics*, 291(5):1405–1416.

Hariharan, K., Ramesh, R., Kishore, P., Kathiravan, C., and Gopalswamy, N. (2014). An estimate of the coronal magnetic field near a solar coronal mass ejection from low-frequency radio observations. *The Astrophysical Journal*, 795(1):14.

Kishore, P., Ramesh, R., Hariharan, K., Kathiravan, C., and Gopalswamy, N. (2016). Constraining the Solar Coronal Magnetic Field Strength using Split-band Type II Radio Burst Observations. *Astrophys. J.*, 832:59.

Kolotkov, D. Y., Nakariakov, V. M., and Kontar, E. P. (2018). Origin of the Modulation of the Radio Emission from the Solar Corona by a Fast Magnetoacoustic Wave. *Astrophys. J.*, 861:33.

Kumari, A., Ramesh, R., Kathiravan, C., and Gopalswamy, N. (2017a). New Evidence for a Coronal Mass Ejection-driven High Frequency Type II Burst near the Sun. *Astrophys. J.*, 843:10.

Kumari, A., Ramesh, R., Kathiravan, C., and Wang, T. J. (2017b). Strength of the Solar Coronal Magnetic Field - A Comparison of Independent Estimates Using Contemporaneous Radio and White-Light Observations. *Solar Phys.*, 292:161.

Lind, F. D., Lonsdale, C. J., Faulkner, A. J., Alexander, P., and Mattmann, C. (2013). Radio array of portable interferometric detectors (rapid). In *2013 IEEE International Symposium on Phased Array Systems and Technology*, pages 676–683.

Sharykin, I. N., Kontar, E. P., and Kuznetsov, A. A. (2018). LOFAR Observations of Fine Spectral Structure Dynamics in Type IIIb Radio Bursts. *Solar Phys.*, 293:115.

Stewart, R. T. and Labrum, N. R. (1972). Meter-wavelength observations of the solar radio burst storm of August 17 22, 1968. *Solar Phys.*, 27:192–202.

Suresh, A., Sharma, R., Oberoi, D., Das, S. B., Pankratius, V., Timar, B., Lonsdale, C. J.,

Bowman, J. D., Briggs, F., Cappallo, R. J., Corey, B. E., Deshpande, A. A., Emrich, D., Goeke, R., Greenhill, L. J., Hazelton, B. J., Johnston-Hollitt, M., Kaplan, D. L., Kasper, J. C., Kratzenberg, E., Lynch, M. J., McWhirter, S. R., Mitchell, D. A., Morales, M. F., Morgan, E., Ord, S. M., Prabu, T., Rogers, A. E. E., Roshi, A., Udaya Shankar, N., Srivani, K. S., Subrahmanyan, R., Tingay, S. J., Waterson, M., Wayth, R. B., Webster, R. L., Whitney, A. R., Williams, A., and Williams, C. L. (2017). Wavelet-based Characterization of Small-scale Solar Emission Features at Low Radio Frequencies. *Astrophys. J.*, 843:19.

Van Haarlem, M., Wise, M., Gunst, A., Heald, G., McKean, J., Hessels, J., De Bruyn, A., Nijboer, R., Swinbank, J., Fallows, R., et al. (2013). Lofar: The low-frequency array. *Astronomy & astrophysics*, 556:A2.